Motion and interaction of a set of particles in a supercritical flow

Tobias Boehm

Motion and interaction of a set of particles in a supercritical flow

Mouvement et interaction d'un ensemble de particules dans un écoulement supercritique

Thèse présentée par **Tobias Böhm**

Pour obtenir le grade de Docteur de
l'Université Grenoble 1 - Joseph Fourier
Ecole Doctorale : Terre, Univers, Environnement
Spécialité : Mécanique des fluides

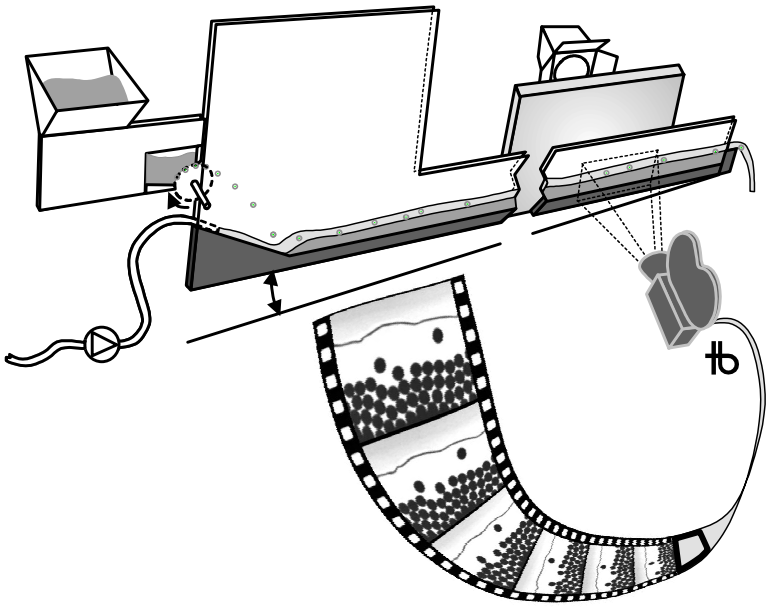

Soutenue le 18 février 2005 devant le jury composé de Messieurs :

Hans Herrmann	ICP Universität Stuttgart	président du jury
Daniel Lhuillier	LMM Paris	rapporteur du jury
François Métivier	IPG Paris	rapporteur du jury
Jean-Luc Reboud	LEMD Grenoble	directeur de thèse
Christophe Ancey	EPF Lausanne	codirecteur de thèse
Philippe Frey	Cemagref Grenoble	codirecteur de thèse

GRENOBLE 1 UNIVERSITE JOSEPH FOURIER SCIENCES.TECHNOLOGIE.SANTÉ

Cemagref
LA RECHERCHE POUR L'INGENIERIE DE L'AGRICULTURE ET DE L'ENVIRONNEMENT

Abstract[1] [Motion and interaction of a set of particles in a supercritical flow]: Bed load transport in watercourses is a longstanding problem in the mechanics of two-phase flows because the physical processes involved are poorly known or overly complicated. The motion of coarse, spherical glass beads entrained by a shallow turbulent water flow down a steep two-dimensional channel with a mobile bed was experimentally investigated. The study focused on bed load equilibrium flows, that is, neither erosion nor deposition of particles over sufficiently long time intervals occurred. Flows were filmed from the side using a high-speed camera. Image-processing software made it possible to determine the flow characteristics such as particle trajectories, their state of motion (rest, rolling, or saltating motion), and flow depth. The first striking result of our experiments was that, over short time periods, bed load transport appeared as a very intermittent process. The large solid-discharge fluctuations resulted essentially from arrangement in the mobile particle bed. Whereas for moderate slopes particles were mainly transported in saltation, the rolling regime was dominant for steep slopes.

Keywords: bed load transport, trajectories, rolling, saltation, mobile bed, supercritical flow, torrent, two-dimensional channel, image processing, solid discharge fluctuations.

PACS numbers (Physics and Astronomy Classification Scheme):
45.50.-j Dynamics and kinematics of a particle and a system of particles
45.70.Mg Granular flow: mixing, segregation and stratification
47.85.Dh Hydrodynamics, hydraulics, hydrostatics
92.40.Gc Erosion and sedimentation.

[1] See [BAF+05] for a summarizing paper of four pages.

Résumé en français[2] [Mouvement et interaction d'un ensemble de particules dans un écoulement supercritique]: Le transport solide par charriage dans les cours d'eau est un problème de longue date dans l'étude des écoulement biphasiques. Les processus physiques impliqués sont en effet mal compris et complexes. Nous présentons une étude expérimentale du mouvement de billes de verre sphériques grossières. Elles étaient entraînées dans un mouvement quasi-bidimensionnel par un écoulement d'eau turbulent peu profond dans un canal à forte pente sur un lit mobile. Nous avons étudié le cas de l'équilibre du transport solide, c.-à-d. qu'il n'y avait ni érosion ni dépôt de particules sur des intervalles de temps suffisamment longs. Les écoulements ont été filmés par le côté avec une caméra rapide. L'utilisation d'un logiciel de traitement d'images a permis de déterminer les caractéristiques des écoulements comme les trajectoires des particules, leur état de mouvement (arrêt, roulement ou saltation) et la hauteur d'eau. Le premier résultat frappant de nos expériences est que, sur des périodes de temps courtes, le transport par charriage apparaît comme un processus très intermittent. Les grandes fluctuations du débit solide résultent essentiellement de l'arrangement dans le lit mobile de particules. Alors que, pour des pentes modérées, les particules sont principalement transportées en saltation, le régime de roulement est prédominant pour des pentes fortes.

Mots clés : transport solide par charriage, trajectoires, roulement, saltation, lit mobile, écoulement supercritique, torrents, canal à deux dimensions, traitement d'images, fluctuations du débit solide.

[2]Voir Annexe D pour des résumés de chaque chapitre.

Zusammenfassung auf Deutsch [Bewegung und Wechselwirkung eines Partikelensembles in einer schießenden Strömung]: Der Geschiebetransport in Wasserläufen ist seit langem ein Forschungsfeld der Mechanik von Zweiphasenströmungen. Die beteiligten physikalischen Prozesse sind komplex und nur wenig verstanden. In einer experimentellen Studie wurde die Bewegung von grobkörnigen Glaskugeln näher untersucht. Diese wurden von einer turbulenten seichten Wasserströmung in einem Kanal mit hohem Gefälle und einem mobilen Bett in eine praktisch zweidimensionale Bewegung gesetzt. Dabei wurden die Bedingungen des Transportgleichgewichts eingehalten, d.h. es gab weder Erosion noch Ablagerung von Partikeln über hinreichend lange Zeiträume. Die Strömungen wurden von der Seite mit einer Hochgeschwindigkeitskamera gefilmt. Mit einem Bildverarbeitungsprogramm war es möglich, Strömungseigenschaften wie die Bewegungsbahnen der Partikel und ihren Bewegungszustand (Ruhe, Rollen oder Springen) sowie die Wasserhöhe zu bestimmen. Ein erstes, wichtiges Ergebnis unserer Experimente war, dass sich der Geschiebetransport als ein über kurze Zeitspannen stark pulsierender Prozess darstellte. Die großen Fluktuationen des Feststoffstroms waren vorwiegend durch die Anordnung des mobilen Partikelbetts bedingt. Während die Partikel bei gemäßigtem Gefälle hauptsächlich in Saltation transportiert wurden, dominierte bei hohem Gefälle die rollende Bewegung.

Schlüsselwörter: Feststofftransport als Geschiebe, Bewegungsbahnen, Rollen, Springen, mobiles Bett, schießende Strömung, Gebirgsbach, zweidimensionaler Kanal, Bildverarbeitung, Fluktuationen des Feststoffstroms.

Ode an die Freude

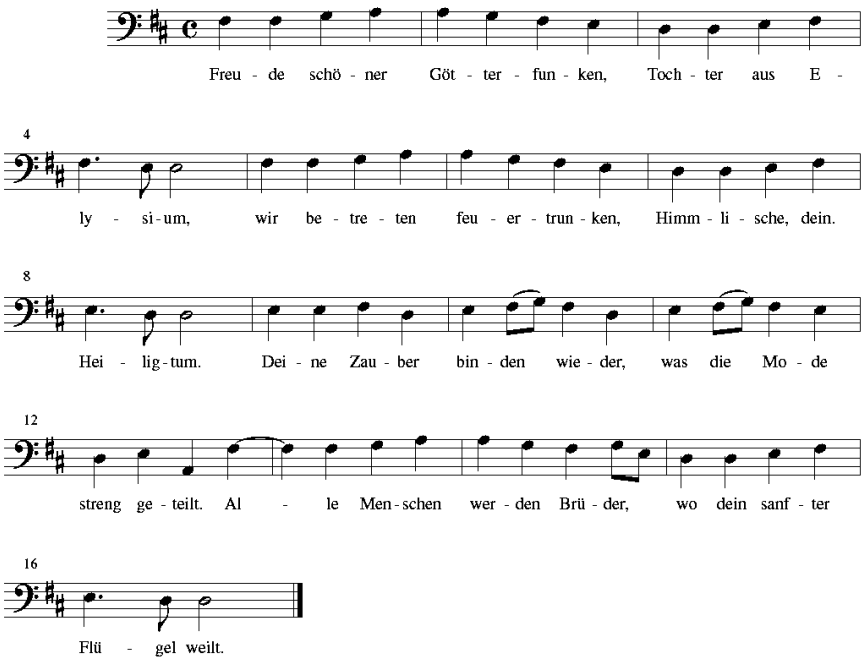

Aus: Ludwig van Beethoven, Sinfonie Nr. 9, Text: Friedrich Schiller.

Lustig quasselt

Lustig quasselt der seichte Bach.
Steinchen scheppern darüber flach.
Stumm gegen die Wellchen steht ein Stein,
Sieht – wie mir scheint –
Ernst aus und verweint.

Denn es macht traurig, unbequem zu sein.

— Joachim Ringelnatz

Remerciements

Je tiens d'abord à remercier les personnes qui m'ont fait l'honneur d'accepter de faire partie de mon jury de thèse. La discussion après la soutenance présidée par Hans Herrmann était enrichissante pour tous les participants. Je suis reconnaissant à Daniel Lhuillier et à François Métivier d'avoir pris en charge le travail de rapporteur. Daniel Lhuillier a montré son esprit de chercheur curieux lors de sa visite au Cemagref. J'ai eu le plaisir de rencontrer François Métivier lors d'une visite à son laboratoire de l'IPG à Paris et à un colloque à San Francisco.

Je voudrais exprimer toute ma gratitude aux trois personnes qui ont encadré ce travail de recherche. Malgré le changement de son propre domaine de recherche, mon directeur de thèse Jean-Luc Reboud a gardé son intérêt pour les problèmes de la mécanique des fluides. Il a stimulé cette thèse avec de nombreuses propositions.

Je remercie Christophe Ancey avant tout de m'avoir transmis une partie de sa grande culture scientifique. C'est grâce à lui, que j'ai pu publier mes premiers résultats après deux ans de thèse. J'ai beaucoup apprécié les colloques à Cambridge et San Francisco que nous avons vécus ensemble.

Je suis reconnaissant à Philippe Frey, entre autres, pour son accueil chaleureux quand je suis arrivé à Grenoble. C'est lui qui m'a convaincu de faire une thèse sur le mouvement des billes dans un écoulement. J'ai apprécié le travail fécond fait ensemble, surtout au laboratoire et avec le logiciel de traitement d'images.

Sur ce point je dois beaucoup à l'équipe IMAGe du TSI de Saint-Etienne, notamment à Christophe Ducottet, Nathalie Bochard, Jacques Jay et Jean-Paul Schon. Merci pour leur aide précieuse pour la mise au point de la caméra et des logiciels de traitement d'images.

D'autres personnes ont contribué à ce travail notamment sur le plan expérimental. Je remercie Frédéric Ousset, Christian Eymond-Gris, et Hervé Bellot pour leur disponibilité. Une grande partie de notre travail commun a été consacrée à améliorer le distributeur de billes. Ce mémoire montre que l'effort a porté ses fruits.

Dans le cadre de ma thèse, j'ai eu le plaisir de co-encadrer le stage de DEA de Magali Jodeau. Nous avons fait un grand nombre d'expériences ensemble et des traces de son travail sont visibles dans le $5^{ème}$ mais aussi dans le 1^{er} chapitre de ce mémoire.

La bonne ambiance au sein de l'unité ETNA du Cemagref est en outre due à Didier Richard et Mohamed Naaim qui ont aussi contribué au bon déroulement de cette thèse. De nombreuses autres personnes de l'unité

m'ont aidé, donné des idées, encouragé, et adressé des mots en allemand. Je pense surtout à: Guillaume Bernard, David Bertrand, Roland Burnet, François-Xavier Cierco, Huguette Collet-Mattras, Françoise Gay, Alain Gérard, Martine Girier, Stéphane Lambert, Nicolle Mathys, Maurice Meunier, Florence Naaim et Alain Recking, mais la liste est incomplète.

Dû à la repartition des bureaux, mon contact avec les collègues de l'unité E(P)M était très intensif, merci pour tous les coups de main. J'ai apprécié les pauses passées ensemble avec mes voisins: Frédéric Berger, Françoise Dinger, Luuk Dorren, Jean-Philippe Falcy, Céline Le Hir, Véronique Magnin, Laurence Penelon et Freddy Rey.

J'ai eu le plaisir de faire de la musique avec mes collègues et je garde un bon souvenir des répétitions et de nos "concerts" à la fête du Cemagref. Notamment les nombreux stagiaires contribuent à la bonne ambiance au Cemagref, je ne les cite pas tous ici et m'en excuse.

Je voudrais remercier Eric Barthélémy et Philippe Sechet de l'ENSHMG de m'avoir permis de donner des TP, ce qui m'a incité à réfléchir à quelques problèmes de la mécanique des fluides plus intensément et à améliorer mon français oral en travaillant avec les étudiants.

Un grand merci à tout ceux qui ont contribué à améliorer mon travail en relisant le mémoire de thèse (notamment Matthieu de Linares) et en posant des questions pertinentes lors des colloques et des présoutenances. Je suis reconnaissant de l'aide à préparer mon pot de thèse, vielen Dank auch meinen Eltern, deren Bier hier sehr gut ankam. Merci à mes amis de Grenoble et d'ailleurs pour leur soutien pendant ces trois ans. Pour finir, je voudrais remercier tous les futurs lecteurs de ce mémoire, en espérant que ce travail vous apporte quelque chose.

Bonne lecture, enjoy it!

Tobias Böhm, Grenoble en mars 2005.

Tobias Böhm
Cemagref de Grenoble
Unité de recherche Erosion Torrentielle, Neige et Avalanches
Dom. univ., BP 76, 38402 St Martin d'Hères, France
tobias.boehm.1976@web.de
http://people.grenoble.cemagref.fr/pagesperso/TBoehm/TobiasBoehm.htm

Contents

List of figures[3] **15**

List of tables **17**

Nomenclature **19**

Introduction **23**

1 Approaches to bed load transport **27**
1.1 Introduction 27
1.2 Description of the problem 28
1.2.1 Phenomenological description 28
1.2.2 Physical description 29
1.3 Bibliographic review 33
1.3.1 Empirical approaches 33
1.3.2 Alternative approaches 35
1.3.3 Particle simulations 36
1.4 Conclusion 41

2 Experimental facilities and techniques **43**
2.1 Introduction 43
2.2 Channel 44
2.3 Water supply 47
2.4 Solid supply 48
2.5 Experimental procedures 50
2.5.1 Fixed bed 50
2.5.2 Mobile bed 50
2.6 Camera 52

[3]This document is assumed to be fully comprehensible if printed in black and white. Color was used, however, in many figures to increase clarity.

2.7 Conclusion 54

3 Image and data processing **57**
3.1 Introduction 57
3.2 Image preprocessing 59
3.3 Detection of the water free surface 61
3.4 Detection of the particle positions 64
3.5 Particle tracking 67
3.5.1 Overview 67
3.5.2 Initial step 67
3.5.3 Iteration steps 69
3.5.4 Trajectories 71
3.6 State of movement and bed line 72
3.6.1 Definition of the state of movement 72
3.6.2 Definition of the bed line 74
3.7 Conclusion 75

4 Fluctuations of the solid discharge **77**
4.1 Introduction 77
4.2 Experimental conditions 78
4.3 Dimensionless numbers 80
4.4 Experimental results 82
4.4.1 Smooth bottom (experiment A) 83
4.4.2 Corrugated bottom (experiment B) 88
4.4.3 Ordered mobile bed (experiment C) 91
4.4.4 Disordered mobile bed (experiment D) 96
4.5 Conclusion 100

5 Influence of flow rate and slope **103**
5.1 Introduction 103
5.2 Variation of the flow rate 104
5.2.1 Effects on the flow parameters 105
5.2.2 Effects on the solid discharge 105
5.2.3 Effects on the transport features 108
5.2.4 Effects on the bead propagation 110
5.3 Variation of the channel slope 116
5.3.1 Effects on the flow variables 118
5.3.2 Effects on the transport features 122
5.4 Experimental limits 126
5.4.1 Constraints of the solid discharge 128

5.4.2 Constraints of the water discharge 128
5.5 Conclusion 130

6 Conclusion **133**
6.1 Summary of the main results 133
6.2 Potential of the experimental facilities 136
6.3 Impact of the results 137

A Theoretical approach for experiment B **139**

B Water and bed surfaces **143**

C Solid discharge **149**
C.1 Fourier transform 149
C.2 Alternative definitions 150

D Résumés des chapitres en français **155**
D.1 Approches en transport solide par charriage 157
D.2 Dispositif et techniques expérimentaux 158
D.3 Traitement d'images et de données 158
D.4 Fluctuations du débit solide 159
D.5 Influence du débit et de la pente 159
D.6 Conclusion 160
D.6.1 Résumé des résultats principaux 160
D.6.2 Potentiel du dispositif expérimental 162
D.6.3 Apport des résultats 164

References **167**

List of Figures

1 Photo of a torrent. 24

1.1 Sketch of the different sediment transport phenomena. 30
1.2 Definition sketch of the problem. 31
1.3 Forces exerted on a particle in a flow. 38

2.1 Photo of the experimental setup. 45
2.2 Sketch of the experimental setup. 46
2.3 Details of the four different channel bases used. 47
2.4 Bead supply system of the channel. 49
2.5 Scales for measuring the bed and water elevation. 52
2.6 Perpendicularity check. 53
2.7 Inclination check. Calculation of the scaling factor. 54
2.8 Images of particle transport. 55

3.1 Interface of the image-processing software Wima 59
3.2 Flowchart of image and data processing. 60
3.3 Detection of the water line. Original images. 61
3.4 Detection of the water line. Image-processing steps. 63
3.5 Elevation of the water free surface $w_f(x,t)$. 64
3.6 Detection of the particle positions. Original images. 65
3.7 Detection of the particle positions. Image-processing steps. . 66
3.8 Initial time step of the particle-tracking algorithm. 68
3.9 Iteration time step of the particle-tracking algorithm. 70
3.10 Visualization of the particle trajectories. 72
3.11 Sketch defining the state of movement and the bed line. . . . 73
3.12 Elevation of the bed surface $b_s(x,t)$. 74

4.1 Images of the particle transport for experiments A–D. 79
4.2 Time variation of the solid discharge for experiments A–D. . 84
4.3 Autocorrelation functions for experiments A–D. 85

4.4 Empirical probability density functions for experiments A–D. 85
4.5 Pdf of the solid discharge $\dot{n}$ for experiment A. 87
4.6 Normalized intercorrelation functions of the solid discharge. . 88
4.7 Probability distributions of N. 90
4.8 Pdf of the solid discharge $\dot{n}$ for experiment B. 90
4.9 Pdf of the solid discharge $\dot{n}$ for experiment C. 92
4.10 $\dot{n}_y(y)$ for experiment C. 94
4.11 Pdf of the contact angle φ for experiments C and D. 95
4.12 Pdf of the solid discharge $\dot{n}$ for experiment D. 96
4.13 $\dot{n}(y)$ for experiment D. 98
4.14 Bead propagation in the plane (x, t) for experiment D. 99
4.15 Downward and upward steps in experiment D. 101

5.1 Solid discharge $\dot{n}$ as a function of q_w 107
5.2 $\dot{n}_y(y)$ for experiments E10. 109
5.3 Bead propagation for experiment E10-6. 111
5.4 Series of rolling particles. 112
5.5 Liftoff and settling for experiment E10-6. 114
5.6 Bead propagation for experiment E10-21. 115
5.7 Liftoff and settling for experiment E10-21. 117
5.8 Comparison of the liftoff and settling zones. 118
5.9 Overview of the experiments conducted. 120
5.10 Solid discharge $\dot{n}$ as a function of q_w and $\tan\theta$. 121
5.11 Contribution of the saltating particles κ_s as a function of h/d 123
5.12 Superimposition of the trajectories for different slopes. 125
5.13 Dimensionless solid discharge ϕ_s as a function of N_{Sh}. 127
5.14 $\kappa_s\phi_s$ as a function of N_{Sh}. 127

B.1 Elevation of the water free surface $w_f(x, t)$. 144
B.2 Elevation of the bed surface $b_s(x, t)$. 144
B.3 Pdf of the water surface w_f and the bed surface b_s. 145
B.4 Autocorrelation diagram of w_f. 146
B.5 Autocorrelation diagram of b_s. 147
B.6 Intercorrelation diagram of w_f and b_s. 148

C.1 Fourier transform of the solid discharge 150
C.2 Sketch of the trajectories in the (x, y, t) space. 151
C.3 Two additional definitions of the solid discharge. 152
C.4 Normalized autocorrelation functions of $\dot{n}_R(t)$ 153
C.5 Normalized intercorrelation functions of $\dot{n}_R(t)$ 154

List of Tables

2.1 The camera's three different acquisition modes. 54

3.1 Association table for the initial time step. 69
3.2 Association table for an iteration time step. 69
3.3 Example for a table of trajectories. 71

4.1 Conditions of experiments A–D. 79
4.2 Flow characteristics and dimensionless numbers (exp. A–D). 81

5.1 Flow characteristics for $\tan\theta = 10\%$ and varied $\dot{n}$. 106
5.2 Flow characteristics for varied $\tan\theta$ and $\dot{n}$. 119
5.3 Summary of the experiments conducted an those that failed . 128

Nomenclature

Symbol	*Unit*	*Variable*	*Page*
A	m^2	element of the bed surface	32
a	m	particle radius	48
b_s	m	bed surface elevation	31, 74
C_D	-	drag coefficient	83
C_f	-	Chezy friction coefficient	31
C_p	-	packing fraction	94
C_s	-	volumetric solid concentration of the flow	81
D	-	dimensionless particle diameter	81
d	m	particle diameter	48
d_{90}	m	diameter for which 90% (mass) of the sediment particles are finer	34
d_c	m	diameter of a half-cylinder	46
d_n	m	distance to the next neighbor of a bead	73
F	kg m/s^2	force exerted on the particle	37
f	frames/s	frame rate	53
Fr	-	Froude number	80
g	m^2/s	gravity acceleration	30
h	m	water depth	31, 75
h_l	-	mean dimensionless leap height	104
I	-	correlation coefficient	85
K_s	$m^{1/3}/s$	Strickler coefficient	105
L	m	window length	82
l_l	-	mean dimensionless leap length	104
m	kg	particle mass	37
m'	kg	buoyant particle mass	83
N	beads	number of particles in motion	82

Symbol	*Unit*	*Variable*	*Page*
N'	beads/pixel	number of particles that passed during the sequence	124
$\dot{n}$	beads/s	solid discharge or transport rate	82
$\dot{n}_0$	beads/s	injection rate of the particle supply	48
N_l	leaps	number of leaps detected	104
N_r	beads	number of rolling particles in the observation window	128
N_s	beads	number of saltating particles in the observation window	128
N_{Sh}	-	dimensionless shear stress or Shields number	32, 80
N'_{Sh}	-	modified Shields number	34
$N_{Sh,c}$	-	critical Shields number	32
q_c	m^2/s	critical transport rate corresponding to incipient motion	51
q_s	m^2/s	bed load transport rate per unit width	31, 48
$\hat{q}_s$	m^2/s	initial guess for q_s	51
Q_w	m^2/s	water discharge	47
q_w	m^2/s	water discharge per unit width	30, 47
r	m	radius	-
r_D	beads/(s m^2)	deposition rate	35
r_E	beads/(s m^2)	entrainment rate	35
Re	-	Reynolds Number	80
Re_p	-	particle Reynolds Number	80
R_h	m	hydraulic radius	80
s	m/pixel	scaling factor	53
t	s	time	-
u_f	m/s	fluid velocity	31
u_i	m/s	streamwise velocity component of a particle	82
$\mathbf{u_p}$	m/s	particle velocity vector	73
u_r	m/s	mean x-velocity of a particle in the rolling regime	93
u_s	m/s	mean x-velocity of a particle in the saltating regime	93
u_t	m/s	threshold velocity between rest and rolling	73

Symbol	*Unit*	*Variable*	*Page*
W	m	channel width	47
w_f	m	water free surface elevation	61
x	m	horizontal coordinate	30
y	m	vertical coordinate	30
Δ_{Fr}	-	variation scale of Fr	80
ε	-	threshold value	73
θ	deg	channel inclination angle	30, 44
κ_r	-	contributions of the rolling beads to $\dot{n}$	104
κ_{re}	-	contributions of the resting beads to $\dot{n}$	104
κ_s	-	contributions of the saltating beads to $\dot{n}$	104
λ	m	distance between two moving particles	82
μ	-	average number of particles in the observation window	88
ν	m^2/s	water kinematic viscosity	48
π	-	mathematical constant	-
ρ_p	kg/m^3	particle density	48
ρ_f	kg/m^3	water density	48
σ_X	same as X	standard deviation of the variable X	-
τ	kg/(s m)	total bottom shear stress	33
τ_0	kg/(s m)	fluid shear stress at the bed	32
τ_c	kg/(s m)	critical bed shear stress of incipient motion	33
ϕ_s	-	dimensionless solid discharge	126
φ	deg	contact angle	95
ω_0	1/s	frequency of the particle supply	89

Introduction

Floods of mountain rivers are distinguished from other flood events by their sudden formation and the transport of large quantities of sediment by water [Bes96]. An example is the flood of the Saltina in Brig (Switzerland) in 1993. Here, the transported sediment obstructed a bridge in the city center, which caused the river to overflow the Old Town, causing the death of two persons. Furthermore, the river left an enormous deposition of sediment [BAJ94]. This is an example prompting engineers to study sediment transport, although predicting the occurrence of such disasters is often impossible.

Moreover, many water courses have to be regulated to ensure the coexistence of the ecosystem and human infrastructure. In this context, sediment transport is often important since it directly impacts the morphology of watercourses. In France for instance, the bed of the Drôme river has lowered considerably, partly due to the extraction of gravel. Since the incision of the bed endangered the protecting effect of flood banks, strategies to reload the river with sediment have to be developed.

Engineers have therefore paid a great deal of attention to the calculation of the sediment transport rate as a function of the water flow; the results are, however, not completely satisfying. This holds especially for steep sloped torrents (see Fig. 1) where the solid concentration can reach 20% and sediment grains of various sizes are involved (from sand to boulders).

This explains the need for a better understanding of bed load transport (sediment transport near the river bed). To address this issue, researchers have adopted different approaches. Field measurements are the closest to reality. However, usually only a few of the many parameters involved can be measured. Furthermore, these measurements are rarely reproducible since they depend on environmental conditions. Field measurements can thus give only a little insight into the mechanisms of bed load transport. Laboratory experiments can fill this gap: The flow phenomenon of interest is simulated under controlled conditions. The number of influence parameters can be

Fig. 1: Photo of a torrent. Here, flow is running from the front to the back. Photo: Ancey, taken near Pelvoux, Hautes-Alpes, France.

reduced and it is much easier to make precise and extensive measurements.

The purpose of both field and laboratory data is to support the development and improvement of models. These models are then used to predict flow phenomena for given conditions. Most of the problems concerning the free surface flow of water have been solved for a long time; sediment transport is, however, still difficult to model since a liquid and a solid phase are involved. It is particulary complex to approach problems related to incipient motion or the presence of bed forms. Until now, modelers have had to resort to empirical approaches in many places since the mechanisms of bed load transport are insufficiently understood. The importance of validating and verifying transport models with laboratory and field data was recently emphasized by the Task Committee on computational modeling of sediment transport processes of the American Society of Civil Engineers [ASC04].

Our contribution to this issue features the following: The idea of reducing bed load transport to its essential elements prompted us to use a

two-dimensional model channel. In another PhD dissertation [Big01], the motion of a single particle in a water flow on a rough bottom was investigated. For the present study, we developed a particle injection system to supply the channel continuously with sediment (we are using spherical glass beads). The setup makes it possible to control the experimental conditions precisely, notably the supply of water and particles. In consequence, we are able to make sophisticated measurements by means of image processing and to analyze the results from a physical point of view. We will pay special attention to the mobile bed resulting from the incessant exchange between the moving particles and the bed. We will, for instance, see that particles lift off and settle frequently in specific zones conditioned by the bed structure. This microstructural study will thus provide more in-depth insight into transport mechanisms. The results are intended to be used to advance the development of numerical bed load transport models.

Dissertation outline

This PhD dissertation is structured as follows: In the first chapter the problem studied is described and the most important works in this field up to the present are reviewed. Chapter 2 introduces the approach used by presenting the experimental facilities consisting of the channel, the supplies of water and particles, and the camera. The experimental procedures implemented to film bed load transport under equilibrium conditions are detailed. The images of the flow were later processed with two detection algorithms to obtain water elevation and particle positions; trajectories were calculated by means of a particle-tracking algorithm. These algorithms are described in Chapter 3.

The experimental results are presented in the next two chapters: A first study investigates the origins of the solid discharge fluctuations (Chapter 4). To this end, we ran a series of four experiments with a growing number of processes involved. In Chapter 5 we expand to the influence of the flow rate and the channel slope on sediment transport. The results show that especially the slope had an important influence on transport characteristics. The impact of these results is discussed with the intention to stimulate future work.

Chapter 1

Approaches to bed load transport

Abstract: The present study focuses on sediment transport in torrents, which are characterized by steep slopes and occasionally high sediment concentrations, including the entrainment of coarse particles. We investigate the sediment transport by a water flow as bed load, i.e., particles rolling or leaping on the bed composed of particles. As both a solid and a liquid phase are present on the bulk scale, the physical approach of the problem is difficult. It is common to consider four variables (solid and water discharges, bed elevation and water depth) as a function of the downstream coordinate and time. Apart from mass balance equations for each of the phases and the momentum balance equation for the fluid, a fourth relation has to be derived to close the set of equations. Engineers usually resort to empirical approaches, which are mostly based on the Bagnold hypothesis. According to this hypothesis, the solid discharge is related to the shear stress exerted on the bed by the fluid if the latter exceeds a threshold value. The failure of the Bagnold assumption for certain problems has renewed the interest in alternative approaches. These include the theoretical description of the fluid-particle system by means of the kinetic theory and the numerical simulation of particle trajectories.

1.1 Introduction

In this chapter we intend to define the scope of the present PhD dissertation. We first introduce the most important terms we will use. Next, the governing equations for a two-phase free-surface flow are presented. The second section

provides a bibliographic review, compiling the most important approaches which are pertinent to our study.

1.2 Description of the problem

1.2.1 Phenomenological description

Torrents

First of all it is important to emphasize that our study is focused on the sediment transport in torrents. Compared to the works on rivers, there are rather few studies devoted to this topic [Kou93, Ric97, Woh00]. An important characteristic of torrents is the steep slope. Bernard [Ber25] suggests to refer to rivers with slopes above 6% as torrents. Several distinct flows occur in torrents which are often classified roughly into debris flows and torrential flows with intense bed load transport. The present document is entirely devoted to the latter flows, which differ by the presence of two separated phases on the bulk scale: a water phase which is interacting with the solid phase (sediment). A further attribute are the large variations of the water flow during the year: Most of the time the water depth of the flow is much lower than it might be expected regarding the channel in the landscape. Sometimes the level rises sensibly and exceptionally the water overflows the usual banks of the torrent.

Sediment transport

Sediment transport is directly related to the water flow or more precisely to the fluid stress exerted on the particles at the bed surface. At low water discharges no sediment particles are moving and the water remains clear. Above a certain threshold (which is hard to specify) particles are entrained by the water flow. The solid concentration of the flow can reach values on the order of 10%, which is far above the typical values for lowland rivers. The grain size distribution of the transported sediment can be extremely wide going from clay, mud, sand and gravel up to boulder. Thus, the diameters of the sediment particles or blocks can reach the same dimensions as the water depth, which entails problems in defining the latter.

In rivers, it is mainly the water discharge that influences the sediment transport, whereas torrent dynamics is governed by a strong interplay between the two phases. Here, erosion or sedimentation can modify the form of the bed essentially in short time periods, which impacts directly on the

water flow. A single flood event can thus cause drastic variations of the cross section, but can similarly affect longitudinal structures.

Transport phenomena

In function of the grain size, different sediment transport phenomena can be observed. Fine particles are mainly transported in suspension (see Fig. 1.1). Here, the particle fall velocity is of the same order as the velocity fluctuations of the surrounding turbulent flow. In torrents, this transport mode has only marginal importance since coarser particles are dominant. These particles, mainly gravel, are transported as bed load, i.e. with frequent contacts to the river bed. Particles transported as bed load can be further classified into:

particles rolling or sliding slowly on the bed,

saltating particles performing small successive leaps,

(see Fig. 1.1). Especially for the case of steep slopes, the particles performing the bed load transport cannot be treated independently of the particles constituting the bed: Moving particles can settle, becoming part of the bed, whereas bed particles can be set into motion. This situation can occur either because of the impact of saltating particles or due to the stress exerted by the water flow. This outlines the complexity of the studied system: The water stream stimulates the solid discharge which modifies the morphology of the bed by erosion and sedimentation processes. This morphology in turn impacts both on the solid and on the water discharge [Ric97]. A strong point of the present study is the consideration of this interaction putting the attention both on bed load and bed particles.

1.2.2 Physical description

Modeling

To approach the phenomenon described from a physical point of view we can use the framework of continuum mechanics. As we are dealing with a two-phase flow of water and solid particles, both fluid mechanics and Lagrangian mechanics are involved. To model a natural system as described above, we are obliged to simplify it. In our study we pay attention only to the sediment transport in the torrential flow, ignoring its formation.

A very common simplification of the physical system is to consider only a two-dimensional flow, neglecting the cross direction of the stream. As torrents are often braided and show a variable width in flow direction this is

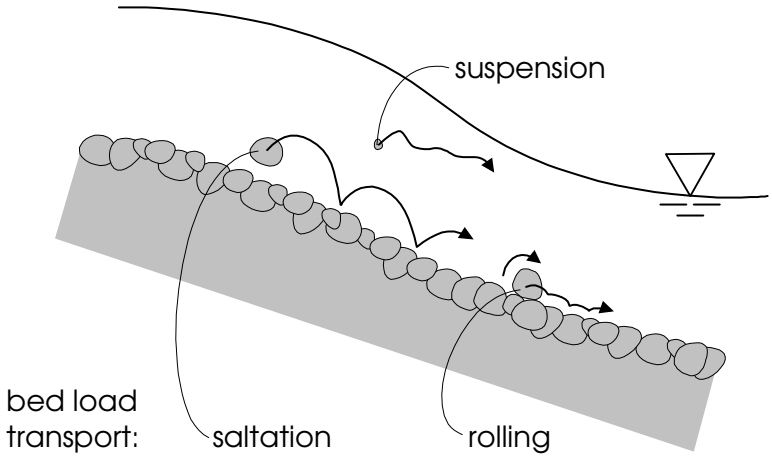

Fig. 1.1: Sketch of the different sediment transport phenomena. Flow is running from left to right in all of the figures of the present document unless otherwise noted.

admittedly an idealization. Furthermore, the equations that we shall derive are averaged in the vertical direction. This simplification is not substantial since we are mainly interested in the integral water and solid discharges and do not focus on the velocity field of the two-phase flow. However, we will see later in the experimental study that it can be helpful to consider profiles in the vertical direction. We will for instance plot the vertical profile of the solid discharge to analyze transport mechanisms.

We finally consider the fluid as incompressible and assume that there is only one sediment material with a uniform density. Note by the way that the flows of our interest are turbulent, the turbulence scale being much smaller than the typical particle size. They are furthermore supercritical, i.e. surface waves do not run upstream. Figure 1.2 sketches the problem in the simplified manner adequate to our study. Even for this case we will see that the set of equations we can derive is not closed in a fully satisfying matter.

The sketch shows that the streamwise and vertical coordinates x and y are rotated by the angle of the mean slope θ with respect to the true vertical direction given by the gravity acceleration g. The four variables of interest are all functions of the time t and the x-coordinate. Two of them are fluxes which we normalize by the channel width (thus measured in m^2/s). These are the water discharge per unit width, $q_w(x,t)$, and the solid discharge

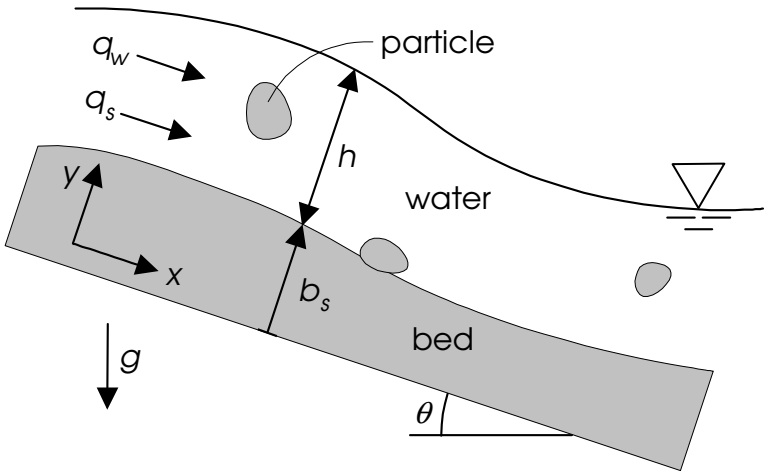

Fig. 1.2: Definition sketch of the problem.

per unit width, $q_s(x,t)$. The other two variables are length scales: the bed elevation, $b_s(x,t)$, and the water depth, $h(x,t)$.

Governing equations

For this case, the momentum and mass balance equations of fluid mechanics are averaged to yield the Saint Venant equations for shallow water (see [BP01] for a similar more detailed derivation):

The continuity equation of the water phase

$$\frac{\partial h}{\partial t} + \frac{\partial h\, u_f}{\partial x} = 0, \tag{1.1}$$

where u_f is the fluid velocity averaged over the water depth, $u_f = q_w/h$.

The momentum flux balance of the water phase

$$\frac{\partial u_f}{\partial t} + u_f \frac{\partial u_f}{\partial x} = g \sin\theta - g \cos\theta \frac{\partial (h + b_s)}{\partial x} - \frac{C_f u_f^2}{h}, \tag{1.2}$$

where the drag term $C_f u_f^2/h$ represents the stress exerted on the fluid by the bed. The friction coefficient C_f is often estimated empirically by the Chezy formula.

Also for the solid phase an equation of continuity can be formulated which is known as the Exner equation. It characterizes the erosion and

deposition of particles affecting the bed elevation. If we neglect the porosity of the bed it reads:

$$\frac{\partial b_s}{\partial t} + \frac{\partial q_s}{\partial x} = 0. \tag{1.3}$$

It is formally possible to establish a momentum balance equation for the solid phase, but, in practice, this equation offers little interest because it cannot be solved even approximately. The crux of the issue lies in the strong nonlinearities in the fluid-particle interplay and the occurrence of different motion regimes. Hence, to close the system of partial differential equations with four unknowns, most attempts over the last decades have been based on a scalar relation for the solid discharge as a function of other flow variables:

$$q_s = q_s(q_w, \theta, \ldots), \tag{1.4}$$

which means that the solid phase is the slave of the flow phase: any change in the fluid flow rate instantaneously entails a change in the solid discharge.

Shields

Especially τ_0, the shear stress exerted on the bed by the fluid, turns out to be an important parameter on the right hand side of equation (1.4). This stress determines the number of bed particles that are set or kept in motion. Since the fluid is turbulent, τ_0 fluctuates and is difficult to measure. An approximation can be obtained if we consider equilibrium, neglect velocity fluctuations and assume furthermore that the flow is dilute. In this case, on each surface element A of the bed leans the mass $\rho_f h A$ where ρ_f is the fluid density. The drag force corresponds then to the x-component of the weight: $F_D = \sin\theta\, g\rho_f h A$. The shear stress yields in this case $\tau_0 = F_D/A = \rho_f g h \sin\theta \approx \rho_f g h \tan\theta$ (for small θ). The drag force competes with a force proportional to the submerged weight of the particle (of the diameter d and the density ρ_p): $F_G = (\rho_p - \rho_f) g \pi d^3/6$. The ratio of these forces is known as the dimensionless shear stress or Shields number:

$$N_{Sh} = \frac{F_D}{F_G} = \frac{\tau_0}{(\rho_p - \rho_f) g d}, \tag{1.5}$$

or $N_{Sh} = \rho_f h \tan\theta / ((\rho_p - \rho_f) d)$ if we accept the approximation for τ_0. By the means of laboratory experiments using near-uniform grains, Shields found that transport occurred only when this number exceeded a critical value, $N_{Sh,c}$ [Shi36]. The diagram of the critical Shields number plotted as a function of the particle Reynolds number (or alternatively the dimensionless

particle diameter) is known as the Shields diagram [Jul94]. For the case of coarse particles different authors found threshold values in the range of 0.047–0.06 which reveals the difficulty in defining a single threshold for the particle transport [BM97].

Even if we accept an uncertainty for the incipient motion, the problem of finding a solution to eq. (1.4) still remains. A bibliographic review shows that most of the proposed solutions are at least partially based on empirical considerations. Compared to laboratory and field measurements several of these bed load formulas give satisfying results as long as the conditions of the simulation do not differ too much from those which served to establish the respective formula. In a more general case, however, these equations yield poor results, notably for flows on arbitrarily sloping beds or for bed load transport close to the threshold of motion. In this context, the next section reviews the most important empirical approaches but presents as well contributions aiming to provide the problem with a more physical foundation.

1.3 Bibliographic review

1.3.1 Empirical approaches

Bagnold

Most of the existing empirical bed load formulas are based on the Bagnold hypothesis [Bag56]. Similarly to Shields, Bagnold introduces a threshold parameter, the critical shear stress τ_c to characterize the incipient movement of bed particles. Moreover, he assumes that for bed load equilibrium the fluid shear stress at the bed τ_0 equals τ_c. Bagnold identifies the difference $\tau - \tau_c$, the amount by which the total bottom shear stress exceeds the critical stress, as the determining variable for the areal entrainment of bed load particles. By this means, the equilibrium transport rate q_s can be calculated theoretically:

$$q_s \propto (\tau - \tau_c)^{3/2} \text{ for } \tau > \tau_c,\ q_s = 0 \text{ otherwise.} \tag{1.6}$$

Due to the absence of other practicable approaches this hypothesis entered into most of the available empirical transport formulas and simulation codes.

Meyer-Peter

One of the most widely used of these formulas is the Meyer-Peter formula [MPM48]. It relates the dimensionless solid discharge ϕ_s to the excess of the

Shields number to a critical value:

$$\phi_s = \frac{q_s}{\sqrt{(\rho_p/\rho_f - 1)gd^3}} = 8(N_{Sh} - N_{Sh,c})^{3/2}. \tag{1.7}$$

Furthermore, Meyer-Peter provided an equation to calculate the Shields number N_{Sh} as a function of roughness coefficients of bed and particles as well as $q_w, h, \tan\theta$ and d. The empirical constants of eq. (1.7) (the coefficient 8 and the critical Shields number $N_{Sh,c} = 0.047$) were obtained by correlating bed load experiments run at slopes up to 2.2%. The formula is therefore not adapted for the case of sediment transport at steep slopes, i.e. for flows in torrents.

Smart and Jaeggi

The work of Meyer-Peter has been extended to steeper slopes by Smart and Jaeggi [SJ83]. Their formula is based on experiments at slopes within a range of 3 to 20%:

$$\frac{q_s}{q_w} = 4\left(\frac{d_{90}}{d_{30}}\right)^{0.2} \frac{\tan^{1.6}\theta}{\rho_p/\rho_f - 1}\left(1 - \frac{N'_{Sh,c}}{N_{Sh}}\right). \tag{1.8}$$

This equation takes into account the grain size distribution of the sediment since it is of special importance for steep slopes: d_{90} is the diameter for which 90% (mass) of the sediment particles are finer, d_{30} is defined in the same way. The critical Shields number is modified ($N'_{Sh,c}$) to take into account the effect of the slope. To obtain the Shields number, the water depth has to be known, but in the case of steep slopes its calculation is not straightforward.

Rickenmann

The Rickenmann formula [Ric91] avoids this drawback introducing a critical water discharge instead of a critical shear stress. Its coefficients are based on the experiments of Meyer-Peter and of Smart and Jaeggi which were completed by Rickenmann's own experiments:

$$q_s = 12.6\left(\frac{d_{90}}{d_{30}}\right)^{0.2} \frac{\tan^2\theta}{(\rho_p/\rho_f - 1)^{1.6}}(q_w - q_c). \tag{1.9}$$

The critical water discharge q_c can be calculated as a function of $\rho_f, \rho_p, g, d_{50}$ and $\tan\theta$ without knowing the flow parameters q_w and h. However, this formula is only valid for bed load transport far above the threshold of motion. In the following this formula will be applied to our case (see §2.5.2, §5.2.2, and §5.3.1).

1.3.2 Alternative approaches

Failure of the Bagnold assumption

The presented transport formulas are widely used in hydraulic engineering. For steady uniform or gently varying flows, they describe the sediment transport correctly, as is shown by confronting to laboratory or field measurements. For more general flow conditions they yield poor results. This is why the Bagnold hypothesis on which these empirical formulas are based has been sporadically criticized over the years. For instance, if bedforms are interpreted as resulting from a loss of linear stability in the coupled fluid-solid system, the Bagnold assumption fails to capture the necessary physics since the resulting equations of motion do not show any instability [BP01]. Recently, Seminara *et al.* [SSP02] proposed to abandon the Bagnold hypothesis. They show that for equilibrium bed load transport on beds with traverse slopes the fluid shear stress τ_0 exceeds the critical stress τ_c. The areal particle concentration, no matter how large, can in this case not reduce the fluid shear stress to the critical value.

Einstein

The failure of the Bagnold assumption has renewed the interest in a better understanding of the physical mechanisms of bed load transport. An alternative approach takes its roots in the work of Einstein [Ein41, Ein50]. Einstein assumes that a distinct condition for the beginning of transport does not exist. He thus suggests to abandon the "critical parameters" turning to a probabilistic description of the problem. Even distinctive bed load transport is according to him caused by velocity fluctuations of the flow and does not result from an equilibrium in the momentum transfer between solid and liquid phases. Einstein defines the entrainment and deposition rates, r_E and r_D, respectively, which are functions of the flow conditions and bed geometry with the intention to derive the transport rate as the difference between them. Stated more explicitly, this amounts to writing that on a small interval δx, the solid discharge variation is $\delta q_s = (r_E - r_D)\delta x$. The solid discharge at bed equilibrium is the implicit solution to the equation $r_E = r_D$. The full problem of determining how r_E and r_D are related to flow conditions remains unsolved.

In consequence of their work that motivated the abandon of the Bagnold hypothesis [SSP02], Parker *et al.* [PSS03] proposed a new approach which keeps the structure of the fluid-solid interaction near the bed of Bagnold incorporating the structure for entrainment of Einstein.

Jenkins and Hanes

Jenkins and Hanes [JH98] developed an analytical approach, which can be applied to model the transport of grains in a fluid (bed load or sand in air). They considered a steady, fully developed sheet flow, which is a highly concentrated region of grains near a bed that interacts with the turbulent shearing flow of a fluid. The motion of particles was assumed to be governed by their collisional interactions rather than by the velocity fluctuations of the fluid. The authors employed a relatively simple model of the turbulent shearing of the fluid and used kinetic theory for the particle interactions. They solved the balance equations of fluid and particle momentum and of particle fluctuation energy.

The results of this approach include the vertical profiles of the mean fluid velocity, the mean particle velocity, the particle velocity fluctuations, and the particle concentration. Several features of these profiles were compared to measurements of Sumer *et al.* [SKFD96]. These measurements were carried out with coarse particles in a water flume. A regime far above the threshold of motion, but below the occurrence of suspension, was considered, the Shields number within a range of 0.5 to 2.5. Comparing theory and experiments yielded good results.

Different aspects of bed load transport are far too complicated to be described analytically. The problem becomes especially complex for transport near the threshold of motion, at low transport stages ($N_{Sh}/N_{Sh,c} \approx 1$). For flumes with steep slopes furthermore the influence of the water free surface is of great importance since the particle diameter is on the order of the water depth. In the presented approaches the bed load layer has, however, been considered as much smaller than the water depth. Remedy can be expected from experimental and numerical methods which have progressed a lot in the last years, the following paragraph reviews some of these works.

1.3.3 Particle simulations

In the last two decades, the idea to consider bed load transport not as the flux of a continuous phase but as the superposition of the motion of individual particles has gained new attention. This has been without any doubt driven by the fast development of computers, permitting meanwhile to resolve numerically the equations of motion of particles in interaction with the flow. The Newtonian equation of motion makes it possible to calculate

the acceleration of each particle in function of the forces acting on it, it reads (see Fig. 1.3):

$$m\frac{d\mathbf{u_p}}{dt} = \mathbf{F}_G + \mathbf{F}_{AM} + \mathbf{F}_D + \mathbf{F}_L + \mathbf{F}_M + \mathbf{F}_B, \tag{1.10}$$

where m and $d\mathbf{u}_p/dt$ are the particle mass and acceleration, respectively. The forces can be identified as:

buoyant force $\mathbf{F}_G$: the submerged weight of the particle due to gravity,

added mass force $\mathbf{F}_{AM}$: the effect of the fluid displaced due to the particle movement,

drag force $\mathbf{F}_D$: due to the velocity difference between particle and fluid (in direction of this velocity difference),

lift force $\mathbf{F}_L$: due to the velocity difference between particle and fluid (orthogonal to this velocity difference),

Magnus force $\mathbf{F}_M$: additional lift force due to the particle rotation,

Basset history force $\mathbf{F}_B$: arising due to the unsteadiness of the fluid flow close to the particle.

Thus, for each of these forces, the challenge is either to derive an appropriate description or to justify that it can be neglected. Furthermore, the contact forces between particles have to be modelled and the effect of the water free surface on the particle has to be considered where necessary.

The description of the particle motion can be seen as the first step to calculate the bed load transport rate q_s. In a second step, the mean particle concentration in the transport layer has to be evaluated. The transport rate q_s is proportional to the product of the mean particle velocity (x-component) and the concentration. An approach of this type was followed for instance by van Rijn [vR84]. He related q_s to the averaged movement of particles. The transport rate q_s was defined as the product of the saltation height, the particle velocity and the bed load concentration. In the following we present further studies on the motion of individual particles.

Wiberg and Smith

A serious drawback of all these equations is that they are valuable for a limited range of flow conditions. This prompted Wiberg and Smith [WS85]

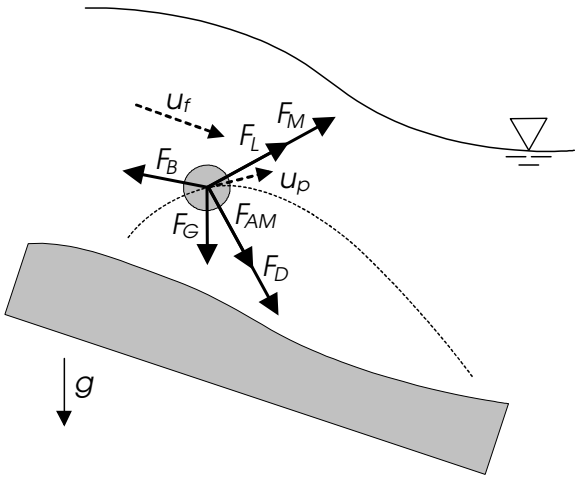

Fig. 1.3: Forces exerted on a particle in a flow.

to develop a more universal bed load model. To simulate the individual movement of saltating particles, they couple the equations of motion of a particle to those of the surrounding fluid providing a numerical solution. The authors consider the two-dimensional motion of a spherical particle exposed to the buoyant, lift, and drag force. These forces are calculated by the use of empirical coefficients (e.g. the drag coefficient) which are known from fundamental experiments. The influence of the Magnus force is tested but not maintained in the final model as it turns out to have little influence on the results. The algorithm provides thus the shape of a particle leap in form of the (x, y)-coordinates as a function of time. To simulate a series of consecutive leaps the model is improved by taking into account the collisions of the considered particle with the bed. The geometry of the impact is here determined by a random number. To calculate the initial velocity of a particle beginning saltation, Wiberg and Smith suppose that the boundary shear stress exceeds a critical value. At this point the model refers to the Bagnold hypothesis.

A second publication by the same authors [WS89] is devoted to apply the simulation model in calculating the particle transport rate. This is done by integrating the product of particle concentration and velocity over the bed load layer. The particle concentration of sediment in the bed load layer can be calculated as the probability to find a particle at a certain elevation. Compared to empirical formulas as the Meyer-Peter formula the transport

model yields good results. One of its advantages is that the model does not contain any scaled parameter without physical meaning.

Niño and García

Niño and García proposed a comparable approach [NG94]. The equation of motion of a saltating particle is averaged over the flow turbulence, the collisions with the bed are modelled stochastically. Friction coefficients are obtained from a parallel experimental study [NGA94]. Herein, the trajectories of coarse particles are analyzed with video-imaging techniques. The leap lengths and heights obtained experimentally agree well with those of the model provided that the lift force is taken into account. The model is then applied to calculate the bed load transport rate reverting to the Bagnold hypothesis. Bed load transport is overestimated which prompts the authors to cast doubts on this hypothesis for the case of coarse sediment.

Schmeeckle and Nelson

The work of Schmeeckle and Nelson [SN03] is initiated by the lack of previous bed load transport models to take into account the strong temporally and spatially variation of the variables involved. Especially for low transport stages ($N_{Sh}/N_{Sh,c} < 3$) it is necessary to consider the effect of the fluctuations of the fluid velocity field on the motion of sediment particles. This is made difficult by the fact that the evolution of the particle bed modifies this velocity field constantly.

Schmeeckle and Nelson developed an algorithm, which directly simulates the motion of a large number of grains by integrating their equations of motion simultaneously. Particles are modelled as spheres (their diameters can be uniform or not) moving in a three-dimensional space with periodic boundary conditions. The buoyant, added mass, drag and contact forces exerted on each particle are considered, in the present version of the model the lift force is neglected. Special care was taken to calculate the fluid forces (drag and added mass) on the particle: In preliminary experiments, the velocity field in the wake of a protruding bed particle was measured by a laser Doppler velocimeter for different configurations. These measurements provided an empirical description of the fluid phase which is used in the simulation algorithm to calculate the fluid forces.

The interaction between moving particles and the bed are modelled in a rather sophisticated way compared to Wiberg and Smith (see above). For each particle in motion the number of contacts to bed particles is considered.

This number changes over the simulation time since rolling particles can lift off and particles in saltation can collide with the bed. The collisions are modelled by a law of an elastic rebound coupled with the viscous damping by the surrounding water. The algorithm takes into account collisions between moving and resting particles whereas the interaction between two moving particles is for the moment excluded.

The simulation results show a good agreement of the transport rate with the empirical bed load formula of Fernandez-Luque. A strong temporal correlation of the transport rate to the fluid velocity is revealed. According to Schmeeckle and Nelson, the saltating regime dominates by far the rolling regime of the particles, rolling is the mere transition phase between rest and saltation.

Bigillon and Ancey

We eventually present the previous work on the mechanisms of bed load transport mechanisms conducted at Cemagref. It is an example for an experimental and analytical investigation at the particle scale. The channel we shall use for the present study (see §2) was already constructed for a previous PhD student. In this work, Bigillon investigated the two-dimensional motion of a single particle in a water flow down a steep channel [Big01]. Her experiments are prototypal of sediment transport on sloping beds. As for the main results, the channel bottom roughness as well as the water free surface revealed to have an important influence on the particle movement. A study on the particle transport modes showed that the saltating motion was dominant for most of the flow conditions. Rolling appeared only in limited ranges as the transition phase between rest and saltation. For steep slopes it disappeared completely.

The investigation on the two motion regimes was carried on and completed with theoretical models by Ancey *et al.* A first publication focuses on the saltation motion [ABF$^+$02]. The critical shear stress $N_{Sh,c}$ for the initiation of motion is determined experimentally. The values found for different flow conditions (the range of $0.001 < N_{Sh,c} < 0.005$ is rather wide) are far below of those typically found for gravel bed experiments ($0.047 < N_{Sh,c} < 0.06$). This is consistent, considering that the test particle is spherical and exposed to the flow on nearly its entire diameter since the bed is fixed. For this reason the flow can set the particle into motion more easily than it the case of a bed composed of particles. Rolling motion occurs in a narrow range of Shields numbers N_{Sh} (typically 0.005–0.01) if N_{Sh} exceeds the value 0.03 saltation is the only transport regime. Furthermore,

the forms of the leaps of this saltating motion are described statistically. Leap length and height reveal to depend on N_{Sh} and the slope. Finally, a simple saltation model evoking the model of Wiberg and Smith is developed. However, the agreement to the experimental results is only qualitative.

The following paper of Ancey *et al.* [ABFD03] is one of the few works devoted to particle transport in the rolling motion. At first, a mean energy balance is formulated to determine under which conditions a particle on a bumpy bottom is set into motion and at which velocity it rolls. This deterministic description confirms that rolling appears in a small range of flow conditions, however, the approach does not capture the stochastic nature of the threshold of motion. Therefore, a second approach is derived considering the state of motion of a particle (rest, rolling, or saltation) as a random variable whose evolution constitutes a jump Markov chain. The model provides the probability for a particle to be in one of these states, a mean particle velocity can be calculated without knowing the state of motion as a function of time. Agreement on the state transitions with the experimental study is encouraging.

1.4 Conclusion

This first chapter intended to provide the reader with the fundament on which this PhD dissertation is based. Sediment transport in flows under steep slopes was first described phenomenologically. By developing a more physical approach to the problem we introduced progressively the most important previous studies in the field. We have seen that the idea to describe bed load transport by means of a threshold of motion is inherent in many of these studies. Shortcomings of this concept have regenerated an interest in the mechanisms of bed load transport. Like some of the works presented in the bibliographic review our study is intended as a step in this direction.

Chapter 2

Experimental facilities and techniques

Abstract: The experimental facility consisted of a narrow, glass-sided channel, 2 m in length. The slope was adjusted in a range from 5% to 20%. The channel was continuously supplied with water and spherical glass beads with a diameter of 6 mm. As the channel was only slightly wider than this diameter, the particle motion was approximately two-dimensional. An obstacle at the channel outlet prompted the particles to settle on the rough channel base. We primarily investigated the case of bed load equilibrium, that is, neither erosion nor deposition of the particle bed over sufficiently long time intervals. Flows were filmed from the side using a high-speed camera allowing to capture the motion of a set of particles (on the order of 100 individuals) for approximately 1 minute.

2.1 Introduction

The main feature of our experimental channel is its small width, which makes it possible to observe the 2D-motion of particles in a flow from the side. The case of dry particles in a similar strongly inclined channel was studied in the PhD dissertation of Azanza [Aza98]. The channel of the Cemagref of Grenoble was constructed in 1999 to study the interaction of particles and water. As described in the last chapter, Bigillon investigated the movement of a single particle in a water stream in her PhD dissertation [Big01].

The "mobile bed", one of the key elements of bed load transport, was not considered in this study. Field observations show that particles can

be entrained and transported by the water stream before settling again. Erosion and sedimentation of particles alternate. To investigate the role of the mobile bed it is thus essential to study not only the interaction between a particle and the fluid but also the interaction between the particles among each other. To observe a set of particles entrained by a water stream under stationary conditions, we supplied the channel continuously with particles. The main focus of the present PhD dissertation was thus the study of the interactions of particles and the mobile bed.

Since we were interested in the rolling and the saltating motion of bed load transport we chose a rather coarse particle size ($\approx$ 1 cm). Spherical particles of uniform size were used to keep the experiments as simple as possible.

We first present the nature of the channel and its water and solid supplies. Afterwards we describe the experimental procedure we followed and the features of the camera.

2.2 Channel

Experiments were carried out in a tilted, narrow, glass-sided channel, 2 m in length and 20 cm in height. Figure 2.1 shows a photo and Fig. 2.2 a sketch of the experimental facility. The channel consisted of an aluminium frame that held two glass panes of 10 mm thickness. It was mounted on a horizontal steel bench with an articulation at the downstream end. The upstream entrance of the channel could be lifted or lowered being connected to a counter balance by a tightrope. The channel slope $\tan\theta$ could thus be adjusted in a range from 5% to 20%, fixing the channel at the desired inclination. We calculated the slope in measuring the distance between the channel frame and the steel bench at two different positions. We verified that the glass panes were vertical and that the steel bench was horizontal with a spirit level.

The bottom of the channel made of stainless flat bar steel was inserted between the glass panes. For the experiments presented in this document we used four different channel bases each of them was 1.98 m long, 6.0 mm thick and approximately 40 mm high. The upstream parts were higher and had triangular shapes (see Fig. 2.2) to prevent water and particles from running upstream. The channel bases were manufactured by laser cutting. They differed by the surface design (see Fig. 2.3):

Fig. 2.1: Photo of the experimental setup. Here, flow is running from the back to the front.

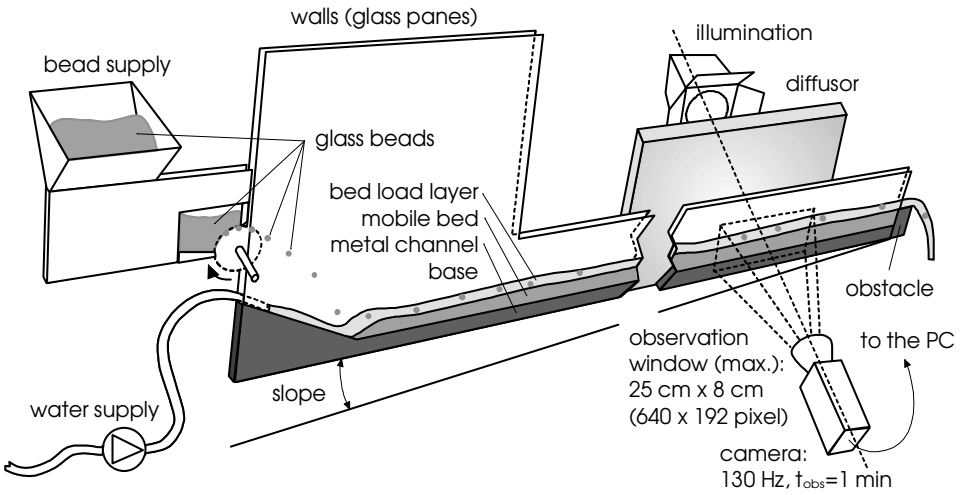

Fig. 2.2: Sketch of the experimental setup (mirror-inverted). Flow is running from left to right in all of the figures of the present document unless otherwise noted.

(a) channel base A was flat and smooth.

(b) channel base B was corrugated, it was made up of juxtaposed half-cylinders (diameter $d_c = 6$ mm).

(c) channel base C consisted of half-cylinders of various sizes. We selected a mixture of three sizes of cylinders: Their diameter d_c could be either 3 mm, 6 mm, or 8 mm.

(d) channel base D consisted of half-cylinders of equal size ($d_c = 6$ mm), but they were arranged on different levels, from 0 to 5.5 mm, by increments of 0.5 mm. These levels were generated using a sequence of uniformly distributed random numbers.

Note that the diameter of the half cylinders d_c matched the particle diameter ($d = 6$ mm, see below). We used these four different channel bases to investigate the fluctuations of the solid discharge under different conditions, in particular with or without the influence of a mobile particle bed (see §2.5.2 for a definition of the term mobile bed). For the study of the influence of different flow conditions we used channel base D systematically.

To make the channel impermeable, we glued a band of foam rubber of rectangular cross section at the lower edge of the channel base. Laterally, we glued two stripes of paper, each one 0.25 mm thick. Next, we inserted the

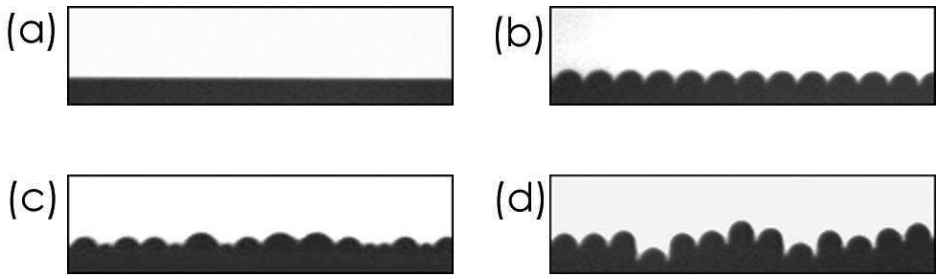

Fig. 2.3: Details of the four different channel bases used (a) A, (b) B, (c) C, and (d) D. Image dimensions: 76 mm × 19 mm.

channel base between the glass panes and clamped them at several positions. At the upper edge of the window panes we used several spacers of 6.5 mm thickness. The channel was thus rectangular, $W = 6.5$ mm wide, which was slightly larger than the particle diameter ($d = 6$ mm). In this way, the particle motion was approximately two-dimensional and stayed in the focal plane of the camera. Actually, the experimental setup made it possible to vary the channel width in the range of 3–25 mm, we kept it constant at 6.5 mm for all the experiments of the present document.

An obstacle could be set at the channel outlet to enable the formation of a particle bed and prevent full bed erosion; its height could be adjusted by increments of 2.5 mm. The procedure used for building the bed is explained in §2.5.2.

2.3 Water supply

Water flowed in a closed circuit. It was collected at the channel outlet in a 70 l reservoir in which we placed a submersible centrifugal pump. The water was pumped to a smaller second reservoir at an elevation of approximately 3 m. In this way, using an overflow pipe, the channel was supplied at a constant pressure head. The water ran successively trough a flow meter and a gate valve, both of nominal diameter 10 mm. We used an electromagnetic flow meter provided by Krohne (France). The flow was transferred from the circular cross section of a hose into the narrow channel by means of a nozzle.

The water discharge Q_w could be adjusted in the range 0.025 to 0.14 l/s, which corresponds to a discharge per unit width q_w from 3.8 to 21.5 × $10^{-3}\,\mathrm{m}^2/\mathrm{s}$. Since we were investigating particle transport under equilibrium conditions a stationary water supply was indispensable. Thanks to the sup-

ply by the elevated reservoir the fluctuations of the water discharge at the channel entrance were low, the flow meter indicated fluctuations for the low frequency domain on the order of ±1%.

We used a coarsely meshed filter at the channel entrance both to retain dirt particles and to dissipate part of the energy of the water flow. A second filter, a finely woven sieve, was placed at the outlet of the channel.

During the experiment, the water was heated to a temperature of 15–25°C due to the lamp of our experimental setup (see §2.6). For our purpose it was sufficient to consider the water density ρ_f and its kinematic viscosity ν as constant, taking the values 1000 kg/m^3 and 1.0×10^{-6} m^2/s, respectively.

The water discharge was limited because of the small diameter of the supply circuit. To reach a higher water discharge we removed flow meter and valve for one experimental run (experiment E7-11, see §5.3). This time we measured for $Q_w = 0.17$ l/s directly after the run using a bucket and a stop watch.

2.4 Solid supply

Colored spherical glass beads with a density ρ_p of 2500 kg/m^3 (provided by Sigmund Lindner GmbH, Germany) were used. Their nominal diameter $d = 2a$ was 6 mm with a tolerance of ±0.3 mm.

The beads were stored in a reservoir (see Fig. 2.2), its upper part was a prism-shaped funnel from which the beads were conducted into a gap to put them in a 2D arrangement. Inside the gap, approximately 8 mm wide, we placed a ramp to make the beads roll towards the channel (see Fig. 2.4). To avoid a jamming of the beads, we attached a vibrator to the reservoir, an electric motor whose rotor was holding an eccentric mass. This mass was chosen ensuring negligible vibrations to the channel.

From the reservoir, the beads were injected into the channel by means of a wheel equipped with 20 hollows on the circumference, as shown in Fig. 2.4. The injection of the beads one by one could be controlled through a plexiglas window in the reservoir. The wheel was driven by a direct current motor via a V-belt. Its rotation speed could be varied by a potentiometer but as well by using pulleys of different diameters at the axis of the transport wheel. The injection rate could thus be varied in a range from $\dot{n}_0 = 5$ to 21 beads per second, with an uncertainty of less than 5%. This corresponded to a solid discharge per unit width q_s of 8.7 to 36.5×10^{-4} m^2/s, q_s being calculated by the relation $q_s = \pi d^3 \dot{n}_0/(6W)$. We measured the solid discharge by clocking the time for a given number of revolutions of the wheel.

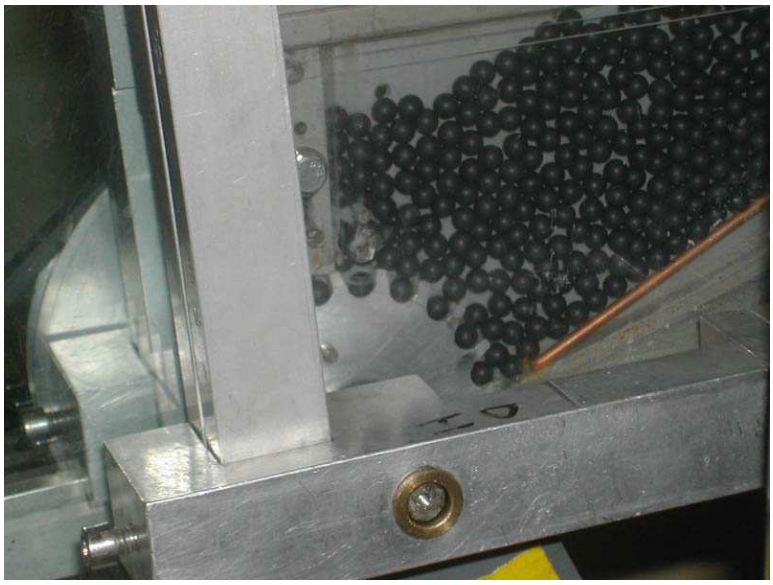

Fig. 2.4: Bead supply system of the channel (transport direction from right to left). The beads were guided by the reservoir to the transport wheel which was equipped with 20 hollows (diameter: 76 mm, width: 4.5 mm). In the background part of the pulley and the V-belt can be seen.

Inside the channel, the impacts of the beads were damped by a piece of foam rubber. We observed slight variations in the bead positions and velocities at the moment of the release from the transport wheel. The beads thus impacted on different points of the channel, which led to nonuniform distances between two consecutive beads.

We collected the beads at the channel outlet in a coarse meshed sieve. It was possible to measure the solid discharge at the channel outlet by counting the beads collected in the sieve in a certain time (30 or 60 s). This was done to check if the system was in equilibrium. The beads were drained for several minutes before putting them back into the reservoir.

The particle supply system was the main element of the experimental facility that was improved during this PhD dissertation. We spent a considerable time to reach a reliable supply with a high injection rate. We started with a transport wheel of 6 hollows and progressed to 12 and 20 hollows. A high injection rate is indispensable to have a sufficient number of particles in motion in the observation window (see §4.4).

2.5 Experimental procedures

2.5.1 Fixed bed

Two experimental runs (see channel bases A and B, in Fig. 2.3(a) and (b) as well as §4) were carried out with a fixed bed and thus were not intended to study erosion and sedimentation phenomena, but to serve as a reference. Here, the experimental procedure was simple because the solid and water discharge could be chosen independently.

2.5.2 Mobile bed

In the further experiments water flowed over a "mobile bed" made up of the same particles as those supplied at the channel entrance, allowing exchanges between the moving solid phase and the bed (erosion or deposition).

A bed is said to be mobile when it consists of particles that can be entrained by the stream. Mobile beds were obtained by building a disordered packing of particles along the channel bottom. Disorder was essential as it prevented slipping of entire layers of particles on the upper bed surface, which would have induced artificial erosion conditions. Maintaining disorder in monosized spherical particles is difficult, with severe constraints [BH93], here involving mainly how to create disorder in the packing and the bed thickness. As regards the latter point, channel bases with a random roughness made up of juxtaposed steel half-cylinders were positioned between the channel walls. The arrangement of the particles constituting the bed depended a great deal on how the half-cylinders of the base were designed and disposed (see §2.2 and Fig. 2.3(c) and (d)).

Selecting either of these channel bases had a substantial influence on the short-range geometrical arrangement of the particles constituting the bed because the bed was thin. For thick beds (typically, whose thickness exceeded 5–6 particle diameters), a regular, crystalline arrangement was observed along the upper part of the bed. This is expected since it is well-known that the disorder range induced by a defect in a crystalline arrangement of monosized spherical particles is a few particle diameters [BH93]. Therefore, in order to be able to control the order in the particle arrangement, we built beds whose thicknesses did not exceed five particle diameters.

Before filming the flow, water and solid supply had to be adjusted in a preliminary procedure. A particle bed was built along the channel base, which remained stationary on average. To that end, an equilibrium between the water discharge, solid discharge, and channel slope was sought. It was

most convenient to find out the equilibrium water discharge as a function of the other variables: $q_w = q_w(\dot{n}_0, \tan\theta)$. An auxiliary equilibrium condition was the uniformity of the bed, i.e. a constant bed elevation along the channel. We developed the following experimental protocol to reach this equilibrium:

Water discharge: The water discharge q_w was set to a constant value adjusting the valve.

Solid discharge: An obstacle (approximately 20 mm in height) was positioned at the downstream end of the channel. The solid discharge $\dot{n}_0$ at the channel entrance (or the injection rate) was set to a constant value. An initial guess $\hat{q}_s$ for the solid discharge at equilibrium was obtained using an empirical sediment transport equation (see eq. (1.9) in §1.3.1 and [Ric91]). For our case (uniform sediment), this equation can be simplified into the following form:

$$\hat{q}_s = 6.27\,(q_w - q_c)\,\tan^2\theta, \tag{2.1}$$

where $q_c = 0.128\,\sqrt{g\,d^3}\,\tan^{-1.12}\theta$ (g denotes the gravity acceleration) is the critical water discharge corresponding to incipient motion of particles. The first beads supplied by the feeding system were stopped by the obstacle at the channel outlet and started to form a bed. The bed line rose to the level of the obstacle and beads began to leave the channel. After approximately 10 minutes, the system arrived at bed load equilibrium, that is, there was no more bed deposition or erosion over a sufficiently long time interval.

Uniformity of the bed: In order to make the bed line parallel with the channel base, the water discharge was then adjusted. The bed elevation and the water level could be controlled using scales as shown in Fig. 2.5. They were attached at the back of the channel at several x-positions to assure that the flow was (in the temporal average) independent of x, i.e. that water and bed elevation were the same. Aberrations were tolerated near the channel entrance (influence of the water and particle supply) and the outlet (the water developing a free jet). The perturbing effect of the channel outlet was indeed low, as flow was most of the time supercritical (see Tab. 4.2). In the case the thickness of the bed was not in the range from two to four particle diameters we readjusted the height of the obstacle at the channel outlet.

After several iterations, we arrived at the configuration of a bed that consisted of two to three almost stationary bead layers along the channel, for

Fig. 2.5: Scales attached at the back of the channel allowed us to measure the bed and water elevation at several x-positions. Here, flow is running from right to left.

which the bed line slope matched the channel base inclination. Further evidence of the system equilibrium was obtained by comparing the rate at which the particles were leaving the channel with the particle injection rate. Average equilibrium conditions were sustained over long time periods, basically as long as 30 minutes.

After the acquisition of image sequences with bed load transport we stopped the solid supply. The obstacle at the channel outlet was removed to erode the particle bed completely. Then we filmed the water flow once again, which made it possible to compare the flow depth in presence and absence of particles.

2.6 Camera

The particles and the water stream were filmed using a Pulnix partial scan video camera (progressive scan TM-6705AN). The camera was placed on a tripod, which was fixed on the wall of the laboratory. Its position was 115 cm distant from the channel, approximately 80 cm upstream from the

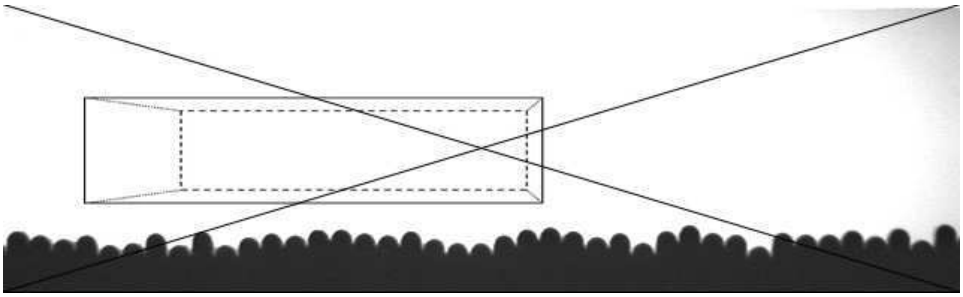

Fig. 2.6: Check if the camera was perpendicular to the channel walls. Schematic view of the cuboid.

channel outlet. A 300 Watt halogen lamp was positioned in the backside of the channel. Between the lamp and the channel, we placed a diffusor to illuminate the complete filmed area fairly uniformly. The aperture of the camera was adjusted manually to optimize the contrast of the image.

Before each experimental run, we verified that the camera was perpendicular to the glass panes. Therefore, we placed a cuboid on the channel wall in the center of the image verifying that none of the lateral surfaces could be seen (see Fig. 2.6). Next, we inserted a long plastic bar into the channel (see Fig. 2.7). It was supported only by the highest bumps of the channel base and allowed us thus to verify that the camera was inclined at the same angle as the channel. A calibration target attached to the plastic bar made it possible to calculate the scaling factor s of the images, 1 pixel corresponded to 0.387 mm both in the x- and in the y-direction ($s = 0.387$ mm/pixel). As we did not change the distance between channel and camera this scaling factor was constant for all the experiments presented in this document.

The camera offered three different acquisition modes as shown in Tab. 2.1. We chose the partial scan mode of 192 lines as it provided a frame rate sufficient for our purposes and a y-resolution which made it possible to capture both channel base and water free surface for the flow conditions that we were investigating. We measured the frame rate by filming a stop watch and found the value $f = 131.3$ fps. An area approximately 25 cm in length and 8 cm in height was filmed which corresponded to 40×12 bead diameters. The image height was later reduced to accelerate image processing. An exposure time of 0.2 ms was chosen.

Once bed equilibrium was reached, we acquired image sequences each one during approximately 1 minute. The images were digitalized (256 gray levels) by a Matrox Meteor II card and initially stored in the computer

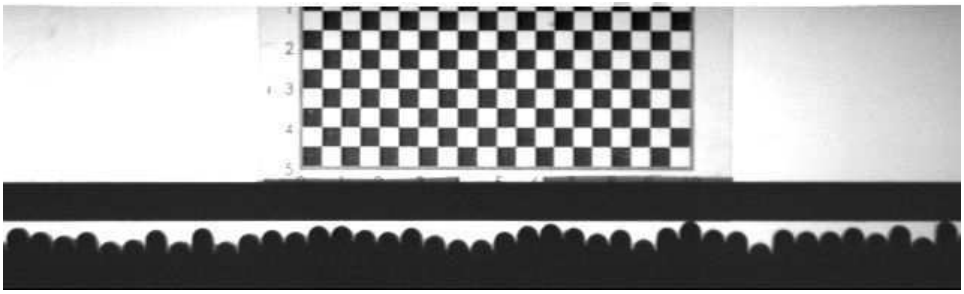

Fig. 2.7: Check if the camera was inclined at the same angle as the channel. Calculation of the scaling factor s, 1 square $\sim 5 \times 5$ mm^2.

mode	normal	partial scan 192	partial scan 100
x-resolution (pixel)	640	640	640
y-resolution (pixel)	480	192	100
frame rate f (Hz)	60	131.3	210

Tab. 2.1: The camera's three different acquisition modes.

RAM. Hence each sequence was limited to 8000 images. The images were then saved on hard disc in the tagged image file-format (tif), occupying approximately 1 GB of disk space. Figure 2.8 shows a small part of a typical image sequence. A close examination allows us to identify particles at rest as well as in rolling or saltating motion.

2.7 Conclusion

In this chapter, our experimental setup to study the dynamics of particle transport in a turbulent water stream was described. We used an inclined channel in which the particle and water supplies at the inlet were controlled accurately. This facility was intended to idealize the sediment transport in steep gravel-bed rivers.

Compared to a usual laboratory channel used for sedimentation studies [NGA94], our experimental setup differed by several characteristics. The channel was rather short but the main drawback was the small channel width compared to the particle diameter. As particles, we used spherical and monosized reproducing sediment particles found in rivers only in a strongly idealized way. However, these limitations were necessary as they allowed

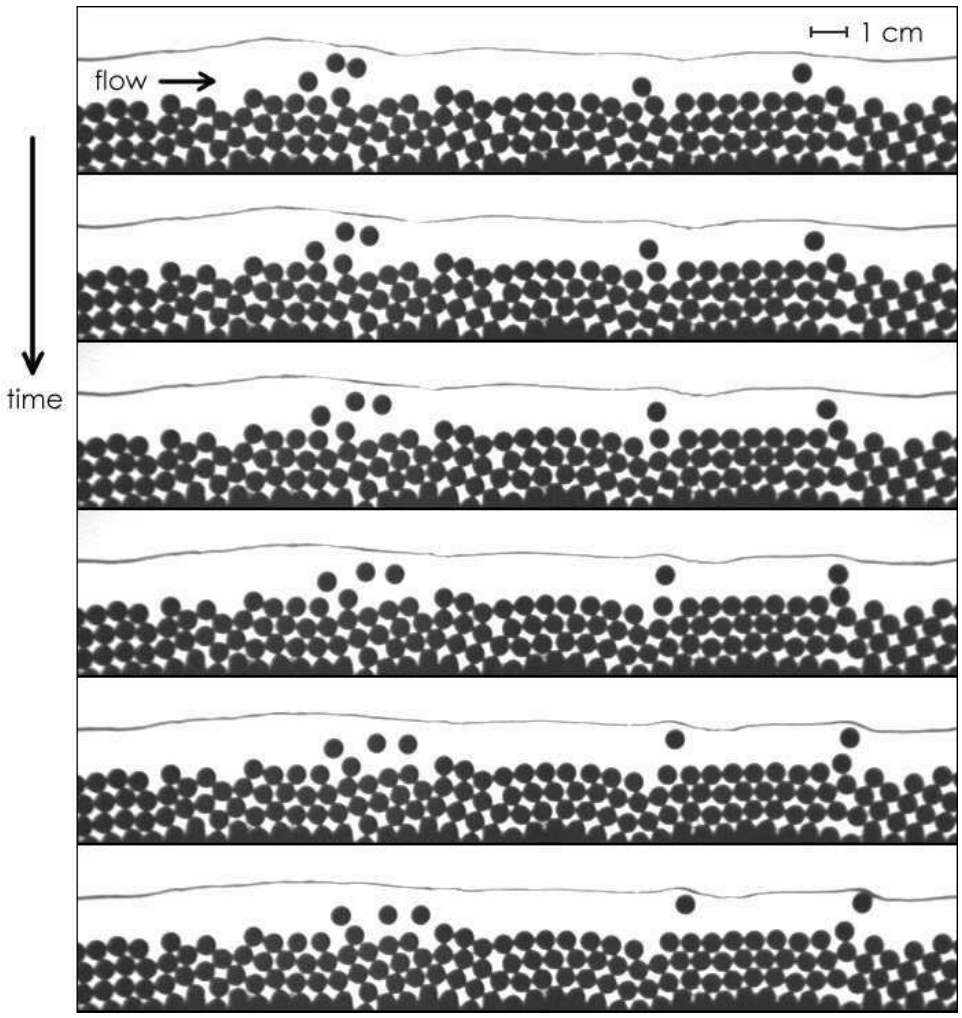

Fig. 2.8: Images of particle transport. Image dimensions: 25 cm × 5 cm (resolution: 640 × 120 pixels); exposure time: 0.2 ms; frame rate: $f = 129.2$ Hz, channel inclination: $\tan\theta = 10\%$. For experimental conditions, see Tab. 4.2, experiment D.

us to capture the entire movement of a set of particles (on the order of 100 individuals). We paid special attention to work under equilibrium conditions and controlled the boundary conditions exactly. To our knowledge, this microstructural investigation has never been conducted previously.

Chapter 3

Image and data processing[1]

Abstract: Images were analyzed using algorithms that combined image-processing operations of the Wima software. The water free surface was detected using its slim form; missing portions were inter- or extrapolated. Positions of the bead mass centers were detected by comparing the filmed images with the image of a model bead. The correlation maxima were calculated to obtain the bead positions. Resulting uncertainty on the water line and bead position was less than 1 pixel, or 0.4 mm. We developed a particle-tracking algorithm to calculate the trajectories of each of the filmed beads step by step. The state of movement of a particle was defined by considering that each bead was either in a resting, rolling, or saltating regime. Defining the bed surface profile to be the broken line linking the top points of the uppermost resting or rolling beads made it possible to calculate the water depth.

3.1 Introduction

The emergence of powerful computers during the last fifty years has affected many areas of our life and did not spare the research in fluid mechanics. More and more sophisticated models can be used in flow simulations. In the meantime, experimental techniques have progressed a great deal. The use of computers allows us to acquire and process huge amounts of experimental data. In particular, methods based on image processing are currently enjoying great popularity. Video processing has been used for a variety of problems such as surveillance, scene monitoring [Cou97], dis-

[1]Publication submitted to *Experiments in Fluids* [BFD$^+$].

tortion measurement, and particle image velocimetry [NKH89, WG91]. In the field of bed load transport, several authors have used photography and video techniques to investigate the motion of saltating particles in a flow [HH96a, HH96b, LCYL00, NGA94].

In the same context the research unit *Erosion Torrentielle, Neige et Avalanches* of the Cemagref is collaborating with the *Traitement du Signal et Instrumentation* laboratory in Saint-Etienne (France). In this institute, the working group *Image, Modèles, Architecture, Géométrie (IMAGe)* is developing the image-processing software Wima since 1992 (see [Duc94] and Fig. 3.1). The code, which is written in C/C++, is continually evolving. The software is mainly designed for the analysis of gray scale images and image sequences. It offers a variety of processing operations that can be classified into geometrical, logical, arithmetic, convolutive, statistical, and morphological operations. It allows the user to combine these operations in macro commands, an important feature. Furthermore, specific algorithms coded in C language can be integrated into the standard version of the software. At Cemagref, the Wima software was used to derive turbulent velocity profiles with PIV [FR01], to measure the grain size distribution instantaneously at the outlet of a gravel-bedded channel [FDJ03], and to detect the motion of a single particle in the channel described above [Big01, ABF$^+$02, ABFD03].

A flowchart of the image and data processing procedures developed during this PhD dissertation is shown in Fig. 3.2. Although the mere observation of the image sequences made it possible to distinguish some characteristics of the experiment, it was image processing that enabled a quantitative analysis. In this way, the essential information (the particle trajectories and the position of the water line) was extracted from the data with high accuracy. The amount of data was thus considerably reduced, which was a precondition for their interpretation.

The position of the water line can be extracted with classical image-processing operators: image thresholding and morphological operations [GW92]. On the other hand, determining particle trajectories requires specific development: First we had to detect particle positions and second track the particles along the sequence in order to find the trajectories. The problem of object detection and localization in a gray scale image is known as a pattern-matching problem. It is usually solved using correlation techniques. More sophisticated nonlinear operators can also be used [BDJ03]. The problem of tracking particles along a sequence is not trivial. Depending on the hypotheses made on particle displacement, more or less complex approaches have been proposed [SJ87, SS90, Hwa89].

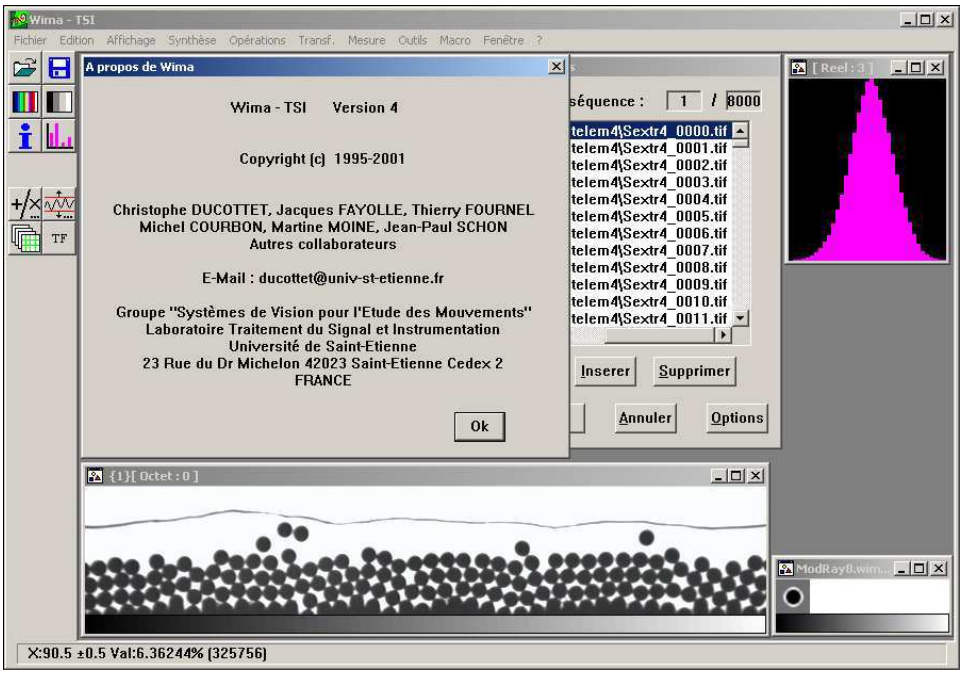

Fig. 3.1: Interface of the image-processing software Wima provided by the *Traitement du Signal et Instrumentation* laboratory in Saint-Etienne, France.

In this chapter, we describe the image processing and the ensuing data processing (see Fig. 3.2). After a preprocessing step, we applied two detection algorithms. Starting from the particle positions, the trajectories and the state of movement of the particles were calculated. The detection of the water free surface served to calculate the flow depth. The output of the processing algorithms was thus the characteristic variables of the experiments such as the solid discharge, the dimensionless numbers used in fluid mechanics (see §4.3), and the water depth. The calculation of these variables which were mostly functions of x and t is not described in this chapter but together with the interpretation in the subsequent chapters.

3.2 Image preprocessing

Depending on the flow conditions, the image height was sometimes much larger than the depth of the two-phase flow and thus contained much redundant information. This prompted us to extract a vertical band of the

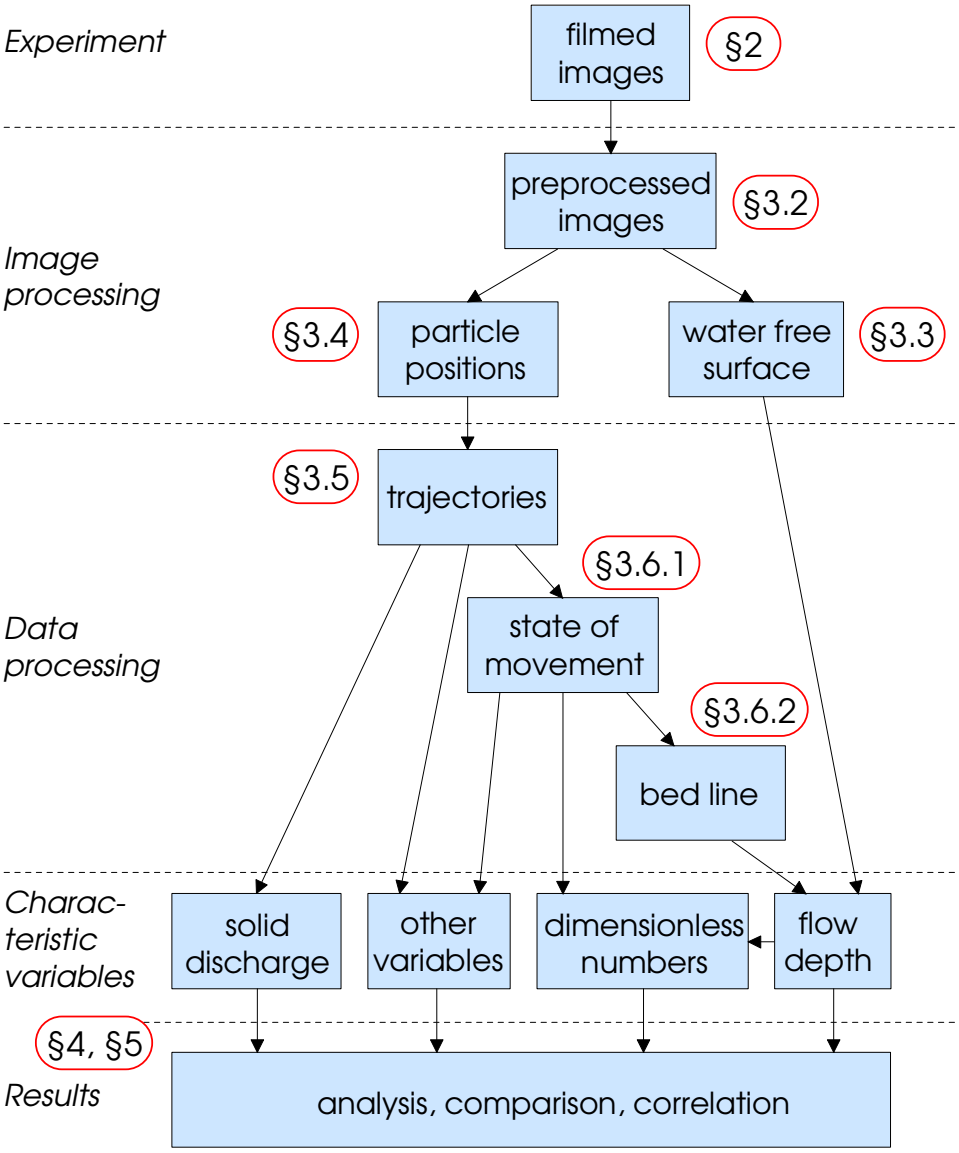

Fig. 3.2: Flowchart of image and data processing.

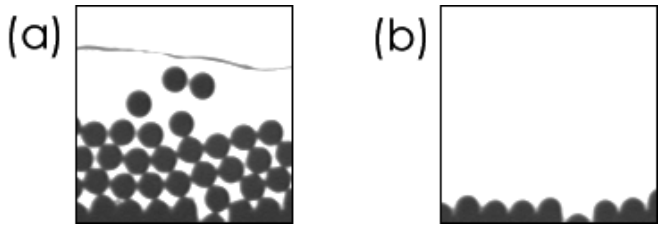

Fig. 3.3: Detection of the water line. Original images.

images keeping only the zone of the particles and water. We saved considerable calculation time by this preliminary step.

A convention in fluid mechanics leads to representing flow from left to right. However, due to the setup of our channel and the camera the flow we filmed ran from right to left. We therefore changed the flow direction of our filmed images subjecting them to an operation of inversion. The second preprocessing step was thus a simple operation of vertical symmetry.

3.3 Detection of the water free surface

The water free surface was fairly constant over the small width of the channel. In spite of the capillary attraction between water and the glass walls, the meniscus appeared on the filmed images as a thin line (Fig. 3.3(a)). We were thus able to take the mean value in the direction perpendicular to the channel walls to calculate the water line as a function of the x-coordinate and time, $w_f(x,t)$.

For its detection with the image-processing software Wima, we used two source images. We explain the procedure by considering a single image of the sequence reduced in length (Fig. 3.3(a)). Figure 3.3(b) shows an image of the empty channel we had taken before. The processing was done in nine steps illustrated in Fig. 3.4. These steps use classical image-processing operators as thresholding, dilation, and logical operators. The reader can refer to [GW92] and [Soi99] for further explanations. The following image-processing steps were performed:

(a) The image of the empty channel (Fig. 3.3(b)) was subtracted from the image of the flow (Fig. 3.3(a)), the channel base was thus eliminated.

(b) The image was inverted and the gray values were rescaled to the range 0–255.

(c) The number of gray values was reduced to black and white using a threshold condition. The threshold value was chosen as a function of the luminosity and contrast of the source images.

(d) The white zones were eroded (four iterations) so the water line would disappear.

(e) Conversely, the resting white spots were dilated. We effected six iterations to join the zones.

(f) The image was inverted.

(g) The logical AND-operation was applied on images (c) and (f). The particles were thus eliminated; the water line and small spots of noise remained.

(h) The line was slimmed down to the width of one pixel.

(i) The image was scanned from the top to find the first white pixel of each column to obtain $w_f(x)$. Figure 3.4(h) shows that there were some missing portions due to light reflections of the free surface. Consequently, we rejected the values breaching the condition $|w_f(x) - \overline{w_f(x)}| < w_e$, where $\overline{w_f(x)}$ is the x-averaged value and a maximal elongation of $w_e = 15$ pixels was chosen. The rejected values were recalculated making use of their neighboring zones. Inside the image, we applied linear interpolation. If there were missing portions at the left or right edge of the image, $w_f(x)$ was set to the value of the nearest available point (extrapolation with a constant value).

We combined these operations to a macro that processed all the images of the sequence consecutively. A calculation for a sequence of 8000 images took on the order of 30 minutes on an ordinary personal computer (Intel Pentium 4 CPU, 2.4 GHz, 1 GB RAM). We were thus able to calculate the water free surface w_f as a function of x and t. In Fig. 3.5, elevation has been coded in gray levels. The image represents the information of the full length of the observation zone, while only a short time period is shown here (2 instead of 60 s). The representation of $w_f(x,t)$ in the form of an image facilitated on the one hand the visual interpretation and enabled, on the other hand, a further analysis with image-processing softwares. Such an analysis is presented in App. B.

The uncertainty of the water line position was in most instances less than 1 pixel; however, we identified three sources of localized inaccuracies:

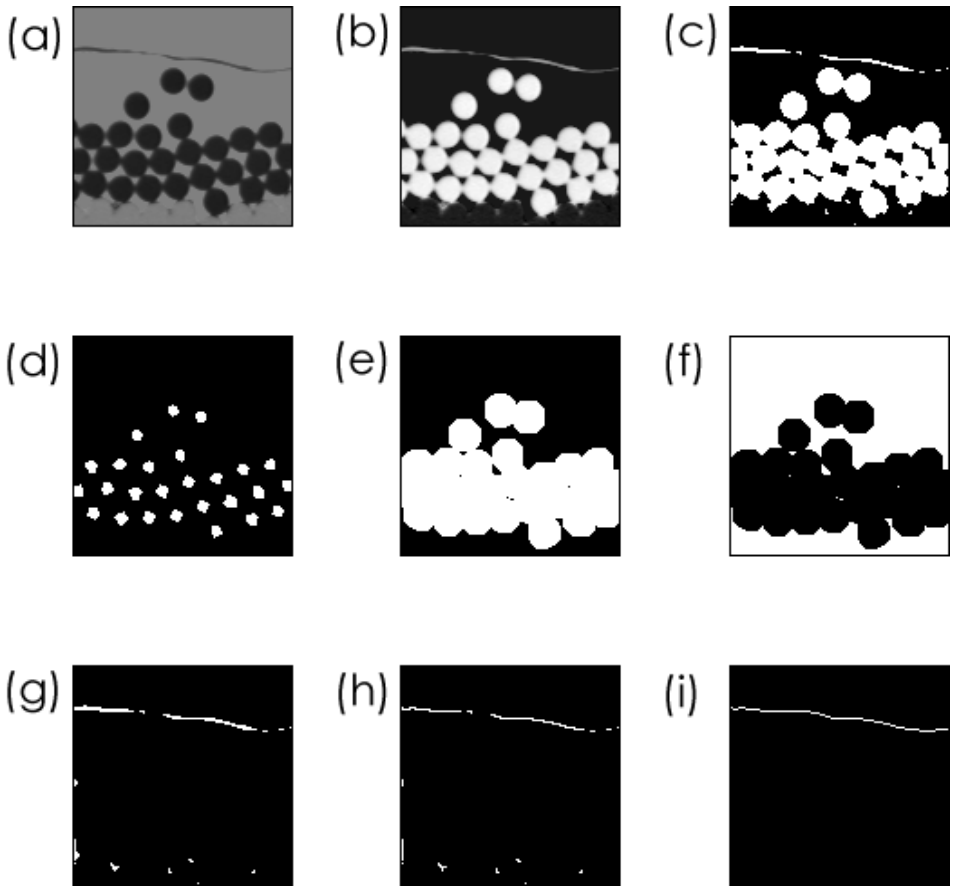

Fig. 3.4: Detection of the water line. Image-processing steps.

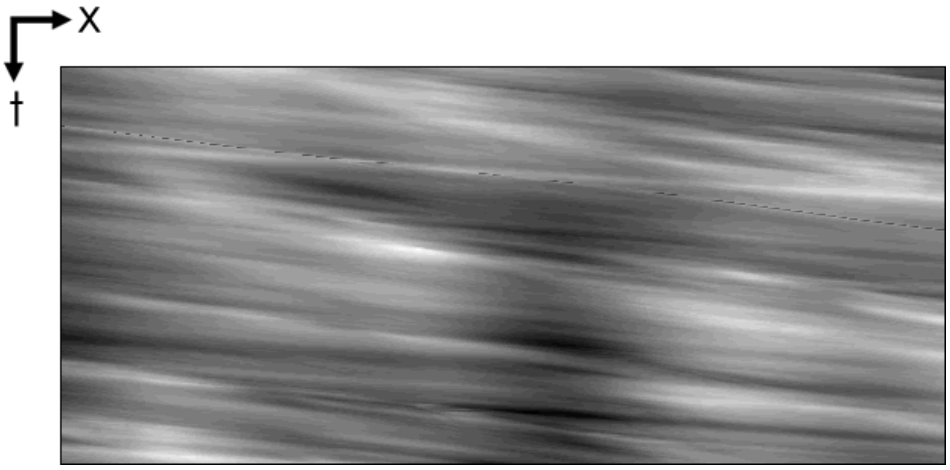

Fig. 3.5: Elevation of the water free surface $w_f(x,t)$ as a gray scale image. Image dimensions: $\Delta x = 220$ mm, $\Delta t = 2$ s. White: $w_f(x,t) = +5.7$ mm, black: $w_f(x,t) = -5.5$ mm versus the mean value. For experimental conditions, see Tab. 4.2, experiment D.

Light reflection of the free surface: We sought to optimize the illumination and the aperture of the camera to reduce reflection.

Air bubbles at the free surface: The water jet and the bead impact at the channel entrance were designed to entrain as little air as possible.

Beads touching the free surface: In this case, a part of the water line was eliminated with the bead and had to be interpolated. The occurrence depended essentially on the ratio of the water depth to the bead diameter (h/d) and thus of the flow conditions that we were investigating.

3.4 Detection of the particle positions

To detect the particle positions, we used the image of a model bead (Fig. 3.6(b)) in addition to the filmed image (Fig. 3.6(a)). A correlation between the model and the image was computed [GW92]. A ring-shaped model was chosen with negative values inside in order to have a zero mean value. A bead was detected whenever it coincided with the ring. The diameter of the ring was chosen to match the diameter of the beads in the filmed image. The

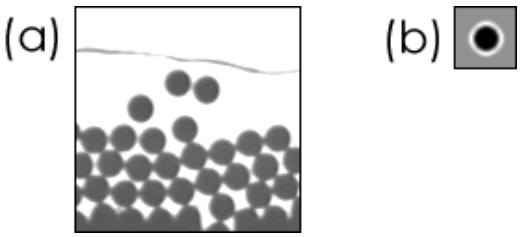

Fig. 3.6: Detection of the particle positions. Original images.

algorithm thus made use of the uniform size and shape of the particles. The processing was done in four steps illustrated in Fig. 3.7:

(a) An algorithm to search the pattern (Fig. 3.6(b)) in the image at hand was applied. We obtained an image showing the zones of high and low correlations in light and dark grays, respectively. Note that the correlation coefficient could not be calculated close to the image edges. Here the resulting image pixels were set to a medium gray level. The width of this zone was half the size of the model bead image (16 pixels). In the center of Fig. 3.7(a) a "correlation cloud" can be seen for each bead in the original image. Although these clouds intersected, circular shapes with pronounced maxima were obvious.

(b) The local maxima of the image were retained, i.e. all the pixels that were lighter than their four neighbors.

(c) The number of gray values was reduced to black and white using a threshold condition.

(d) The white pixels were dilated to increase the visibility of the bead centers, they appeared now as crosses.

(e) The (x, y)-positions of these crosses were extracted and saved in a list associated with the image (not shown in the figure).

These operations were joined in a macro that was applied on the images of the sequence consecutively, similarly to the detection of the water line. Due to the algorithm described in (a), this computation was longer, on the order of 2 hours.

In the center of the image, the uncertainty of the detected particle positions was less than 1 pixel (0.387 mm). Near the borders of the image, we

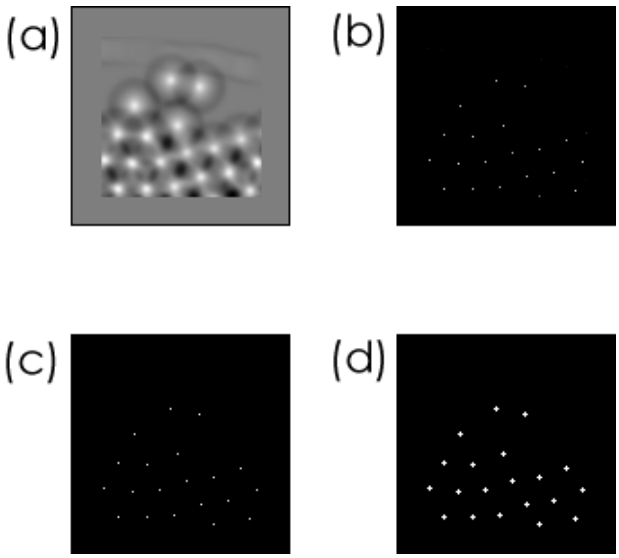

Fig. 3.7: Detection of the particle positions. Image-processing steps.

found deviations of about 2 pixels. Let us consider the lowest particle in Fig. 3.6(a), which was trapped in a gap of the channel base. In Fig. 3.7(d) the detected position is too high, too close to its neighbors. The center of its correlation cloud is out of the scope of the image (Fig. 3.7(a)), but a maxima was nevertheless identified. This deficiency of the algorithm had no further consequences:

At the left and right borders: We calculated particle positions and trajectories on the whole image (640 pixels in the x-direction), but restricted the terminal analysis to a smaller zone. Zones of 30 pixels were cut off from the left and the right leaving an effective image length of 580 pixels.

At the lower border: The particles near the lower image border, especially the trapped particles, were fairly immobile. As they did not contribute to the solid discharge the information on their exact positions was irrelevant. Indeed, the effect of immobile particles differed barely from the bumps of the channel base. We tried, however, to detect all the beads but not the bumps of the channel base (the bumps having the same diameter as the beads, the algorithm could confuse them with particles). This could be achieved by cutting off the lower

part of the image at the right position before the calculation. At the same time we reduced the upper part of the image to accelerate the image processing (see §3.2).

3.5 Particle tracking

3.5.1 Overview

The particle position data obtained from the detection algorithm were analyzed to obtain the particle trajectories. For this purpose, we developed a particle-tracking algorithm, which was integrated into the Wima software. Different from the detection algorithms, it was not a macro, but a subprogram coded in the C language.

The particle image velocimetry is perhaps the most popular recent technique in experimental fluid mechanics. A related method used especially for low particle concentrations is particle-tracking velocimetry [NKH89]. Its usual application is the determination of the velocity field of a fluid carrying small particles. In contrast, we focused on the individual particle motion in our study. The particle velocities differed from those of the surrounding fluid since our particles were coarse and had a higher density than water. Our algorithm was nevertheless comparable to an algorithm developed by Hwang [Hwa89].

The algorithm compared the bead positions of two consecutive images to determine the trajectory of each bead step by step. Although the use of spherical particles of uniform size made detection easier, it hampered the calculation of the trajectories since we were unable to distinguish between particles because of their shape. Given the high frame rate of the camera, the displacement of a particle between two images was always smaller than a particle diameter. This was essential not only to reach a high resolution of the trajectories, but primarily to be able to distinguish the particles over time. We explain the algorithm by describing first its initial step and then the iteration step, which was simply an advancement of the initial step.

3.5.2 Initial step

The initial time step of the particle-tracking algorithm is illustrated in Fig. 3.8. For each particle of the first image, we defined a circular searching zone (here shown only for particles A and B). The radius of this zone was the maximal displacement expected. A particle of the second image was associated with a particle of the first image if it was lying inside its search

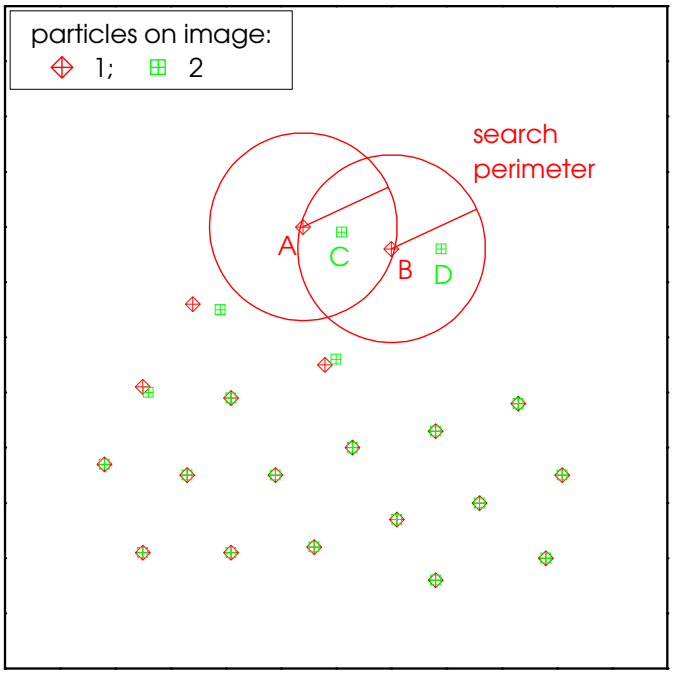

Fig. 3.8: Initial time step of the particle-tracking algorithm.

perimeter. Here, particle D was associated with B, whereas C was associated both with A and B. For each association, we noted the distance of the particles (see Tab. 3.1).

After the calculation of the complete association table for the image couple, the best associations were selected. For this purpose, the association with the minimal distance was chosen, eliminating other possible associations of the involved particles. In the case of several minimal distances, one of these associations was chosen arbitrarily. Next, the best remaining association was selected. In our example, the association A-C was chosen first; as a consequence, this eliminated the association B-C. In a second iteration, the association B-D was selected. Note that for some particles, no predecessor or successor could be found, especially for the particles entering or leaving the observation window.

In this way, the association table was transformed into a table of trajectories of the particles for the first two images. The information on particle displacements was used for the following calculation step.

particle on image 1	particle on image 2	distance (pixels)
A	C	7.07
B	C	9.49
B	D	9.00
...		

Tab. 3.1: Association table for the initial time step.

particle on image 2	particle on image 3	distance (pixels)
C	E	1.41
D	F	1.00
...		

Tab. 3.2: Association table for an iteration time step.

3.5.3 Iteration steps

A sketch of the particle-tracking algorithm for the following time-step is displayed in Fig. 3.9. It shows the particle positions for images 2 and 3. The difference compared to Fig. 3.8 is the position of the searching zones. An estimate for the particle position in image 3 was obtained by adding the displacement vector of the preceding calculation step to each particle position in image 2 (black arrows). The searching zone was centered around this estimate. Thus, the algorithm made use of the low acceleration of the particles.

Apart from the positions of the searching zones, the algorithm worked as described above. Here, the distance was calculated between the particle position of the third image and the estimated position (see Tab. 3.2). As the calculated distances were considerably lower for the second calculation step, a better correlation was achieved. In our example, particles E and F were associated only with particles C and D, respectively. The positions of particles E and F were appended to the trajectories, which then were denoted by A-C-E and B-D-F, respectively.

The following time steps were processed similarly. Whenever the information of the last displacement was available, it was used to calculate the estimate of the new particle position. If no predecessor of a particle could be found, a new trajectory was created. Otherwise, the particle coordinates

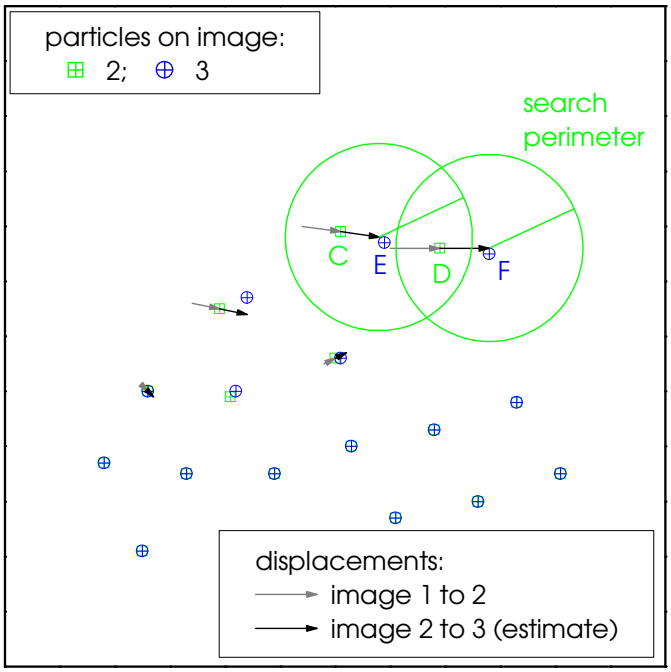

Fig. 3.9: Iteration time step of the particle-tracking algorithm.

were appended to an existing trajectory. If no successor position of a particle was found the trajectory was closed.

The only arbitrary parameter of the algorithm was the radius r of the searching zone, which was nothing but the maximal expected particle displacement. To avoid the association of resting particles with their neighbors, we limited it to the particle diameter on the images, $r = d/s \approx 16$ pixels, where s denotes the scaling factor of the camera. This limited the particle velocity being detected by the algorithm: $v_m = rsf \approx 0.80$ m/s, where v_m denotes the maximal velocity and f the frame rate of the camera. The limit affected only the first calculation steps of the trajectories whose particles were entering the observation window. The following steps were simple since the preceding displacements could be taken into account for tracking. Since the particle velocities in our experiments rarely exceeded 0.5 m/s, almost all the trajectories could be tracked from the start at the left edge of the image. As aforementioned, we calculated the trajectories on the whole images (640 pixels in the x-direction) but restricted the final analysis to a smaller zone. Zones of 30 pixels were cut off from the left and the right,

No.	start	size	x-positions (pixel)					y-positions (pixel)				
1	2	4	-	194	202	209	217	-	41	43	45	47
2	1	3	203	212	221	-	-	44	44	45	-	-
3	2	4	-	193	194	196	199	-	64	64	64	64
4	1	5	211	211	211	211	211	77	77	77	77	77
5	1	5	196	196	196	196	196	80	80	80	80	80
6	1	5	219	219	219	219	219	90	90	90	90	90
7	1	5	204	204	204	204	204	93	93	93	93	93
8	1	5	211	211	211	211	211	104	104	104	104	104

Tab. 3.3: Example for a table of trajectories. No., start, and size are the number of the trajectory, the first time step of its tracking, and the number of time steps the particle was tracked, respectively. The table was made for a reduced zone in x ($193 < x \leq 223$ pixel) and only for the first five time steps.

leaving an effective image length of 580 pixels.

We paid particular attention to avoiding the confusion of particles in the case of collisions. Therefore, we defined a second criterion for the association table in addition to the criterion of the minimal distance. The particles at low velocities (those that were susceptible to being hit and set in motion by others) were selected from the association table in a privileged manner. The application of the algorithm showed, however, that this second criterion was rarely relevant, which is why we only mention it here.

3.5.4 Trajectories

Running the algorithm on the whole image sequence, we obtained a table with the trajectories of all the particles observed. This table contained 400 to 2000 trajectories, depending on the solid discharge adjusted at the channel entrance. Table 3.3 shows a considerably shortened example of a trajectory table. The lists of x- and y-positions do not represent regular arrays since the trajectories had different sizes (the size of a trajectory being the number of time steps it was tracked). We thus had to note the time step of the start and the size of each trajectory in the table.

In the example, the particles involved in trajectories No. 4 to 8 did not move at all during the five time steps. Particles 1 and 3 entered the observation zone, whereas particle 2 left it.

It is more convenient to study the particle trajectories by means of a diagram. Figure 3.10 shows the trajectories of the first five time steps of

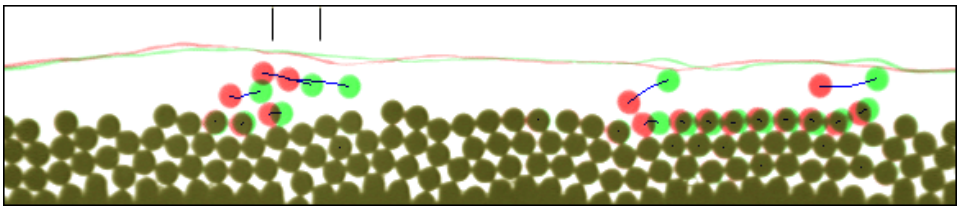

Fig. 3.10: Visualization of the particle trajectories (blue). In the background, the particles at the initial (red) and the final positions (green) of the short image sequence are shown.

an image sequence. The first and the fifth filmed images can be seen in the background (the particles are shown in red and green, respectively). The zone in the x-direction of Tab. 3.3 is marked in the upper part of the figure for a comparison.

While developing the particle-tracking algorithm, we tested its accuracy continuously. We used reduced image sequences to compare the calculated trajectories with the filmed images. The algorithm yielded correct results even when particles collided. The amount of data extracted from our experiments was still too large to make more than random sample tests of the reliability of the trajectories. Additionally, we carefully studied the global results obtained from the analysis of the trajectories (see the following chapters), no significant errors of the particle-tracking algorithm were revealed. We especially compared the solid discharge deduced from the trajectories $\dot{n}$ with the injection rate $\dot{n}_0$. This measured solid discharge fluctuated greatly (see §4). However, taking the average over sufficiently long time periods (one minute), the relative difference $(\bar{\dot{n}} - \dot{n}_0)/\dot{n}_0$ was smaller than $\pm$ 3% (see Tab. 4.2). We can thus conclude that the algorithm performed accurately for the given problem.

3.6 State of movement and bed line

3.6.1 Definition of the state of movement

Next the state of movement of a particle was defined by considering that each bead was always either in a resting, rolling, or saltating regime (see Fig. 3.11). This partitioning posed several difficulties from the algorithmic viewpoint. The three states of movement were distinguished as follows:

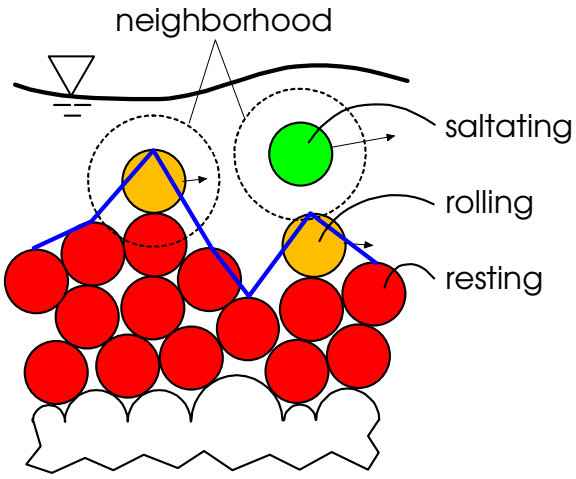

Fig. 3.11: Sketch defining the state of movement and the bed line.

The resting beads formed the bed, they were in sustained contact with their neighbors. They were not expected to move or, more precisely, their possible drift velocities (together with fluctuating velocities) were lower than a threshold velocity u_t: $|\mathbf{u_p}| < u_t$, where $\mathbf{u_p}$ denotes the particle velocity averaged over five consecutive frames.

The beads in the rolling regime were located above the beads at rest: They remained in close contact with the bed and moved at a certain velocity. Our algorithm used two criteria to distinguish rolling beads: $|\mathbf{u_p}| \geq u_t$ (bead in motion) and $d_n/d \leq \varepsilon$ (particles in the vicinity), where d_n is the distance to the next neighbor (measured between the mass centers and averaged over five consecutive frames) and ε is a threshold.

The beads in saltation leaped above the others. They had no close neighbors except when they collided with other beads. The algorithm distinguished saltating beads using the criteria $|\mathbf{u_p}| \geq u_t$ and $d_n/d > \varepsilon$.

The values of the threshold parameters u_t and ε were adjusted by trial and error to minimize the differences between the state determined by the algorithm and the state determined by the naked eye. Good agreement was obtained for $u_t = 0.025$ m/s and $\varepsilon = 1.07$.

The state of movement of each particle was a function of time. A particle at rest could be set in rolling motion by the fluid or other particles and

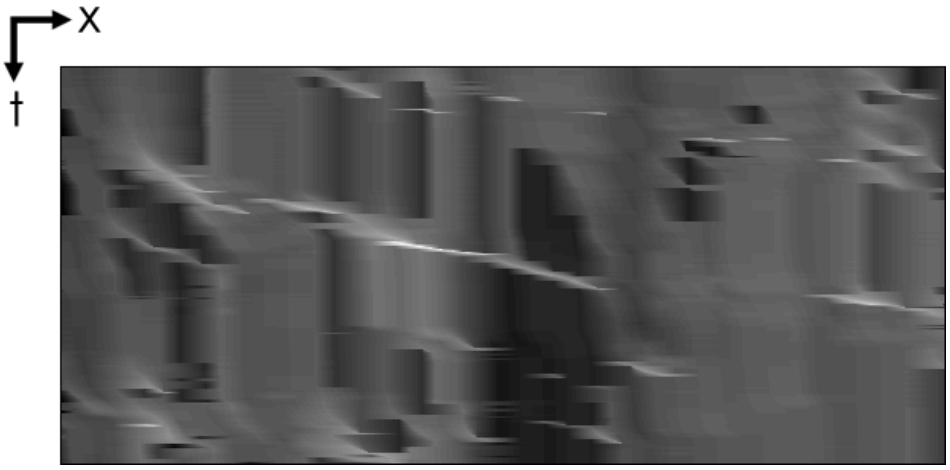

Fig. 3.12: Elevation of the bed surface $b_s(x,t)$ as a gray scale image. Image dimensions: $\Delta x = 220$ mm, $\Delta t = 2$ s. White: $b_s(x,t) = +15.5$ mm, black: $b_s(x,t) = -7.3$ mm versus the mean value. For experimental conditions, see Tab. 4.2, experiment D.

accelerated to get into saltating motion. On the other hand, a fast moving particle could lose its kinetic energy and come to rest.

Since the state of movement was determined by using a time average, it was not defined on some occasions. This occurred (i) at the beginning and the end of the image sequence and (ii) for particles entering or leaving the observation window. The undefined state of movement had no further consequence since (i) the image sequences were long (8000 frames) compared to the time step used for averaging (5 frames) and (ii) the zones of the left and right borders of the images were discarded from the following analysis.

3.6.2 Definition of the bed line

To describe the fact that the bed was continuously evolving through particle deposition and erosion we defined the bed surface elevation $b_s(x,t)$. Arbitrarily, we considered that the bed surface profile is the broken line linking the top points of the uppermost resting or rolling beads. Figure 3.11 depicts this broken line at a given time. Viewed as a function of time, the bed elevation could be visualized (see Fig. 3.12) similarly to the water free surface (see Fig. 3.5). The two diagrams turned out to be very different (see App. B for an interpretation).

The water depth $h(x,t)$ was defined as the difference between the water and the bed elevations, $h(x,t) = w_f(x,t) - b_s(x,t)$. For the experiments with a fixed bed (A and B see §4) the bed elevation was constant. For the experiments run in absence of particles (see §2.5.2) the bed elevation depended only on x.

3.7 Conclusion

This chapter describes the algorithms developed to analyze our experimental data. Starting from the filmed images, the particle trajectories and the water line were calculated through several processing steps. An automatic processing was essential to be able to treat large amounts of data (see §5).

An important information that could not be extracted from the filmed images was the velocity field of the water. This was mainly hampered by the fact that, different from the particle movement, the water flow was three-dimensional. On the one hand, methods such as stereo particle image velocimetry are rather complex in their application. Since in our case the turbulent structures were typically smaller than the particle diameter it would be difficult to follow them over the whole actual observation length (25 cm). On the other hand, the techniques to mesure velocity fields yield only reliable results if an averaging over several measurements can be done, the presence of particles would indeed hamper the averaging. The velocity profile of the water channel flow without particles was measured in a previous study [FR01], the integration of particles raises many difficulties.

We were able to calculate a mean velocity of the water flow since the mean discharge and the water depth were known. The most important information obtained from the experiments was, however, the particle trajectories. They made it possible to calculate physical variables characterizing the flow as the solid discharge with a high time resolution (see §4). We will furthermore see that the knowledge of the movement of each particle can be used to observe erosion and deposition phenomena which are essential for bed load transport. Such an experimental analysis of bed load transport incorporating the movement of a complete set of particles has to our knowledge never been done before.

Chapter 4

Fluctuations of the solid discharge[1]

Abstract: We studied the origins of the fluctuations of the measured solid discharge by investigating different flow conditions. Two experiments were carried out with a fixed (smooth or corrugated) channel bottom and two others were run with a mobile bed (involving layers of closely packed particles lying along the channel base, which could be entrained by the stream); in the latter case, two particle arrangements were tested. It was found that, to a large extent, fluctuations reflected the finite size of the observation window. For fixed beds, the characteristic timescale of fluctuations and their probability distribution was predetermined by evaluating the mean and fluctuating velocities of a single particle. Solid discharge fluctuations were exacerbated when the bed was mobile because (i) the moving solid phase and the stationary bed exchanged particles and (ii) collective entrainment of particles occurred.

4.1 Introduction

The objective of this chapter is to examine the origins of solid discharge fluctuations observed with the experimental setup described above. Compared to previous studies of Ancey, Bigillon *et al.* [Big01, ABF$^+$02, ABFD03] the main difference of the experiments presented here is the use of a continuous particle supply. Surprisingly enough, we observed substantial variations in

[1]Based on T. Böhm, C. Ancey, P. Frey, J.L. Reboud, and C. Ducottet, *Physical Review E* **69** 061307 (2004); see [BAF$^+$04].

the solid discharge with time, whereas the flow conditions were stationary on average: Intermittent phases of transport and fluctuations as large as the mean solid discharge occurred. Such phenomena are frequent when fine particles are involved because their motion is controlled by fluid turbulence, but they were not expected here given the large size of particles used in our experiments. In order to gain insight into the origins of these fluctuations, we conducted further tests by varying the boundary conditions at the channel bottom: We used fixed channel bases (smooth or corrugated bottom) and mobile beds (the moving solid phase could exchange particles with the bed). Specific care was taken to distinguish between different artificial fluctuations and intrinsic fluctuations.

This chapter attempts to understand why solid discharge exhibits large fluctuations in steady conditions. We shall see that the most plausible explanation lies in the collective motion of the particles entrained from the bed and that this collective motion is directly related to the particle arrangement inside the bed. We present the experimental results for four different channel configurations. For all these configurations, the solid supply at the channel inlet and the slope were kept constant. We modified however the boundary conditions at the channel bottom by constraining particles to flow either over a fixed bed or an erodible bed.

After presenting the conditions of the four different experiments, we describe the characteristics of the flows introducing several dimensionless numbers. The presentation of the results for each of the experiments is preceded by a general overview of the results and followed by a conclusion.

4.2 Experimental conditions

The four experiments presented in this chapter were run under bed load equilibrium conditions with the same channel slope ($\tan\theta = 10\%$) and the same particle injection rate of $\dot{n}_0 = 8$ beads per second. They differed in the applied boundary conditions which is made clear in Tab. 4.1 and in Fig. 4.1. The terms fixed bed, mobile bed, and obstacle are defined in §2.5, the characteristics of the channel bases we were using are detailed in §2.2.

For experiments A and B a water discharge $q_w = 5.39 \times 10^{-3}$ m^2/s could be chosen independently of the solid discharge. It was set to 3.85×10^{-3} m^2/s for bottom C versus 5.39×10^{-3} m^2/s for bottom D: Bed equilibrium was reached for significantly different water discharges (relative difference of 40%). This provided preliminary evidence of the substantial effect of particle arrangement on particle transport.

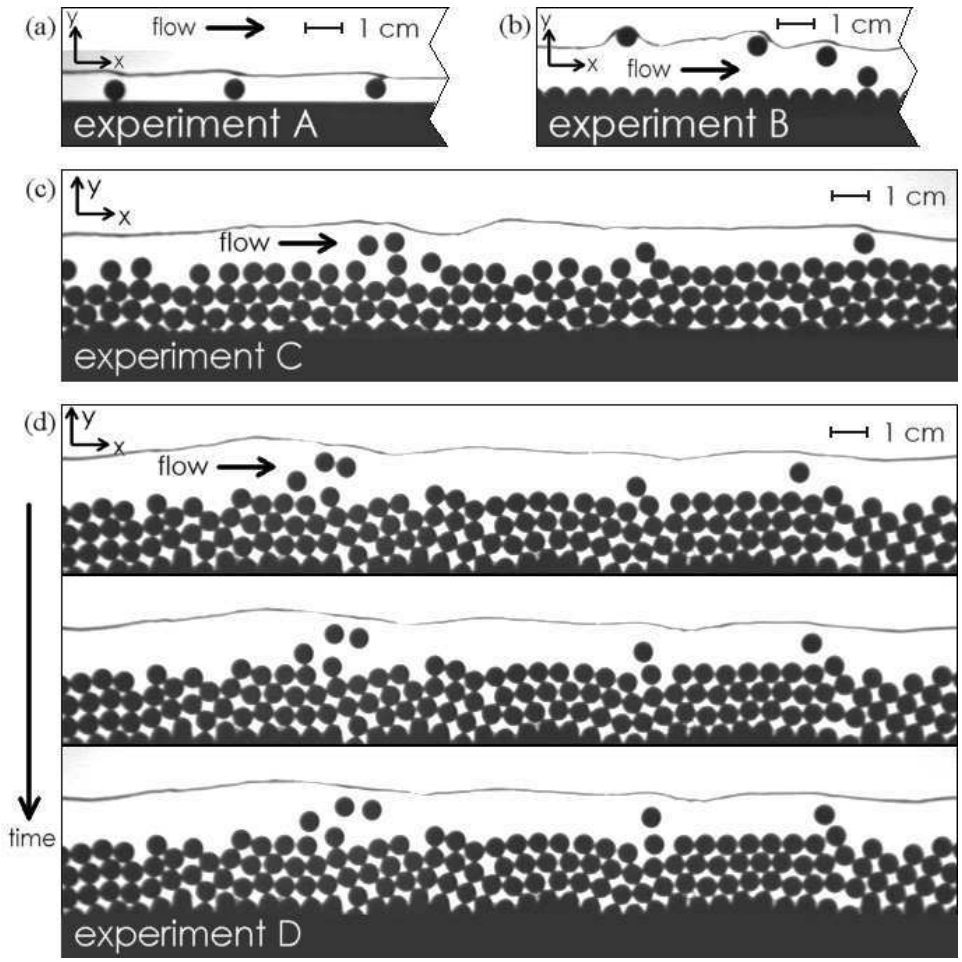

Fig. 4.1: Images of the particle transport for experiments A, B, C, and D. Image dimensions: 25 cm × 5 cm (resolution: 640 × 120 pixels), (a) and (b) reduced; exposure time: 0.2 ms; frame rate: $f = 129.2$ Hz, channel inclination: $\tan\theta = 10\%$. For experimental conditions, see Table 4.2.

Experiment	bed	obstacle	channel base
A	fixed	no	flat and smooth
B	fixed	no	corrugated
C	mobile	yes	half-cylinders of various sizes
D	mobile	yes	half-cylinders on different levels

Tab. 4.1: Conditions of experiments A–D.

4.3 Dimensionless numbers

The hydraulic conditions can be specified using classic dimensionless numbers. Table 4.2 reports the time-averaged values of these numbers. In the table, σ_h and $\sigma_{\dot{n}}$ denote the standard deviations of the water depth and the solid discharge, respectively. Here, to make the flow rate $\dot{n}$ more palpable, we express it in beads/s instead of m^3/s.

The flow Reynolds number is defined as $\mathrm{Re} = 4R_h\bar{u}_f/\nu$, where $R_h = Wh/(2h+W)$ denotes hydraulic radius, $\bar{u}_f = q_w/h$ fluid velocity (averaged in the y- and z-directions), ν kinematic viscosity of water, and h water depth.

The Froude number $\mathrm{Fr} = u_f/\sqrt{gh}$ (where g denotes gravity acceleration) varied significantly over the experiment duration and along the main stream direction. The Froude number was calculated for each x-position and each instant t, in Tab. 4.2 we give the averaged values. The variation scale of the Froude number Δ_{Fr} was estimated assuming a constant water discharge and considering the variations in water depth: $\Delta_{\mathrm{Fr}} = |\delta\mathrm{Fr}| = |3\,\mathrm{Fr}\,\sigma_h/(2\,h)|$. These numbers show that there were frequent transitions from subcritical to supercritical regimes for experiments C and D. This phenomenon seems intrinsic to bed load transport on a mobile bed (e.g. see [Gra97]).

The Shields number is defined as the ratio of the bottom shear stress ($\tau_0 = \rho_f g h \tan\theta$) to the stress equivalent of the buoyant force of a particle lying on the bottom [Jul94]: $N_{Sh} = \tau_0/(gd(\rho_p - \rho_f))$. The critical Shields number corresponding to incipient motion, $N_{Sh,c}$, has been determined experimentally by Ancey *et al.* [ABF$^+$02] for the motion of a single glass bead, yielding values in the range 0.001–0.005. This is consistent with experiment B of the present study which was conducted far above the threshold of motion ($N_{Sh} = 0.114$). For our experiments with mobile bed however (C and D), a critical shear stress of $0.001 < N_{Sh,c} < 0.005$ seems too low. In preliminary experiments, we determined the water discharge necessary to set a stationary particle bed into motion (without solid supply). This critical water discharge was on the order of 20% of the typical value for bed load equilibrium. This indicates that experiments C and D ($N_{Sh} \approx 0.1$) were run rather close to incipient motion. A critical Shields number in the range 0.047–0.06 as found for gravel-bedded rivers by many authors (see [BM97] for a review of incipient motion studies) is thus of the correct order of magnitude. At this point our experiments where in line with classical sediment transport experiments, even though we used spherical particles.

The particle Reynolds number can be defined as $\mathrm{Re}_p = |\bar{u}_f - \bar{u}_p|d/\nu$, where $\bar{u}_p$ denotes the mean velocity of a particle in motion. Furthermore,

Experiment		A	B	C	D
h (mm)		7.0	10.2	8.7	12.0
σ_h(mm)		0.7	1.5	1.9	2.2
q_w (10^{-3} m^2/s)	$= Q_w/W$	5.39	5.39	3.85	5.39
u_f (m/s)	$= q_w/h$	0.77	0.53	0.44	0.45
$\dot{n}$ (beads/s)	$= \frac{1}{L}\sum_{i=1}^{N} u_i$	7.99	8.20	7.97	7.93
$\sigma_{\dot{n}}$ (beads/s)		2.35	2.98	4.31	3.50
Re	$= 4R_h\bar{u}_f/\nu$	6810	5200	4190	4590
Fr	$= u_f/\sqrt{gh}$	2.98	1.73	1.68	1.40
Δ_{Fr}	$= \lvert 3\,\mathrm{Fr}\,\sigma_h/(2\,h)\rvert$	0.464	0.377	0.544	0.385
N_{Sh}	$= \tau_0/(gd(\rho_p - \rho_f))$	0.078	0.114	0.096	0.133
Re_p	$= \lvert\bar{u}_f - \bar{u}_p\rvert d/\nu$	669	545	859	897
D	$= d\sqrt[3]{(\rho_p/\rho_f - 1)g/\nu^2}$	147	147	147	147
C_s(%)	$= q_s/q_w$	2.58	2.65	3.60	2.56
h/d		1.17	1.70	1.45	2.00

Tab. 4.2: Flow characteristics and time-averaged values of dimensionless numbers characterizing bed load and water flow of experiments A–D. Constant parameters: Channel inclination $\tan\theta = 10\%$, particle injection rate $\dot{n}_0 = 8$ beads/s, and channel width $W = 6.5$ mm.

we introduced the dimensionless particle diameter $D = d\sqrt[3]{(\rho_p/\rho_f - 1)g/\nu^2}$ used in sedimentology to characterize the particle size compared to the turbulence scale [Jul94]. The solid concentration is defined as the ratio of the solid and the water discharge $C_s = q_s/q_w$. Values reported in Table 4.2 are low, which indicates that the biphasic flow was dilute. Compared with values found in sedimentology literature the concentration was high due to the steep channel slope. The ratio h/d was low, typically in the range 1–2.

Note that the dimensionless number values differ substantially from the values usually found in the sedimentology literature. The reason is twofold: First we used a short and narrow channel, which led to studying low Reynolds number regimes, whereas hydraulicians take care to avoid such regimes. Since we used coarse particles, particle motion was weakly dependent on the actual value of the flow Reynolds number and turbulence structure. Therefore we think that the small size of the experimental setup is not a handicap. Second we investigated supercritical flows because flow must be energetic enough to carry particles. However, in a supercritical regime, flow depth was low: on the order of the particle size, meaning that particle motion was affected by the water free surface.

4.4 Experimental results

Since the primary objective was to understand the origins of the solid-discharge fluctuations, we paid particular attention to distinguishing between fluctuations intrinsic to the phenomenon and those coming from the measurement system (finite size of the observation of the window, acquisition rate, etc.). The solid discharge Q_s is usually defined as the flux of particles through a flow cross-section $\mathcal{S}$: $Q_s = \int_{\mathcal{S}} d\mathcal{S}\mathbf{u}_p \cdot \mathbf{k}$, where $\mathbf{k}$ is the unit normal to $\mathcal{S}$. This definition, suitable to continuum fields, is not well-suited to discrete elements. A more convenient definition is to introduce the flow rate in terms of the probability $P[\mathbf{u}_p|\mathbf{x}, t]$ that a particle crosses the control surface $\mathcal{S}$ at position $\mathbf{x}$ and time t with velocity $\mathbf{u}_p$:

$$Q_s = \int_{\mathcal{S}} \int_{\mathbb{R}^2} |d\mathbf{x}| d\mathbf{u}_p P[\mathbf{u}_p|\mathbf{x}, t]\mathbf{u}_p \cdot \mathbf{k}. \tag{4.1}$$

Under steady conditions ($\partial P/\partial t = 0$), this definition can be worked out as:

$$Q_s = \lim_{V\to\infty} \frac{1}{V} \sum_{i=1}^{N} u_i v\mathcal{S} = \lim_{L\to\infty} \frac{v}{L} \sum_{i=1}^{N} u_i, \tag{4.2}$$

in which the ensemble average has been replaced by a volume average. The integration has been made on a control volume $\mathcal{V} = \mathcal{S} \times L$ of length L and volume V. We have also used: $v = 4\pi a^3/3$ the particle volume, $u_i = \mathbf{u}_p \cdot \mathbf{k}$ the streamwise velocity component of particle i, and N the number of particles in motion in the control volume. Therefore, in the following, we shall define the flow rate $\dot{n} = Q_s/v$ as:

$$\dot{n} = \frac{1}{L} \sum_{i=1}^{N} u_i. \tag{4.3}$$

An ideal experimental setup would be based on (i) an observation window with a length L that outweighs the mean distance λ between two moving particles and (ii) an acquisition rate much larger than the inverse of the typical particle timescale, computed as the time needed for the particle to move across the window.

In our laboratory experiments, the typical acquisition rate f, particle velocity u_p, and window length L were approximately 130 Hz, 0.3 m/s, and 25 cm, respectively. The supply rate of particles being $\dot{n}_0 = 8$ beads/s, we deduce that the interparticle length scale is on the order of $\lambda = u_p/8 \approx$ 38 mm and the mean time for a particle to move across the window is on the order of $t_c = L/u_p = 0.8$ s. These estimates lead to the ratio:

$L/\lambda \approx 7$ and $f/(1/t_c) = 104$, which means that condition (ii) above is met whereas condition (i) is not. Resulting from the finite size of the observation window and the channel, artificial fluctuations were generated in the time records of solid discharge. Another source of fluctuations comes from the solid supply system. The bead supply system was designed to ensure a constant injection rate. However, we observed slight variations in the bead position and velocity at the moment of the release from the transport wheel. The beads thus impacted on different points of the channel, which led to nonuniform distances between two consecutive beads. For the experiments with a fixed bed (A and B), this deficiency was reflected by a strong variation in the number of beads in the window. In contrast, for the mobile bed experiments, we expected that the influence of the supply system on the flow in the observation window was weak because of the buffer effect of the bed: Since the observation window was located 1.2 m from the channel inlet, an injected bead was likely to experience several jumps and/or transitions to rest before reaching the observation window; it is thus unlikely that this bead kept memory of its initial conditions.

The time records of the solid discharge were analyzed by taking a closer look at its empirical probability distribution and its correlation function. In addition, we carefully examined the features of the particle trajectories such as the types of motion as well as the leap length and height of saltating particles. To synthesize this information, we reported the particle movements in a space-time diagram. We further studied the structure of the bed arrangement. The main results are reported in Fig. 4.2 (flow-rate variation with time), Fig. 4.3 (autocorrelation of $\dot{n}$), and in Fig. 4.4 (probability distribution of $\dot{n}$); they are analyzed in the following sections.

4.4.1 Smooth bottom (experiment A)

Comparison to a theoretical approach

The simplest configuration is a water stream over a flat surface. In this case, it is expected that particles roll or slide quickly as a result of the driving force exerted by gravity and water drag. Assuming that a test particle reaches a steady regime, we can express the momentum equation as a balance between the streamwise component of gravity acceleration $m'g\sin\theta$ and the mean water drag force $C_D\rho_f\pi a^2|u_p - u_f|^2/2$. We used the following notations: $m' = 4\pi a^3(\rho_p - \rho_f)/3$ is the buoyant particle mass and C_D the drag coefficient; typically for high particle Reynolds numbers and confined flows, the drag coefficient is close to unity [ABF$^+$02]. The mean particle

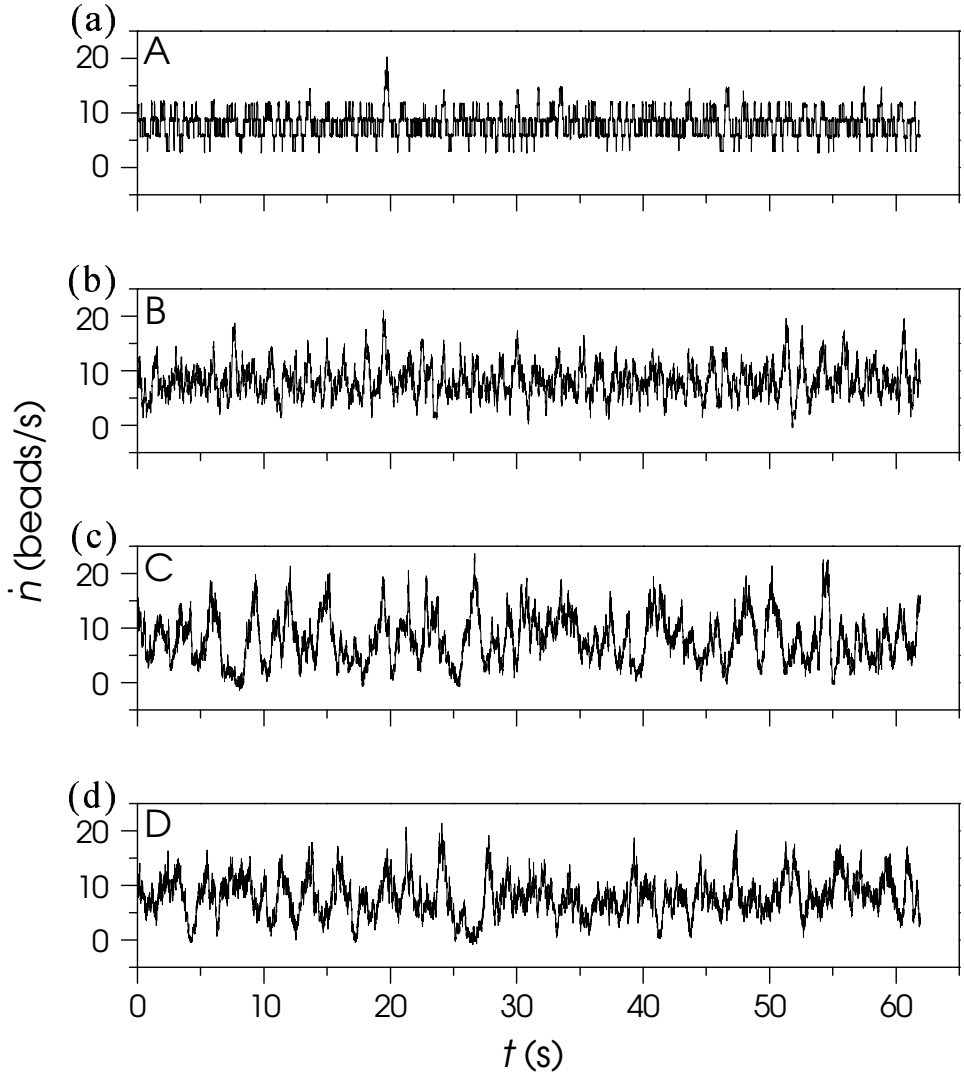

Fig. 4.2: Variation in the measured solid discharge with time for experiments A–D.

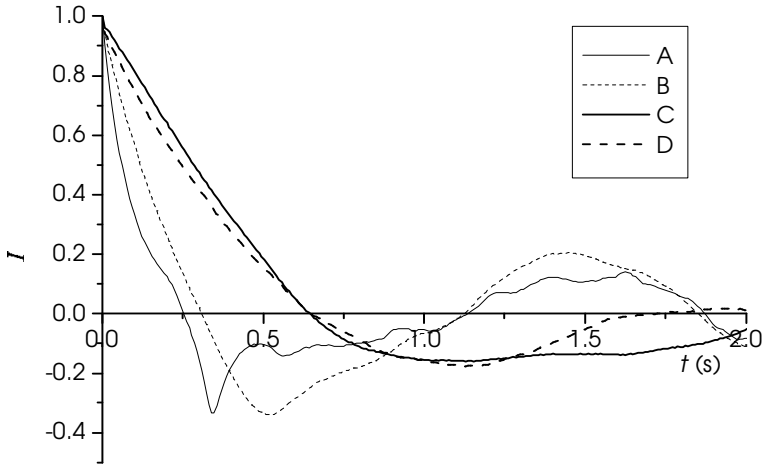

Fig. 4.3: Autocorrelation functions for experiments A–D.

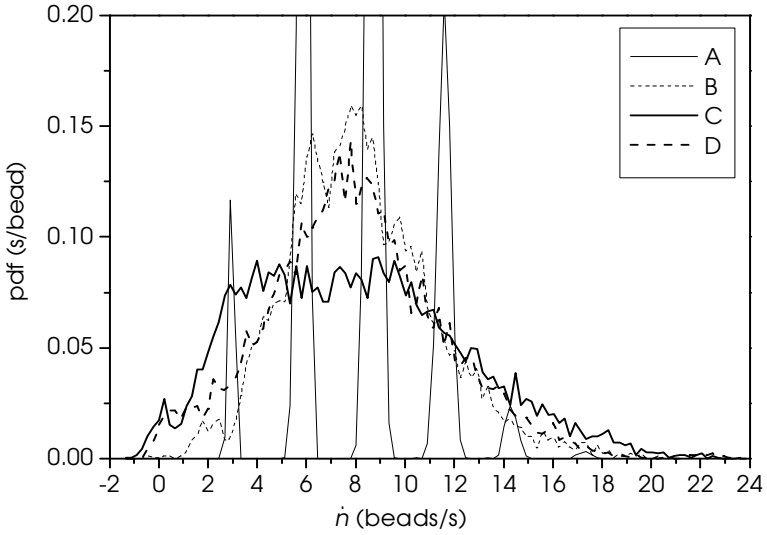

Fig. 4.4: Empirical probability density functions for experiments A–D.

velocity is then:

$$\bar{u}_p = \bar{u}_f - \sqrt{\frac{8}{3}\frac{\rho_p - \rho_f}{\rho_f}\frac{\sin\theta}{C_D}ag}. \tag{4.4}$$

As shown in Table 4.2, the mean fluid velocity was 0.77 m/s and particle velocity should have been close to 0.61 m/s. The interparticle distance was then: $\lambda = \frac{1}{8}\,0.61 \approx 7.7$ cm and thus, in the observation window (580 pixels or equivalently $L = 22.5$ cm), we must count 2.94 particles on average or, to be more specific, 6% of the recorded frames should include two particles and 94% should contain three particles. As a result, the solid discharge should oscillate with two possible states: $\dot{n} = 5.45$ beads/s and $\dot{n} = 8.17$ beads/s.

Time variations in $\dot{n}$ are plotted in Fig. 4.2(a). The autocorrelation of the signal are reported in Fig. 4.3. The time variations in solid discharge were step-shaped, which means that the solid discharge function was valued over a finite set of possible values and thus $\dot{n}$ behaved as a discrete random variable. This is probably best seen in the probability density function (pdf) plot: Figure 4.5 shows the scaled histogram of the recorded values and the expected probability distribution deduced using heuristic arguments. As expected, two peaks are found in the $\dot{n}$ pdf, but marginal spikes are also present. As shown in the inset of Fig. 4.5, although there is not much difference between the measured and expected average number of particles contained in the observation window (2.66 against 2.94), the probability density function of the particle number was much wider than expected: On rare occasions, up to seven particles could be observed in the window. This difference between the expected and observed values mainly resulted from small irregularities in bead supply at the channel inlet.

Another striking result is that there was not much difference between the probability distributions of N and $\dot{n}$ in terms of their shape, demonstrating that the particle velocity was fairly constant and close to the mean value. Experimentally, we found that the mean value of $\bar{u}_p$ was 0.65 m/s, while our heuristical approach gives an estimate of 0.61 m/s, in fairly good agreement with the observed value.

Time correlation

Figure 4.6 reports the intercorrelation function of the solid discharge. It was obtained by dividing the observation window vertically into two halves and calculating the time evolution of the solid discharge for either half (see eq. (4.3)). The intercorrelation function was computed by taking normalized signals $(\dot{n}(t) - \overline{\dot{n}})/\sigma_{\dot{n}}$.

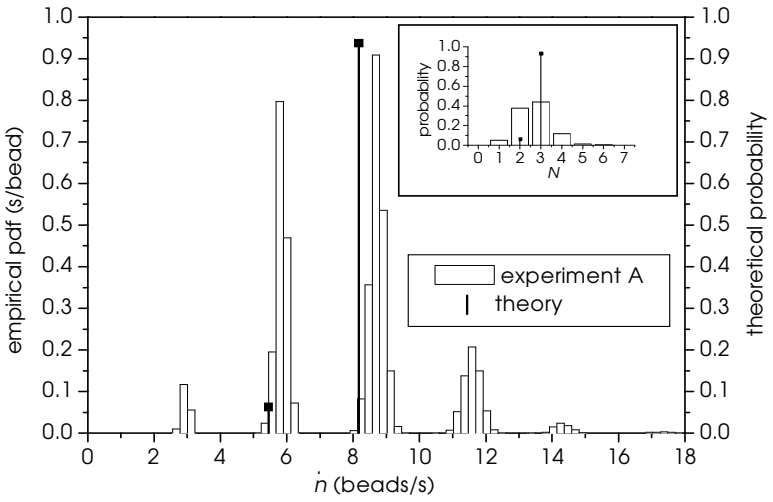

Fig. 4.5: Probability density function (pdf) of the solid discharge $\dot{n}$. The white histogram gives the empirical pdf of the observed values while the bold lines (here two peaks) stand for the theoretical mass distribution of $\dot{n}$. In the panel, the probability distribution of the number N of particles counted in the observation window is reported.

For experiment A, this yields a spike function with a maximum at the characteristic time of $t_A = 0.17$ s. This time is consistent with the travel time of a particle: Since the average velocity was 0.65 m/s, the time required for a particle to cross half the window was $t = 0.174$ s. The high value reached by the maximum shows that the signal changed only slightly between the two window halves because the interparticle distances once established at the channel inlet did not change along the channel. The channel base did not introduce any significant perturbation to the particle movement.

In short, we have found that, for smooth beds, the observed fluctuations in solid discharge essentially came from the finite size of the observation window compared to the particle diameter. In such experiments, solid discharge fluctuations induced by water turbulence were low.

For smooth beds, the solid discharge fluctuations essentially came from the finite size of the observation window compared to the particle diameter.

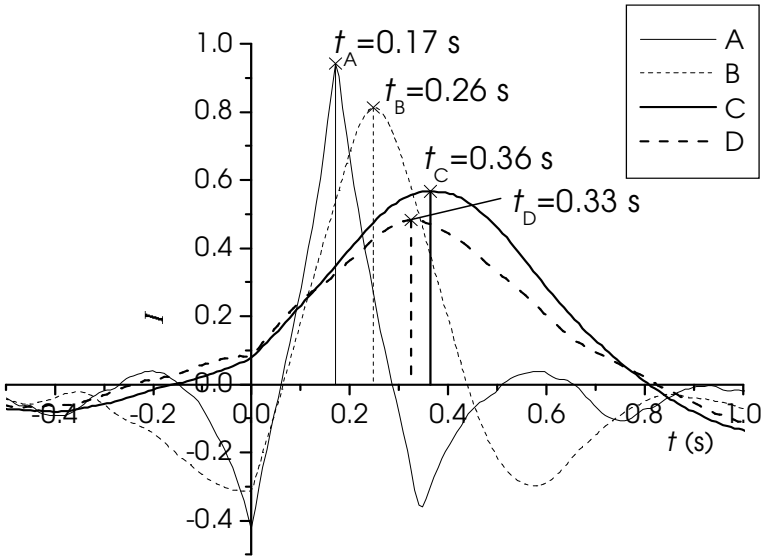

Fig. 4.6: Normalized intercorrelation functions of the solid discharge $\dot{n}$ computed over either half window for experiments A–D.

4.4.2 Corrugated bottom (experiment B)

Comparison to a theoretical approach

In order to test the influence of the bottom roughness, we conducted a further experiment replacing the smooth base by a corrugated surface. A wider range of the particle velocity was expected as a result of collisions with the corrugated bottom. This should generate larger fluctuations in the solid discharge than in the previous case. To compute the probability density function of the flow rate, we used the following assumptions: (a) the number of particles included in the observation window is distributed according to a Poisson distribution, (b) the streamwise components of particle velocity is Maxwellian, (c) the particle velocity distribution is independent of the particle number (because flow is dilute). Under these assumptions, it can be shown (see App. A) that:

$$P_{\dot{n}}(\dot{n}|L) = \sum_{k=1}^{\infty} \frac{e^{-\mu}\mu^k}{k!\sqrt{2\pi k}} \frac{L}{\sigma_u} \exp\left[-\frac{(L\dot{n} - k\bar{u})^2}{2k\sigma_u^2}\right], \tag{4.5}$$

where σ_u^2 is the particle velocity variance (streamwise component), $\bar{u}$ its average, and μ is the average number of particles moving in the observation

window. No closed analytical expression was found, but numerical estimations can easily be made because of the rapid convergence of the sum and the moments of $P_{\dot{n}}$ can be analytically determined (see App. A). Notably it is shown that the average flow rate is $\mu\bar{u}/L$, as expected, and its variance is $\mu\sigma_u^2/L^2$. As previously, the mean number of particles contained in the observation window can be estimated from the mean interparticle distance λ imposed by the particle supply frequency ω_0 (here $\omega_0 = 8$ Hz) and particle velocity: $\mu = L/\lambda$ with $\lambda = \omega_0^{-1}\bar{u}_p$. Therefore, we find that the mean flow rate equals the supplied flow rate $\dot{n}_0$ and its variance is:

$$\mathrm{Var}[P_{\dot{n}}] = \frac{1}{L}\frac{\sigma_u^2}{\bar{u}_p}. \tag{4.6}$$

From a theoretical viewpoint, solid discharge fluctuations result from the finite-size of the channel (factor L^{-1}) and velocity fluctuations of individual particles (factor $\sigma_u^2/\bar{u}_p$). Note that if we replace the values of L, σ_u, and $\bar{u}_p$ by the measured values, we find that the variance of $\dot{n}_0$ is substantially affected by L.

Experimentally, the water discharge was unchanged compared to run A, but the water level rose considerably due to the higher dissipation rate at the bottom (see Table 4.2). The injection rate being unchanged, the beads were mostly in saltation; rolling motion occurred marginally (it contributed to the solid discharge at less than 1.5%). We counted 2321 leaps, with a mean length and height of 6.5 and 1.2 particle diameters, respectively. The values of the dimensionless leap length and height for our experiment B are nevertheless consistent with Niño *et al.'s* work [NGA94], despite the substantial differences in the two experimental configurations. Because of the variability induced by the collisions with the channel bottom, the particle velocity varied within a wider range: The average value $\bar{u}_p$ and the standard derivation σ_u were 0.44 m/s and 0.10 m/s respectively. The number of particles in the window (see Fig. 4.7) ranged from 0 to 10 (versus 0 to 7 for the smooth base). As a consequence, the pdf plot of the solid discharge was continuous and bell-shaped at first sight. A closer look reveals that there were several local maxima in the histogram but they were less pronounced than those observed in experiment A. As shown in Fig. 4.8, the empirical distribution is in fairly good agreement with the theoretical expression: The local peak positions and the tail behavior are reasonably described by the theoretical predictions.

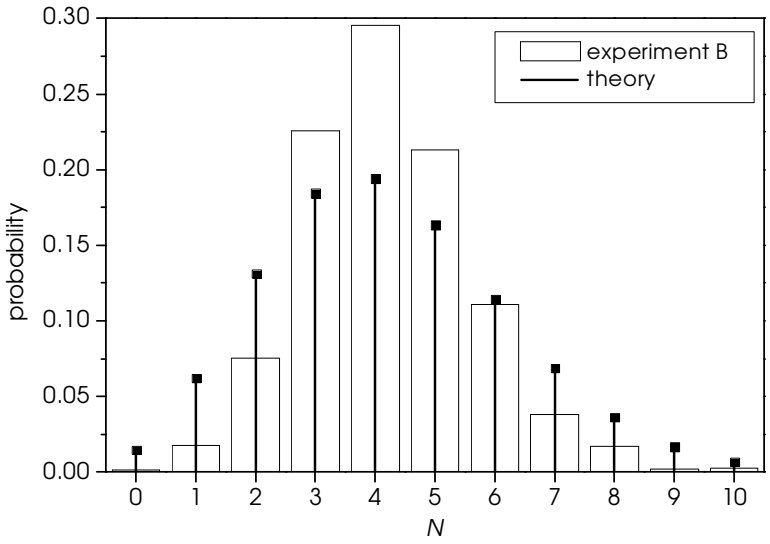

Fig. 4.7: Probability distributions of the number N of particles counted in the observation window. The white histogram represents experiment B and the black lines a theoretical distribution (Poisson distribution).

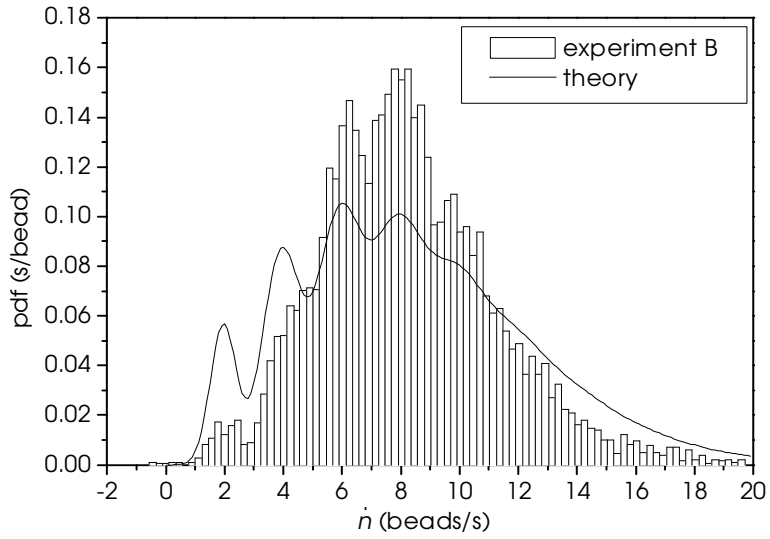

Fig. 4.8: Probability density functions (pdf) of the solid discharge $\dot{n}$. The white histogram and the black line represent the empirical and the theoretical pdf, respectively.

Time correlation

The autocorrelation of the signal has been reported in Fig. 4.3. Note that there are slight differences between the autocorrelation functions pertaining to experiments A and B. Easier to interpret is the intercorrelation function. Here the intercorrelation function of the solid discharges was computed in either window half. The resulting function has been plotted in Fig. 4.6. For experiment B, the correlation maximum was situated at $t_B = 0.25$ s. This characteristic time is consistent with the mean time a bead takes to travel half of the window: $t = L/(2\,\bar{u}_p) = 0.26$ s. Compared to experiment A, the peak of the function was slightly less acute and spread out more widely. This shows that particle flow was not only advected with mean velocity $\bar{u}_p$, but there was also a diffusive process induced by particle velocity fluctuations.

In short, experimental results provide evidence that solid discharge fluctuations come from both finite-size effects of the observation window and, to a lesser extent, particle velocity fluctuations.

For a fixed corrugated bed, solid discharge fluctuations came from both finite-size effects of the observation window and particle velocity fluctuations.

4.4.3 Ordered mobile bed (experiment C)

The next step was to study the interaction between the particles and a mobile bed (see §2.5.2). Compared to experiments A and B, the chief difference is that the moving solid phase can exchange particles with the mobile bed. The assumptions used in the heuristic model described in §4.4.2 are no longer valid, notably because the particle velocity fluctuations cannot be described by a Maxwellian distribution, since particles experienced different types of motion (rolling, saltating, entrainment/deposition). A problem in interpreting experiment C results (and afterwards experiment D) is that, as far we know, there is currently no microstructural theoretical work on the particle exchanges between a mobile bed and a turbulent stream transporting coarse particles. Compared to simple experimental configurations A and B, it is more difficult to distinguish between artificial and intrinsic fluctuations of solid discharge. This led us to thoroughly examine the flow features by relating the solid discharge to particle trajectories.

Experimentally, because of the interplay between solid and fluid phases, solid and water discharges could no longer be set independently. In order to

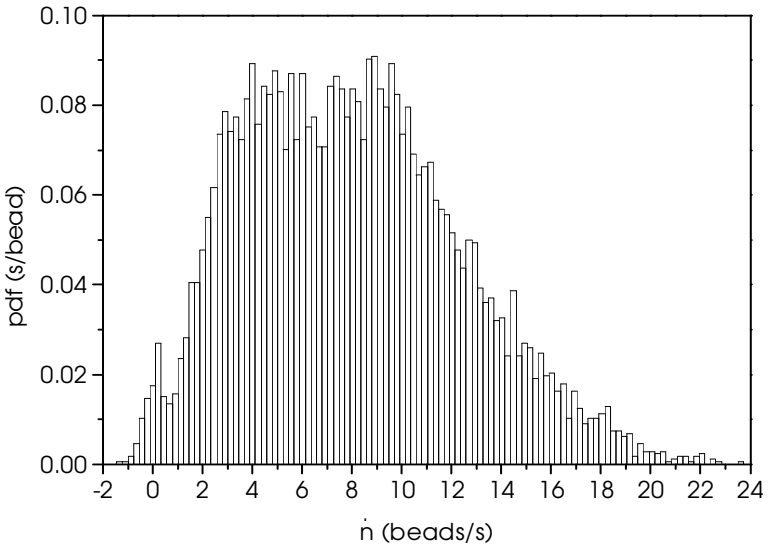

Fig. 4.9: Probability density function (pdf) of the solid discharge $\dot{n}$ for experiment C.

enforce bed load equilibrium, the water discharge was set to a considerably lower value for experiment C than for the other experiments. However, the water level was only slightly lower than in experiment B (see Table 4.2), (i) as a result of energy dissipation induced by particle collisions and (ii) because the bed surface was less regular. Beads were observed in the saltating, the rolling, and the resting regimes. This is why the number of leaps counted (1437) was lower than for experiment B. The mean leap length and height reduced to 3.7 and 0.37 particle diameters, respectively, which is significantly lower than values found by other authors because the trajectories of saltating particles were extremely constrained by the water free surface and the mobile bed.

Figure 4.9 shows a fairly compact probability distribution for the flow rate $\dot{n}$. The small spike at approximately 0 indicates that there were phases without bed load transport. The distribution showed a large plateau between the values of $\dot{n} \approx 3$ beads/s and $\dot{n} \approx 11$ beads/s, as though the flow rate was uniformly distributed within this range.

Time correlation

The autocorrelation of the solid discharge has been reported in Fig. 4.3. Compared to experiments A and B, the time correlation was increased. This enhanced memory effect can result from (i) the increased number of particles in the observation window and (ii) decreased mean particle velocities for experiment C compared to runs A and B. Note that there was not much difference between experiments C and D, despite their significant differences as regards the solid-discharge probability distribution. We have also computed the intercorrelation function (see Fig. 4.6). The characteristic time of the intercorrelation function $t_C = 0.36$ s was longer than for the previous experiments. We measured a mean velocity for the beads in the rolling regime ($u_r = 0.062$ m/s) and another one for the beads in saltation ($u_s = 0.30$ m/s). Only the latter yields a travel time ($t = L/(2\,u_s) = 0.38$ s) that was consistent with the time given by the intercorrelation function. The peak was wider and lower than that observed for the previous experiments, which reveals a substantial diffusion of the flow rate in the streamwise direction. In this experiment, intermittent motion was frequent: A number of beads experienced different rolling and resting regimes. These beads needed much more time than the characteristic time t_C to travel half of the window, which contributed to increasing the tail of the intercorrelation function.

Vertical distribution of the solid discharge

In order to gain insight into the properties of $\dot{n}$, we examined how the flow rate $\dot{n}$ was distributed in the vertical direction. The background of Fig. 4.10 was obtained by superimposing all the images of the filmed sequence. In the lower part of the figure, beads can be clearly distinguished because they did not move during the sequence. Above this stationary bed, intermittent movements of beads can be observed. Far from the stationary layers, the image becomes blurred and lighter because fast-moving beads left only fuzzy traces. In experiment C, the layer structure of the bed is obvious.

This can also be seen in the curve of the time-averaged solid discharge as a function of the flow depth reported in the same figure. In addition, we plotted the individual contribution of saltating, rolling, and resting phases to the total discharge. The diagram reveals a splitting of the solid discharge into three fractions across the y-axis. The small peaks at $y = 6$ mm and 12 mm mainly represent transport at very low velocities, i.e., beads in the resting regime. The peak at $y = 18$ mm reflects the predominance of the rolling regime, whereas the peak at $y = 25$ mm represents the saltating frac-

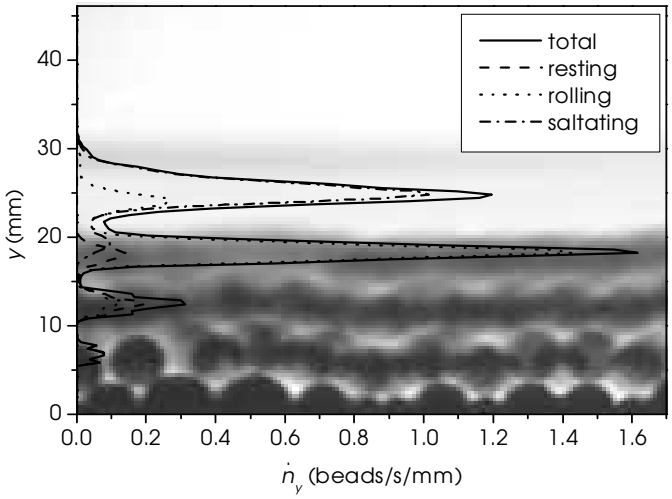

Fig. 4.10: Solid discharge $\dot{n}_y$ as a function of the y-coordinate, divided into the fractions of the state of movement, for Experiment C. In the background the cumulated images of the sequence are plotted.

tion. The distance between two peaks corresponds to the particle diameter d. The formation of sharp peaks in the diagram provides evidence that the structure of horizontal bead layers in experiment C influenced a great deal the transport. The solid discharge can thus be decomposed mainly into the saltating regime (41.4%) and the rolling regime (46.6%); the contribution of the beads at rest (moving at low drift velocities) was low (10.0%).

Bed structure

These solid-discharge properties depend to some extent on the particle arrangement of the bed. To study the structure of the two-dimensional bed more precisely, we calculated the packing fraction C_p of the beads at rest. For this purpose, we calculated the border polygon in the (x, y)-plane that included all the centers of the beads at rest. The packing fraction was defined as the ratio between the part of the surface occupied by beads to the total surface of the polygon. The time-averaged value was $C_p = 0.846$, which lay midway between the values of a square lattice ($C_p = 0.785$) and a triangular lattice, the densest packing ($C_p = 0.906$). The packing fraction parameter was not sufficient to describe the bed structure given that it differed only slightly between experiments C and D (see also §4.4.4).

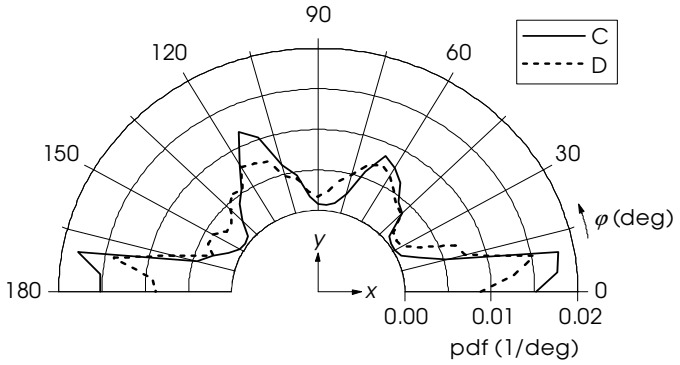

Fig. 4.11: Pdf of the contact angle φ between the beads at rest. Experiments C and D.

We therefore examined the local order of the arrangement considering neighboring particles. This leads to introducing the contact angle: The contact angle φ is defined as the angle between the x-direction and the line linking the centers of mass of two beads in sustained contact. Figure 4.11 plots the time-averaged probability density function of contact angles for all the beads constituting the bed (solid line for experiment C). A polar plot was used for an easier comparison with the images of Fig. 4.1; a bin size of 5° was chosen. Only the range 0–180° of the function is shown. It can be seen that contacts were found most frequently in the horizontal direction. This heterogeneity in the contact angle distribution results from the statistical computation being made on a collection of beads, which spanned nearly 40 particle diameters in the x-direction, but only approximately three in the y-direction. There is a second maximum near 120° and a third one at 60°, revealing that the bed structure was not too far from a crystalline structure (triangular lattice). Contacts in the 120° direction were more frequent than those in the 60° direction. This indicates that beads in the upper part of the bed frequently came to a halt against a bead in the downstream direction, at an angle of 120°. There were almost no contacts between these peaks.

Since the bed was permanently rearranged as a result of interactions with moving particles, it tended to build up regular structures. The disorder imposed by the channel base was not sufficient to prevent formation of horizontal layers. The order in the bed implied an intermittent movement of fairly long series of particles. The fluctuations of the solid discharge were, to some extent, influenced by the bed arrangement.

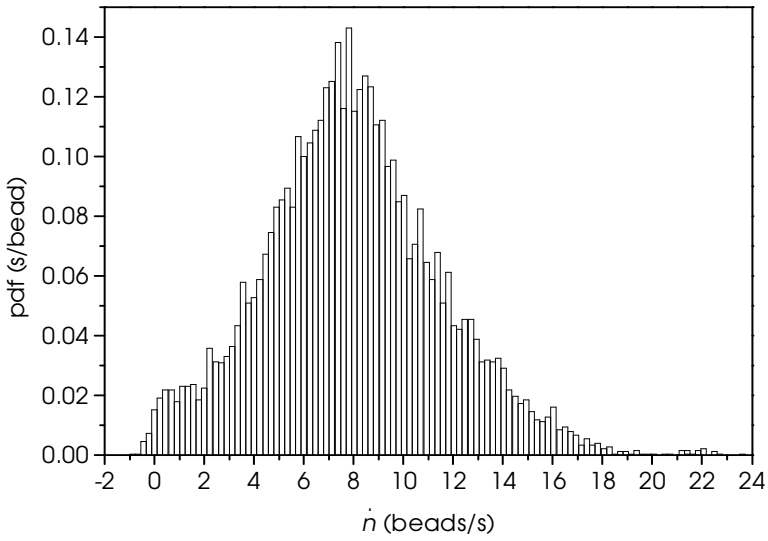

Fig. 4.12: Probability density function (pdf) of the solid discharge $\dot{n}$ for experiment D.

4.4.4 Disordered mobile bed (experiment D)

Our intention was to reduce artificial ordering effects of a two-dimensional particle arrangement as much as possible. To limit the formation of horizontal bead layers, we constructed another channel base (see Fig. 4.1(d)). Similarly to experiment C, beads were observed in a saltating/rolling regime. However, the bead arrangement of the bed changed the characteristics of the transport considerably. We counted 1461 leaps with a mean length and height of 4.4 and 0.50 particle diameters, respectively. The augmentation with respect to experiment C was due to the increase in the water depth. The water discharge when bed-load equilibrium conditions were achieved was considerably higher than for experiment C; the water depth value was thus higher as well. The pdf plot of the solid discharge was bell-shaped and nearly symmetric (see Fig. 4.12). There was, however, an accumulation of phases with low transport rates ($\dot{n} \approx$1 bead/s) .

Time correlation

The characteristic time of the intercorrelation function was $t_D = 0.33$ s (see Fig. 4.6) and differed only slightly from that of experiment C. The mean velocity of the saltating beads ($u_s = 0.30$ m/s) was very close to

the velocity found for experiment C. As previously, the characteristic time can be directly related to this saltating particle velocity, but not the rolling particle velocity ($u_r = 0.062$ m/s).

Vertical distribution of the solid discharge

As for experiment C, we calculated the time-averaged solid discharge as a function of the y-coordinate (see Fig. 4.13). Here, rolling and saltating phases appeared in wider, overlapping zones. Both saltation and rolling zones showed a peak at $y = 26$ mm, the rolling zone had an additional peak at $y = 19$ mm. While the peaks were less pronounced than for experiment C, the distance between them still corresponded to d. The solid discharge could be broken down into three contributions: 56.9% of $\dot{n}$ resulted from saltating particles, 36.1% from rolling beads, and 7.0% from creeping beads of the bed (versus 41.4%, 46.6%, and 10.0%, respectively, for experiment C). Compared to experiment C, the rolling movement was less frequent.

This can be shown by looking at the superimposed images of the sequence in the background of Fig. 4.13: There was more disorder in the bead arrangement, which prevented long layers of beads from sliding. In other words, to reach the imposed total solid discharge, the water stream was more intense than for experiment C (flow rate 40% higher than for experiment C) and therefore could transport more saltating particles. This reveals the tremendous interplay between the water flow rate, the bed arrangement, and the moving solid phase: Small changes in the bed configuration led to substantial variations in the water flow rate and solid phase features.

Small changes in the bed configuration led to substantial variations in the solid concentration of the flow.

Bed structure

The changes in the bed configuration mainly resulted from the particle arrangement. Indeed, the packing fraction of the resting beads $C_p = 0.827$ was only slightly lower than the value obtained for experiment C. Differences in the bead arrangement could be seen in the pdf of the contact angles shown in Fig. 4.11 (dashed line for experiment D), which was more evenly distributed than for experiment C. The maxima were lower and the minima less pronounced. However, the crystalline symmetry was not completely broken.

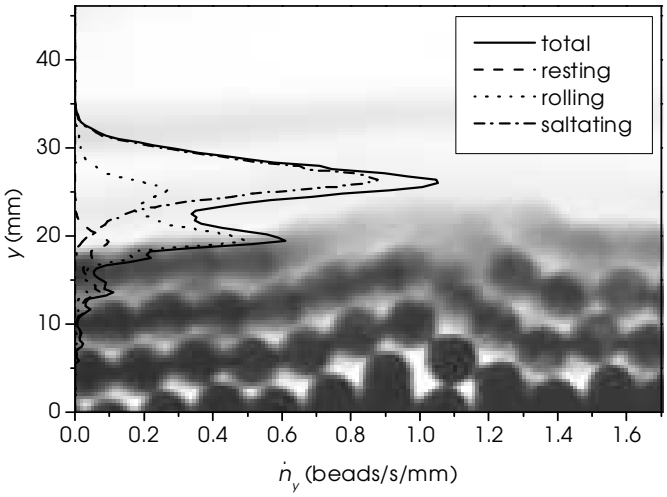

Fig. 4.13: Solid discharge $\dot{n}_y$ as a function of the y-coordinate (total solid discharge and elementary contributions) for experiment D. In the background the cumulated images of the sequence are plotted.

Bead propagation

To relate solid-discharge fluctuations to particle trajectories, it is interesting to examine the spatiotemporal bead propagation by reporting the particle movement in the (x, t)-plane. Figure 4.14 shows the bead propagation, including a sketch of how the diagram was obtained. Only beads in saltation (black lines) and rolling (gray lines) are presented, beads at rest have been omitted for the sake of clarity. Beads entered the observation window on the left and left it on the right. The time propagation is downwards. Since the x-component of the velocity of a bead is the ratio between the x-displacement and the elapsed time, it is equivalent to the slope of the trace. Given that beads usually moved faster in the saltating regime than in the rolling regime the $\Delta x/\Delta t$ quotient was larger, which can be seen in the diagram. Note as well that the beads in saltation typically travelled distances as long as the window length before coming to rest, whereas beads in the rolling regime often moved only a few bead diameters before stopping again.

Furthermore, different events (at a certain x-position and a certain time, see Fig. 4.14) could be observed, for example:

(a) A bead in saltation overtook another one in the rolling regime and the traces intersected (see Fig. 4.14 at $x \approx 80$ mm, $t \approx 0.1$ s).

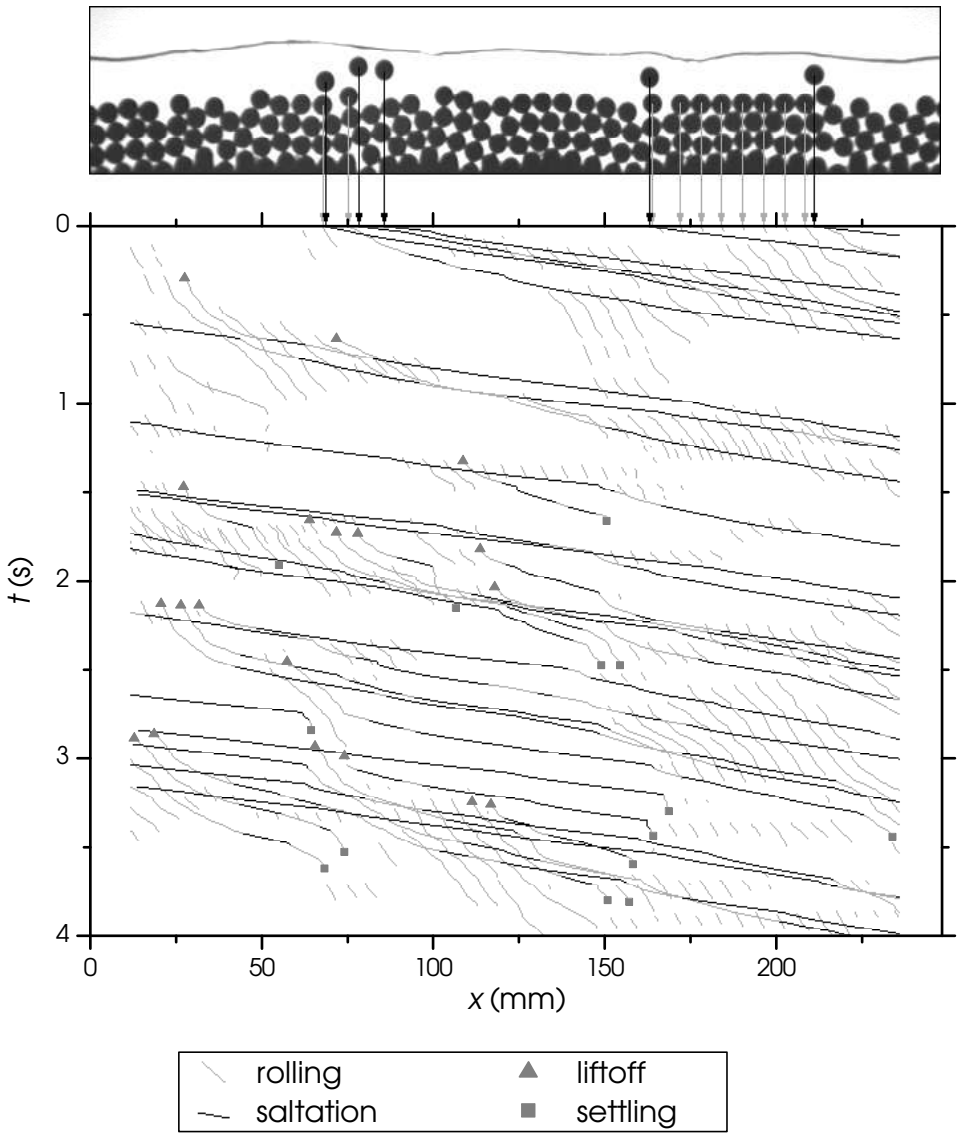

Fig. 4.14: From the image sequence to the bead propagation in the plane (x, t). Experiment D.

(b) A series of four particles was set into rolling movement (see Fig. 4.14 at $x \approx 150$ mm, $t \approx 0.4$ s).

(c) A bead in saltation was decelerated suddenly because of a collision with another bead. It switched into a rolling regime but returned to saltation a few images later. The bead that had been hit moved about one diameter then came back to rest (see Fig. 4.14 at $x \approx 150$ mm, $t \approx 1.5$ s).

Note that, in the diagram of Fig. 4.14, we show only 4 s of the sequence, whose total duration exceeded 60 s. The cited events were nevertheless typical of the experiment and reproduced with modifications over the whole sequence.

The diagram shows that there were beads frequently switching between rest and rolling; others were switching between the rolling and the saltating regimes, whereas the transition from rest to saltation via rolling (or from saltation to rest) was rare. We studied these cases of a bead liftoff and settling more precisely. This first required defining the regime transitions more accurately. A bead that stayed at least five images (0.039 s) at rest and then (at least) five images in saltation (with a rolling phase of arbitrary duration in-between) was defined as lift off; settling was defined in the same way. In the diagram of Fig. 4.14, we marked the transition from rest to rolling (respectively from rolling to rest) of the liftoff events (resp. the settling events) by triangles (resp. squares). A striking feature is that the liftoff and settling events often occurred in tight ranges of x. We observed for example seven liftoffs in the range of 10 mm $< x <$ 40 mm in the time period 0 s $< t <$ 3 s and eight settling events in the range of 140 mm $< x <$ 170 mm in the period 1.5 s $< t <$ 4 s. This basically resulted from bed structures, as shown in Fig. 4.15: A downward step in the bed forced the ejection of beads and an upward step made beads in saltation collide and come to rest. These structures were typically active for several seconds until the bed rearranged.

Bed structures governed the liftoff and settling of particles.

4.5 Conclusion

In this chapter the fluctuations of the solid discharge measured with our experimental setup have been investigated. Consistently with field observa-

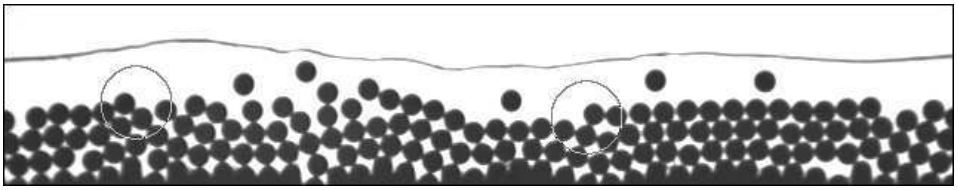

Fig. 4.15: A single image of the sequence at $t = 2.0$ s. It shows a downward and an upward step which provoke the liftoff and the settling of beads respectively. Experiment D.

tions, preliminary experiments revealed substantial fluctuations in the measured solid discharge, whereas the flow conditions were kept stationary on average.

We ran a series of four experiments (A–D) with a growing number of processes involved, to understand and discriminate the origins of these fluctuations. Experiments provided clear evidence that these fluctuations resulted, to a large extent, from the finite size of the observation window. Experiments A and B done with a fixed bed showed that solid discharge also inherited stochastic properties exhibited by individual particles. Fluctuations were exacerbated when the bed was mobile (runs C and D), that is, deposition and entrainment of particles were made possible. Mobile bed experiments were also characterized by a spectacular change in particle transport behavior, notably in the occurrence of rolling and saltating regimes. Solid discharge variations with time were intercorrelated to obtain a characteristic time of particle motion. For fixed bed experiments, the characteristic time was nothing but the average time for a particle to travel the length of the observation window. For mobile bed experiments, the characteristic times were found to be larger; they corresponded to the mean downstream velocity of the saltating phase. A striking result is that, although the probability density function of the solid discharge differed significantly between runs C and D, there was not much difference between their intercorrelation functions.

Another notable result is that solid discharge depended a great deal on bed arrangement. Although the solid discharge was kept constant for either experiment, the water discharge at equilibrium was 40% higher for experiment D than for experiment C; moreover, the saltating movement was more frequent for run D compared to run C. Regime transitions (rolling from rest, saltation from rolling) depended a great deal on the bed arrangement: It was shown that (i) the local dynamics (liftoff, settling) was largely depen-

dent on the bed arrangement and (ii) there were space and time correlations in the regime transitions, implying collective changes in particle behavior. This observation is of fundamental importance from the theoretical viewpoint because it emphasizes the importance of taking into account particle arrangement in the study of regime transition. Apart from a few recent experimental investigations [PDEF02] and [WC03], there are very few theoretical or experimental works that have been devoted to this topic.

Chapter 5

Influence of flow rate and slope[1]

Abstract: The influence of flow rate and slope on the processes of bed load transport was investigated. Firstly, we varied the solid discharge, adjusting the water discharge to obtain bed load equilibrium. An increase in the solid discharge mainly boosted the transport near the water free surface, while the particle transport in the lower part remained nearly constant. Furthermore, we identified particle liftoff and settling zones, which were correlated with the local shape of the channel base. These zones expanded if the particle injection rate was raised, but they barely changed place. When the channel slope increased, the ratio of particles transported in the saltating regime decreased. For steep slopes, the water depth was reduced to the order of one particle diameter, which forced the particles to stay in mutual contact and displace in the rolling regime. For still lower water depths, it was impossible to reach bed load equilibrium.

5.1 Introduction

The objective of this chapter is to study the influence of the flow rate and the channel slope on the processes of bed load transport. This is the natural continuation of the preceding chapter which helped, amongst other things, to estimate the assets and drawbacks of the experimental setup. Here, the use of automated image and data processing algorithms (presented in chapter 3) was essential since we had to treat a large quantity of data.

[1] A publication is in preparation.

The prediction of sediment transport in rivers is a problem which has not yet been solved in a satisfying manner. Experimental channels have been used for a long time to infer bed load transport equations. Indeed, the list of experimental studies aiming to determine the solid discharge as a function of the water discharge and the slope is long (see for example [MPM48, FLvB76]). The main focus of the present study is not to provide new experimental data for the calibration of empirical bed load transport equations, anyway our channel was not designed for this issue. In contrast, we were able to study the individual movement of each sediment particle including the particles of the bed which to the present was ventured by few authors. In our opinion such an approach is instrumental in supporting recent particle based models.

We ran a series of experiments under various flow conditions each one under bed load equilibrium. In contrast to chapter 4, we worked throughout with channel base D on which a mobile bed was installed. At first we will present the results at a channel slope of 10% for various particle injection rates. Next we incorporate the variation of the slope. This part of the study provides results concerning especially the particle's transport modes. Furthermore, we will see that for some flow conditions no bed load equilibrium could be reached. A closer look at this made it possible, however, to evaluate the potential of the experimental setup. The chapter is closed by a conclusion on the main results.

5.2 Variation of the flow rate

To investigate the influence of the mean solid flow rate on the transport phenomena, we ran the six experiments presented in Tab. 5.1. For each chosen particle injection rate $\dot{n}_0$, we sought the equilibrium water discharge q_w for the given slope ($\tan\theta = 10\%$ in this section). We grabbed four sequences of 8000 images for each experiment, calculating respectively the trajectories and water elevations. This measure allowed us to verify that the experiments were fairly reproducible. Table. 5.1 presents, apart from the imposed variables ($\tan\theta$, $\dot{n}_0$, and q_w), the calculated flow characteristics and dimensionless numbers. We used the same formulas as in §4.3, averaging this time over the four sequences. Additionally we calculated the mean x-velocities of the rolling (u_r) and the saltating (u_s) beads. We broke down the solid discharge into the contributions of the resting (κ_{re}), the rolling (κ_r), and the saltating (κ_s) beads as well. Concerning the leaps of the saltating beads we present N_l, l_l, and h_l which are the number of leaps, the mean

dimensionless leap length and height, respectively. Leap length and height were made dimensionless by dividing by the particle diameter d.

5.2.1 Effects on the flow parameters

Figure 5.1 shows the solid discharge $\dot{n}$ as a function of the water discharge q_w (see the red squares). It is obvious that q_w had to be increased with $\dot{n}$ to maintain bed load equilibrium. This entrained an increase of the water depth h, which can be estimated by the Manning-Strickler formula [GA93] holding for uniform flows without sediment transport. The formula reads $q_w = h\, K_s \tan^{1/2}\theta\, R_h^{2/3}$ (where K_s is the Strickler coefficient, depending on the wall roughness) and predicts for our case (where $h/W > 1$ and therefore $R_h \approx W/2$) approximatively a linear increase in h with q_w. For the experiments, the growth of h was less than those of q_w (see the column Comp of Tab. 5.1), involving a slight rising of the mean fluid velocity u_f. This was expected since in our case the channel base was much rougher than the walls. The friction increased thus only little with the water depth. For larger channels ($R_h \to h$), a rise of the water discharge would entrain a more significant augmentation of the fluid velocity. At this point our channel acted unusually: The friction at the walls had its effects on a large part of the channel width keeping the fluid velocities low. A further peculiarity of the channel was that the metal bottom was much rougher than the glass walls, which could be described with two different Strickler coefficients. A study on the flow depth as a function of the water discharge for our channel (in absence of particles) can be found in [Jod04].

As the augmentation of the water discharge caused mainly an augmentation of the water depth, the Froude number Fr decreased from experiment E6-10 to E10-21 but remained above unity. According to our definition the Shields number N_{Sh} increased linearly with h. This is in line with the fact that we moved away from the threshold of motion by raising the solid discharge.

5.2.2 Effects on the solid discharge

Figure 5.1 shows additionally the particle injection rates $\dot{n}_0$ (see the crosses) in comparison to the $\dot{n}$ measured in the observation window. The deviations $\dot{n} - \dot{n}_0$ were rather low within a range of -0.6 to $+0.6$ beads/s for all of the experiments. To a certain extent these deviations must be attributed to the fact that the injection rate could only be imposed with a uncertainty of 5%. However no systematical error (i.e. positive or negative) could be revealed for

Experiment	E10-6	E10-7	E10-8	E10-9	E10-16	E10-21	Comp
$\tan\theta$ (%)	10.0	10.0	10.0	10.0	10.0	10.0	1.00
$\dot{n}_0$ (beads/s)	5.3	6.7	8.0	10.0	15.4	20.0	3.77
q_w (10^{-3} m^2/s)	4.15	4.42	5.38	5.54	8.19	10.31	2.48
h (mm)	10.2	10.8	12.2	12.5	16.9	19.4	1.91
σ_h(mm)	2.1	2.1	2.3	2.4	2.5	2.7	1.25
u_f (m/s)	0.41	0.41	0.44	0.44	0.48	0.53	1.30
$\dot{n}$ (beads/s)	5.72	6.85	7.74	9.41	15.56	20.57	3.60
$\sigma_{\dot{n}}$ (beads/s)	3.07	3.34	3.55	3.62	3.96	5.23	1.70
Re	4020	4090	4550	4570	5280	5910	1.47
Fr	1.42	1.37	1.38	1.36	1.24	1.26	0.89
Δ_{Fr}	0.446	0.404	0.387	0.384	0.276	0.260	0.58
N_{Sh}	0.113	0.120	0.135	0.139	0.188	0.216	1.91
Re_p	760	711	918	921	1000	1290	1.69
D	147	147	147	147	147	147	1.00
C_s (%)	2.40	2.69	2.50	2.96	3.30	3.47	1.45
h/d	1.69	1.80	2.03	2.08	2.82	3.23	1.91
u_r (m/s)	0.063	0.074	0.065	0.075	0.075	0.072	1.14
u_s (m/s)	0.28	0.29	0.29	0.29	0.32	0.32	1.12
κ_{re} (%)	7.6	9.3	6.6	9.1	7.5	7.2	0.95
κ_r (%)	40.6	35.3	38.6	39.3	38.1	40.5	1.00
κ_s (%)	51.7	55.4	54.8	51.6	54.3	52.1	1.01
N_l	1118	1286	1430	1399	2242	2719	2.43
l_l	3.84	4.12	4.17	4.30	4.75	5.22	1.36
h_l	0.46	0.46	0.50	0.42	0.48	0.46	1.00

Tab. 5.1: Flow characteristics and time-averaged values of dimensionless numbers characterizing bed load and water flow for $\tan\theta = 10\%$. Varying parameter: Solid discharge $\dot{n}$. The notation E10-6 indicates: $\tan\theta = 10\%$ and $\dot{n} \approx 6$ beads/s. The column Comp shows the ratio of experiment E10-21 and experiment E10-6 for each variable.

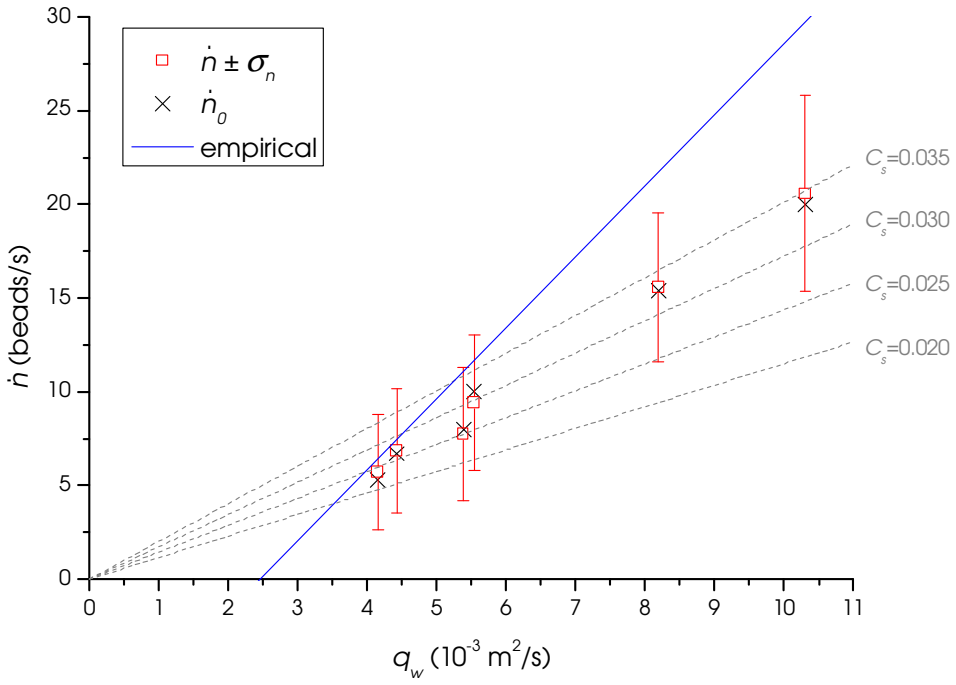

Fig. 5.1: Solid discharge $\dot{n}$ as a function of the water discharge q_w. Representation of the injection rate $\dot{n}_0$, the standard deviation $\sigma_{\dot{n}}$, the concentration C_s, and of an empirical bed load formula (see eq. (1.9) and [Ric91]). Experiments E10.

the different experiments. Another source for the deviations were the erosion and sedimentation phenomena in the zone between the channel entrance and the observation window (approximately 75 cm or 125 bead diameters long). Multiplied by the observation time (61.5 s) the maximal deviation of $|\dot{n} - \dot{n}_0| = 0.6$ beads/s reflects a supplement or a lack of 37 particles. The number of beads in the cited zone could easily vary with an amplitude of 37, since the bed elevation was evolving. Seen over the series of experiments the deviation $\dot{n} - \dot{n}_0$ seemed to vary randomly with no dependence on $\dot{n}$. This is why the relative difference $|\dot{n} - \dot{n}_0|/\dot{n}$ decreased with $\dot{n}$. As a consequence, a high particle injection rate was desirable and we renounced to investigate injection rates below $\dot{n}_0 = 5$ beads/s.

The solid concentration $C_s = q_s/q_w$ increased by 45% over the series of experiments (see the dashed lines in Fig. 5.1). An empirical bed load formulas, the Rickenmann equation (see Fig. 5.1, eq. (1.9), and [Ric91]) predicts a stronger rise of the concentration. However, these formulas are

established for bed load transport far above the threshold of motion. On the other hand, the discrepancy can be explained through the fluid velocity weakly depending on the water discharge for our channel. For higher water discharges a rather small supplement of particles was entrained by the fluid. Furthermore, the mean particle velocities for the rolling (u_r) and the saltating (u_s) motion raised only slightly, u_s being coupled to u_f.

The standard deviation of the solid discharge $\sigma_{\dot{n}}$ increased with $\dot{n}$, whereas the ratio $\sigma_{\dot{n}}/\dot{n}$ decreased, in analogy to $|\dot{n} - \dot{n}_0|/\dot{n}$ (see the whiskers in Fig. 5.1). In §4 we attributed the fluctuations of the solid discharge both (i) to the finite size of the observation window and (ii) to the influence of the mobile bed. Regarding the series of experiments E6-10 to E10-21, the effect (i) was reduced as the number of particles in motion in the observation window increased. The intrinsic fluctuations (ii), however, were larger when liftoff and settling events (see §5.2.4) became more frequent for higher $\dot{n}$. In total the fluctuations $\sigma_{\dot{n}}$ increased, but to a much lesser extent than $\dot{n}$.

5.2.3 Effects on the transport features

To compare the nature of the transport for different solid discharges we plotted the distributions of $\dot{n}$ in the vertical direction y for the six experiments (only one image sequence of each experiment has been considered) (see Fig. 5.2, solid curves). As in §4 the diagrams showed three peaks at intervals of approximately one particle diameter. Only Fig. 5.2(f) revealed a fourth peak one particle diameter above, the transport occupied here a wider y-range, as the water level was higher too. It is remarkable that the lower peaks grew only little from (a) to (f) while the uppermost peak grew progressively and produced another peak for experiment E10-21. A higher solid discharge was thus mainly achieved by an increase in the transport near the water free surface, while the particle transport below remained nearly constant.

A higher solid discharge was mainly achieved by an increase of the transport near the water free surface, while the particle transport below remained nearly constant.

While the depth of the transport zone evolved with $\dot{n}$ the relative contributions of the rolling (κ_r) and the saltating (κ_s) particles to the solid discharge stayed the same, which is perhaps the most important result of this series of experiments. Table 5.1 shows that κ_s was nearly constant for different $\dot{n}$, within a range of 51 to 56%. Approximatively constant, the

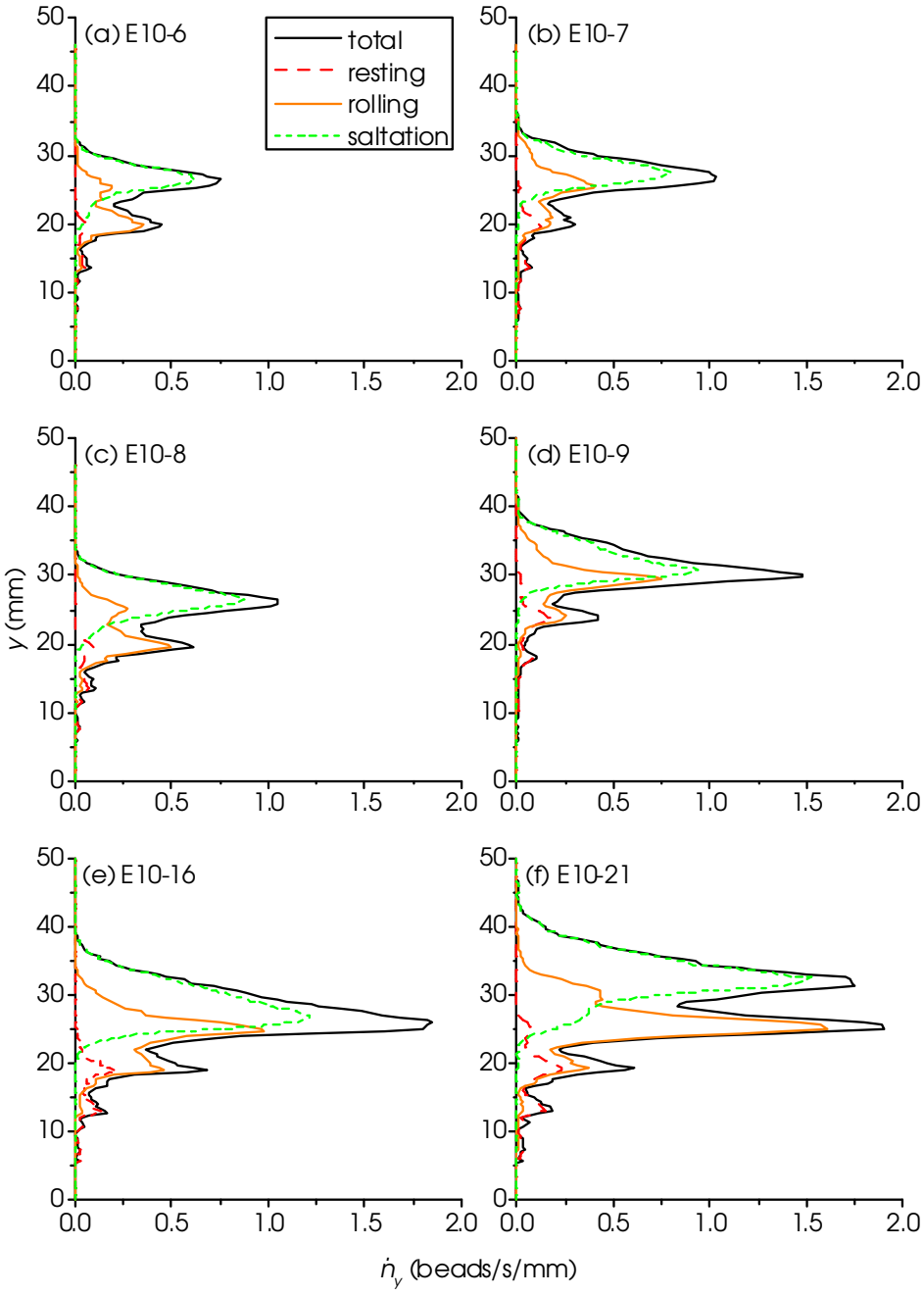

Fig. 5.2: Solid discharge $\dot{n}_y$ as a function of the y-coordinate (total solid discharge and elementary contributions) for experiments E10-6 – E10-21 ($\tan\theta = 10\%$, see Tab. 5.1). Only one image sequence of each experiment has been considered.

rolling fraction κ_r represented 35 to 41% of the solid discharge, while there where small contributions between 6 and 10% of the resting beads (κ_{re}), i.e. the beads moving at velocities lower than $u_t = 0.025$ m/s. Figure 5.2 shows further the contributions κ as a function of the vertical coordinate. It reveals that the presence of several maxima was mainly due to the rolling beads that were transported in layers, while the contributions of the beads in saltation showed single maxima in y. The diagram of experiment E10-9 (Fig. 5.2(d)) seems to be shifted upwards by nearly one particle diameter with respect to the other experiments (compare the two lower peaks). Indeed, for this experiment the bed was almost one particle diameter thicker, due to a higher obstacle at the channel outlet. As the lowest particles (y = 0 to 15 mm) were immobile the flow was only shifted by approximately 5 mm without changing its features. This confirmed that the height of the obstacle could be varied within certain limits without influencing the flow characteristics.

Studying the variables which characterize the leaps of the saltating particles (see Tab. 5.1) one notices first of all that N_l, the number of leaps detected, increased strongly with the solid discharge. The mean leap length l_l increased to a lesser extent, while the leap high h_l stayed fairly constant. An increase in the solid discharge (concerning the saltation) was thereby realized by a growth of the number of leaps, but also of the leap length.

5.2.4 Effects on the bead propagation

Low solid discharge

Further insight into the transport mechanisms at different solid discharges was provided by the diagram of the spatiotemporal bead propagation (see Fig. 4.14 in §4.4.4). At a low solid discharge as in experiment E10-6 the motion of each particle can be clearly distinguished (see Fig. 5.3). Compared to the other experiments, the mutual interference of the particles was reduced. Therefore we first tried to identify the characteristics of the transport for this case before analyzing the more complex diagram for a higher solid discharge and eventually comparing them.

The mean velocity for the saltating motion was $u_s = 0.28$ m/s, while it was $u_r = 0.063$ m/s for the rolling motion (see Tab. 5.1). Saltating beads were thus on average four to five times faster than rolling ones, which can be seen in the different slopes of the black and the gray lines in Fig. 5.3. The definition of the state of movement is obvious in the diagram: Saltating beads propagated individually (without contact to other beads), whereas

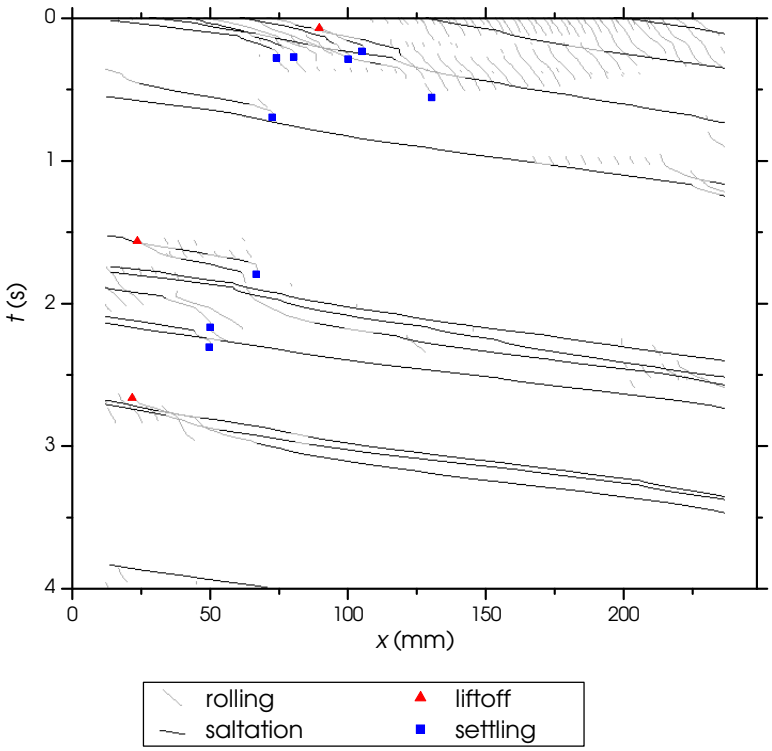

Fig. 5.3: Bead propagation in the plane (x, t), liftoff and settling events. Experiment E10-6.

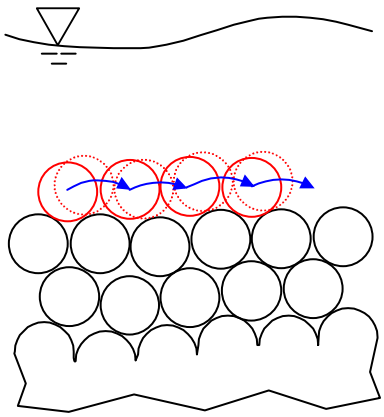

Fig. 5.4: A series of particles rolling the distance of one particle diameter.

rolling beads kept contact with the bed and moved moreover often in series. This formation of series must partly be attributed to our experimental setup. Firstly, the small width of the channel lead to particles pushing each other. In a larger channel, rolling particles would be able to sidestep others, i.e. to roll transversally avoiding a frontal collision. Secondly, particles were monosized and formed hexagonal bed structures in several zones of the channel, in spite of the special shaping of channel base D. Figure 5.4 illustrates the displacement (in the rolling regime) of a series of beads from one stable configuration to the next one, as it was typical for our experiments.

Figure 5.3 further shows that occasionally there were phases without transport in the observation window (see 1.3 s $< t <$ 1.5 s as well as 3.5 s $< t <$ 3.8 s). Usually such phases began when the last bead in motion left the observation window. Only on rare occasions, this last bead settled in the observation zone. The phases without transport ended when new particles entered from upstream. We never observed the liftoff of particles solely due to the water flow.

A temporal and spatial accumulation of the settling events (see §4.4.4 for the definition) was also obvious (see the squares in Fig. 5.3). The same held for the liftoffs (see the triangles), admittedly Fig. 5.3 shows too few events to support this statement. On this account, we show the 160 liftoff and the 186 settling events for the whole duration of the experiment in Fig. 5.5 (see below for the hatched area). Often accumulations of liftoff or settling events can be seen reflecting the erosion or the sedimentation of particles, respectively. For instance, a scatter of 16 liftoff events was situated in the

range 16 mm $< x <$ 33 mm and in the time period 43 s $< t <$ 48 s. Further downstream (with a larger extension of 37 mm $< x <$ 166 mm) an accumulation of 21 settling events can be found in the same time period. In §4.4.4, the accumulations of the liftoff and the settling events have been attributed to downward and upward steps in the particle bed which persisted for several seconds.

Even if we look at longer time intervals, it can be noted that both liftoff and settling events occurred predominantly in tight x-ranges as the horizontal lines in Fig. 5.5 point up (see below for the determination of these lines). This can be explained by means of the superimposed images of the sequence (see Fig. 5.5), which show the beads that moved scarcely during the sequence. It is striking that both liftoff and settling events occurred rarely in the zone where the bed was layered (see the range 140 mm $< x <$ 200 mm in Fig. 5.5). At the downstream end of this zone (range 200 mm $< x <$ 210 mm) the uppermost layer gave the impression to vanish while the lower layers bent upwards. This entailed that beads of the uppermost layer tended to get into saltation, i.e. to lift off. The situation was inverted upstream of the layered zone (in the range 100 mm $< x <$ 140 mm): A new layer of quasiimmobile particles formed. Beads that were initially in motion were "collected" (settling). The image in Fig. 5.5 shows that the order in the bed (averaged in time) was directly related to the local shape of the channel base. In the zone 140 mm $< x <$ 200 mm there were no abrupt transitions in the height of the neighboring half-cylinders of the channel base. In this zone the particles built up a bed of layers which were only slightly undulating. In other zones, namely for $x \approx 35$ and 220 mm, the height of neighboring half-cylinders differed by approximately $d/2$, which disturbed the layer structure of the bed. The lengths of these zones of order and disorder (especially of the layered zone) were large compared to the length of the observation window. In our experiments, only approximately 40 half-cylinders of the channel base were visible. An ideal experimental setup would allow us to film a zone that is long compared to the ordered and disordered zones in the bed.

High solid discharge and comparison

To investigate the effect of $\dot{n}$ on the bead propagation, we compared experiment E10-6 (see Fig. 5.3) with experiment E10-21 (see Fig. 5.6), which was run at a considerable higher solid discharge. As a matter of fact, this involved a much denser particle movement. The diagram shows that there were permanent interactions between the particles in motion. Phases without transport were of short duration and occupied little space (see 50 mm

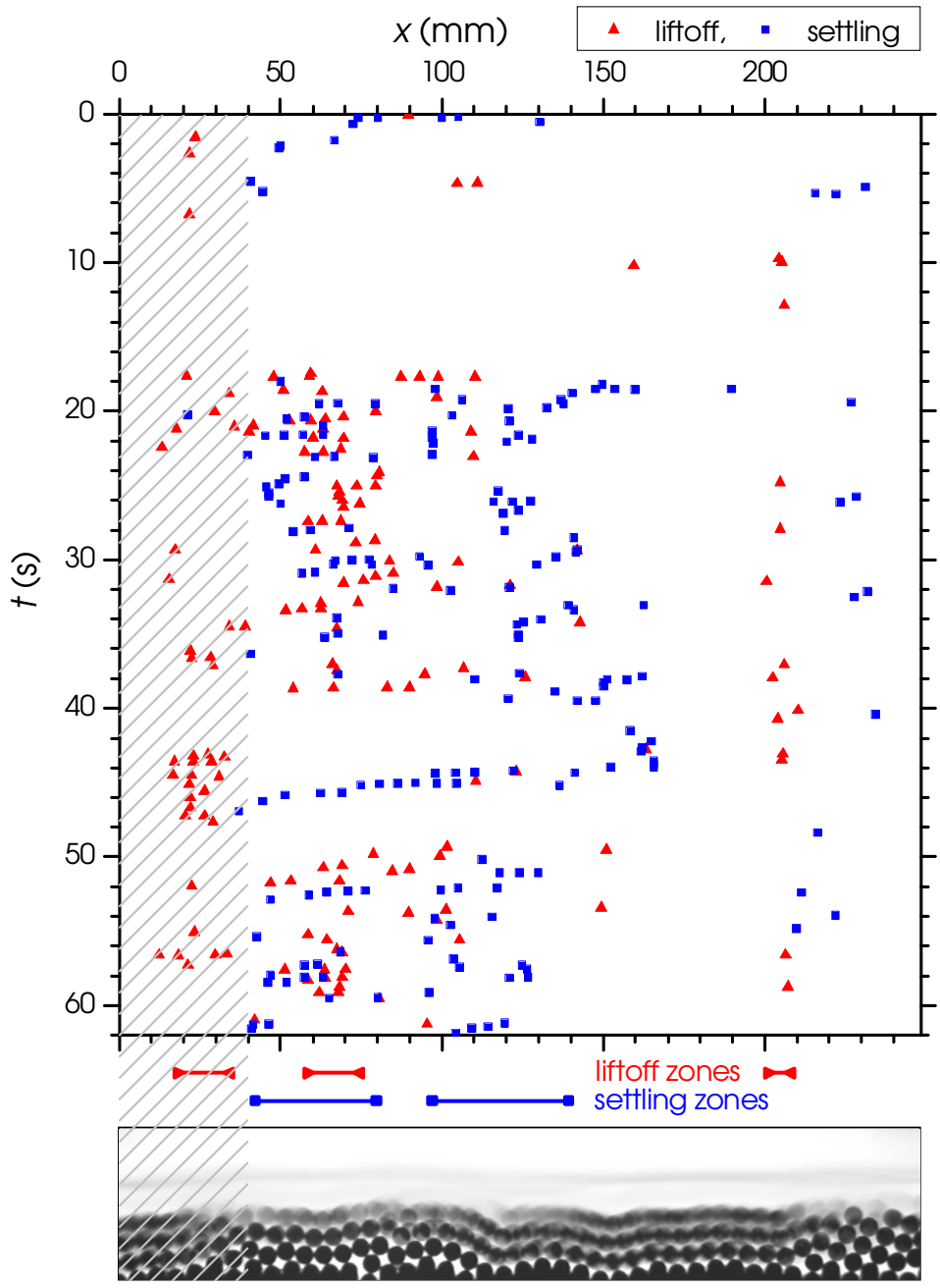

Fig. 5.5: Liftoff and settling events in the plane (x, t) for the whole sequence. Experiment E10-6.

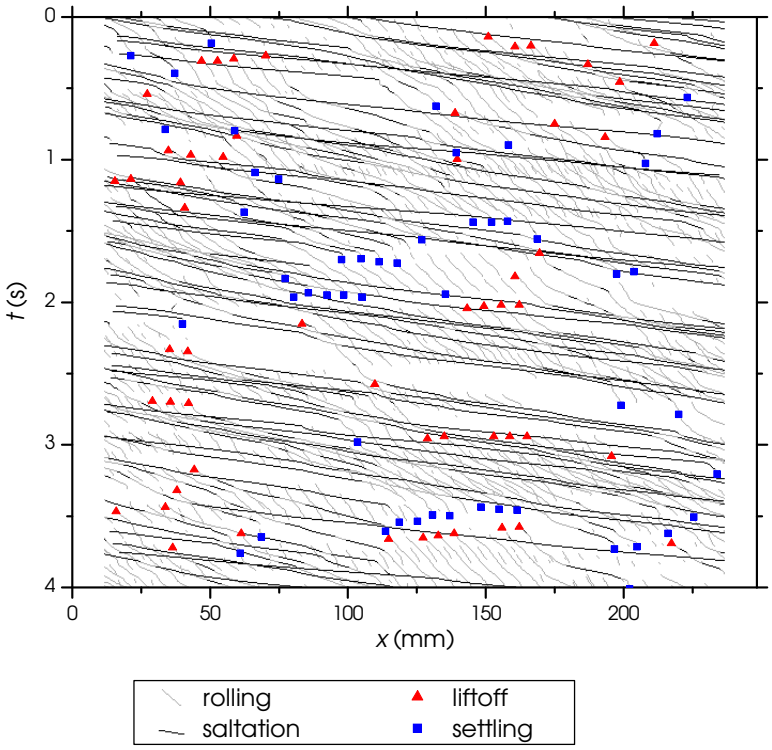

Fig. 5.6: Bead propagation in the plane (x, t), liftoff and settling events. Experiment E10-21.

$< x <$ 80 mm at 2.2 s $< t <$ 2.4 s in Fig. 5.6). The mean velocities for the saltating and the rolling motion were $u_s = 0.32$ m/s and $u_r = 0.072$ m/s, respectively (see Tab. 5.1), both of these values were only slightly higher than for experiment E10-6. As confirmed by the comparison of the diagrams, a higher solid discharge was thus achieved mainly as a result of a lower interparticle length scale (the mean distance between two particles in motion) and not a higher particle velocity. The spatial and temporal correlation of the liftoff and settling events of particles was even more pronounced than for experiment E10-6. In Fig. 5.6 the erosion or the sedimentation of series of particles can be seen at several occasions. Another peculiarity of experiment E10-21 was that several particles underwent multiple settling and liftoff processes within the observation window.

We further show the total number of liftoff (766) and settling events (791) in the (x, t)-plane in Fig. 5.7. Note that these numbers match fairly well,

since each bead underwent settling and liftoff processes alternatively during its course from the entrance to the exit of the channel. Before comparing this diagram to Fig. 5.5 it must be noted, that the location of the observation window differed between the two experiments. Due to experimental circumstances, for experiment E10-21 we filmed a zone that was approximatively 40 mm downstream with respect to experiment E10-6. The areas that have to be ignored for a comparison of Fig. 5.5 and 5.7 are hatched. The layered zone of the particle bed was thus in the range 100 mm $< x <$ 160 mm instead of 140 mm $< x <$ 200 mm.

Figure 5.8 shows a comparison of the liftoff and settling zones for the two transport rates. It reflects the frequency of the liftoff and settling events plotted as a function of the x-coordinate, a bin size of approximately one particle diameter was chosen. The liftoff and settling zones, already presented in Fig. 5.5 and 5.7, were actually determined taking the maxima of these curves. In Fig. 5.8, the diagram of experiment E10-21 has been shifted to the right to facilitate a comparison between the two experiments respecting the same local shape of the channel base. Obviously the maxima of the curves, the liftoff and settling zones, were roughly at the same locations for both of the injection rates. Settling events were frequent upstream of the layered zone (140 mm $< x <$ 200 mm) while liftoff events cumulated downstream of it. For experiment E10-21, the liftoff and settling zones were, however, longer and overlapped where the particle bed was layered, in contrast to experiment E10-6. This can be explained as follows: Series of particles (with horizontal extensions of 10 to 40 mm) frequently lifted off or settled simultaneously if the solid discharge was high.

Liftoff and settling zones were correlated with the local shape of the channel base. They expanded if the particle injection rate was raised, but they barely changed place.

5.3 Variation of the channel slope

Since the slope $\tan\theta$ is one of the crucial parameters affecting bed load transport, we ran further experiments varying the channel slope. We adjusted $\tan\theta$ to 7.5, 12.5 and 15% and studied each time several solid discharges (see Tab. 5.2) to complete the experiments conducted at 10%. Here, to limit the processing time, we grabbed only two sequences of 8000 images for each experiment and averaged over those. The calculated flow characteris-

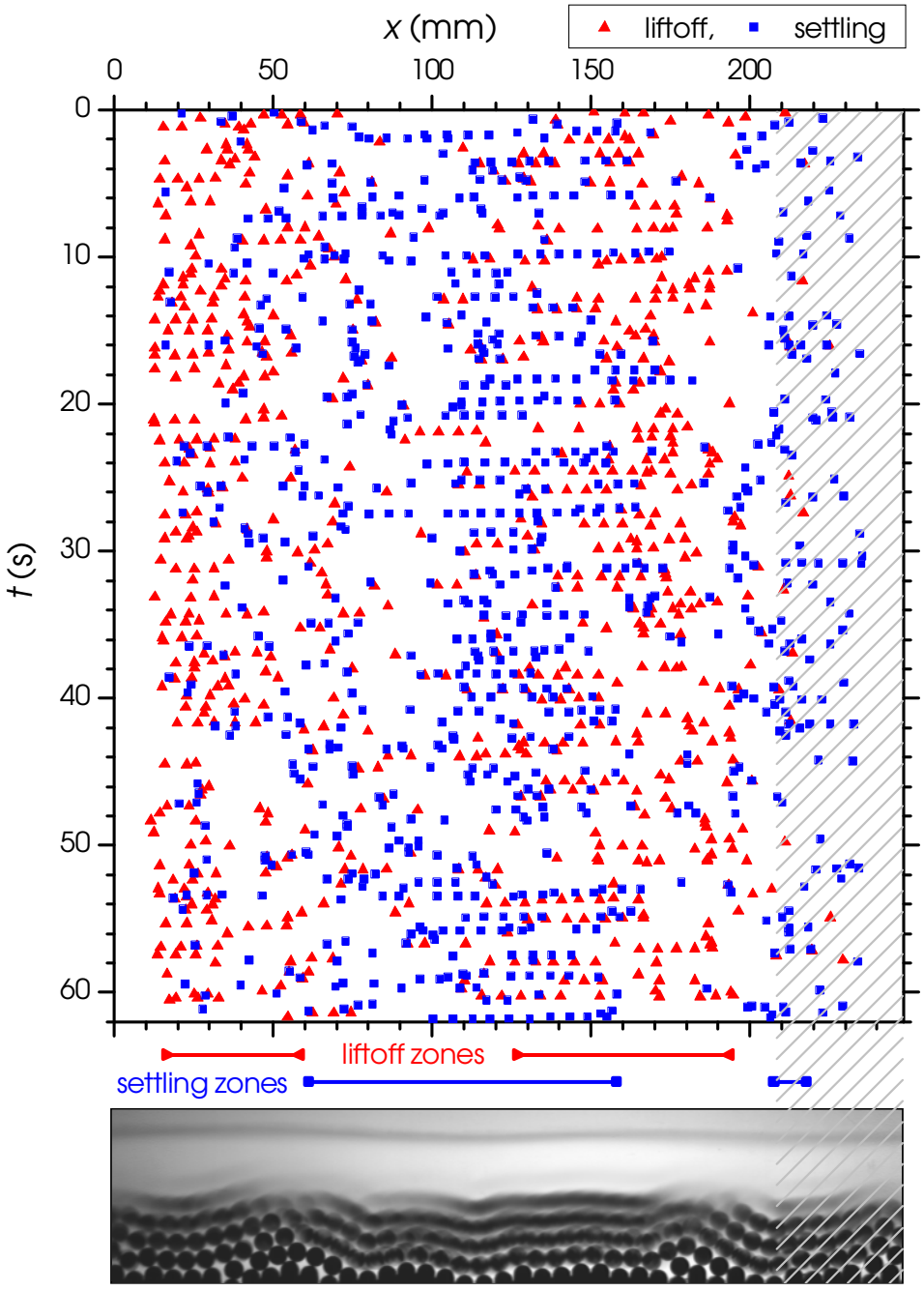

Fig. 5.7: Liftoff and settling events in the plane (x, t) for the whole sequence. Experiment E10-21.

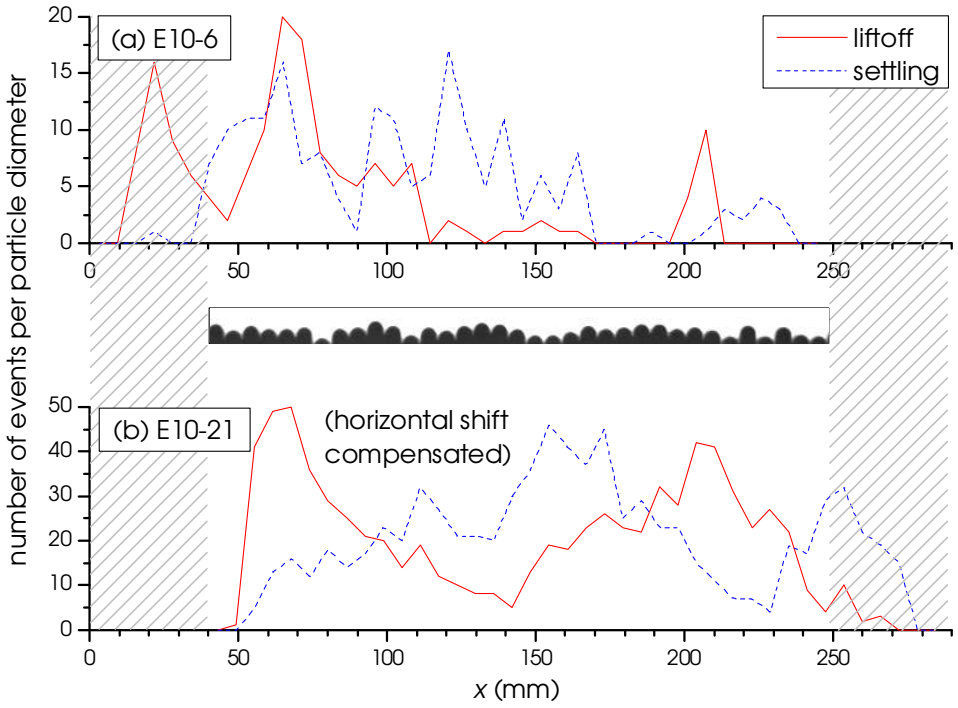

Fig. 5.8: Comparison of the liftoff and settling zones for experiments E10-6 and E10-21.

tics and dimensionless numbers presented in Tab. 5.2 correspond to those of Tab. 5.1. Figure 5.9 shows images of the particle transport for the 15 experiments conducted. Note especially the important variation of the water depth in function of the solid discharge and the slope.

5.3.1 Effects on the flow variables

In addition to a comparison of these experiments at a constant slope (as done in the preceding section), various ways of comparing the flow characteristics are possible. A comparison at a constant solid discharge seems convenient as this was a variable we imposed. However, for steeper slopes the equilibrium water discharge and thus the water depth were substantially lower, which made it difficult to extract the slope effect from the results. Similarly, if we compared several experiments at a constant water discharge, the important variation of the solid discharge with the slope would obscure the influence of any other parameter. Considering two experiments at similar water dis-

Experiment	E7-6	E7-8	E7-9	E7-11	E12-9	E12-16	E12-21	E15-16	E15-21
$\tan\theta$ (%)	7.5	7.5	7.5	7.5	12.5	12.5	12.5	15.0	15.0
$\dot{n}_0$ (beads/s)	5.7	7.8	8.7	10.9	9.3	15.2	20.0	15.6	21.5
q_w (10^{-3} m^2/s)	10.00	11.54	13.85	26.15	2.97	3.85	4.46	2.31	2.92
h (mm)	18.9	20.8	24.9	40.8	7.0	8.2	9.4	4.9	6.7
σ_h(mm)	2.2	2.3	2.5	2.8	2.2	2.3	2.4	2.0	2.5
u_f (m/s)	0.53	0.55	0.56	0.64	0.42	0.47	0.48	0.47	0.44
$\dot{n}$ (beads/s)	5.45	7.76	9.20	10.99	9.52	15.52	19.86	15.45	20.55
$\sigma_{\dot{n}}$ (beads/s)	3.13	3.39	3.72	3.73	4.28	5.13	5.71	5.18	4.45
Re	5860	6230	6400	7720	3760	4360	4600	3680	3830
Fr	1.26	1.26	1.15	1.02	2.20	2.09	1.90	3.72	2.63
Δ_{Fr}	0.222	0.209	0.172	0.105	1.046	0.875	0.716	2.272	1.468
N_{Sh}	0.158	0.173	0.207	0.340	0.098	0.114	0.130	0.082	0.111
Re_p	1050	1150	1350	1990	1120	1140	1060	1720	1270
D	147	147	147	147	147	147	147	147	147
C_s (%)	0.95	1.17	1.16	0.73	5.58	7.02	7.74	11.65	12.23
h/d	3.16	3.47	4.15	6.80	1.17	1.37	1.56	0.82	1.11
u_r (m/s)	0.078	0.084	0.079	0.078	0.074	0.075	0.077	0.072	0.079
u_s (m/s)	0.35	0.36	0.33	0.31	0.24	0.28	0.30	0.18	0.23
κ_{re} (%)	6.9	5.5	6.4	5.1	12.1	12.1	10.8	10.6	7.3
κ_r (%)	29.0	28.6	31.1	30.7	68.0	63.8	57.0	84.9	76.2
κ_s (%)	63.9	65.7	62.2	64.1	19.9	24.1	32.1	4.4	16.4
N_l	849	1183	1484	1981	635	1107	1850	194	1115
l_l	5.39	5.66	5.05	4.74	2.65	3.33	3.92	1.75	2.58
h_l	0.55	0.54	0.54	0.60	0.36	0.33	0.37	0.29	0.37

Tab. 5.2: Flow characteristics and time-averaged values of dimensionless numbers characterizing bed load and water flow. Varying parameters: Channel inclination $\tan\theta$ and solid discharge $\dot{n}$. The notation E7-6 indicates: $\tan\theta \approx 7\%$ and $\dot{n} \approx$ 6 beads/s. See Tab. 5.1 for the experiments at $\tan\theta = 10\%$.

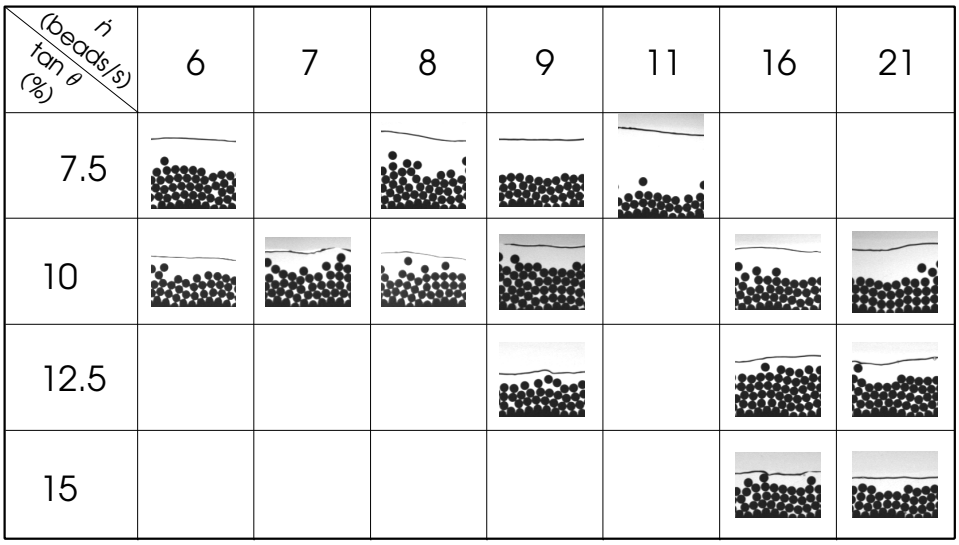

Fig. 5.9: Overview of the experiments conducted at various solid discharges $\dot{n}$ and slopes $\tan\theta$. For each experiment, a detail of one filmed image is shown. See Tab. 5.1 and 5.2 for the experimental conditions.

charges but slightly different slopes, Tab. 5.1 and 5.2 show that the solid discharge could vary by a factor of two to four. The close coupling of the flow variables (the most important ones being $\tan\theta$, $\dot{n}$, q_w, and h) made a comparison difficult and made it impossible to suppress the influence of individual parameters. In the following, we present a number of striking points of transport mechanisms when varying the channel slope.

Figure 5.10 depicts the solid discharge $\dot{n}$ as a function of the water discharge q_w with the slope $\tan\theta$ as parameter. In this diagram, each experiment is represented by two data points corresponding to the two image sequences grabbed (four for the experiments at $\tan\theta = 10\%$), which reveals a small scatter of the data. Experiment E7-11 has been omitted in the diagram as its water discharge was nearly two times higher than for the other experiments.

As already stated in the preceding section a higher water discharge provoked primarily an increase of the water depth, while the mean fluid velocity u_f augmented only slightly. Therefore u_f stayed in the tight range of 0.41 to 0.64 m/s for all the experiments reaching its maximum for low slopes. The characteristic velocities of the rolling (u_r) and the saltating beads (u_s) varied little and were still linked to u_f. This result and the results of chapter

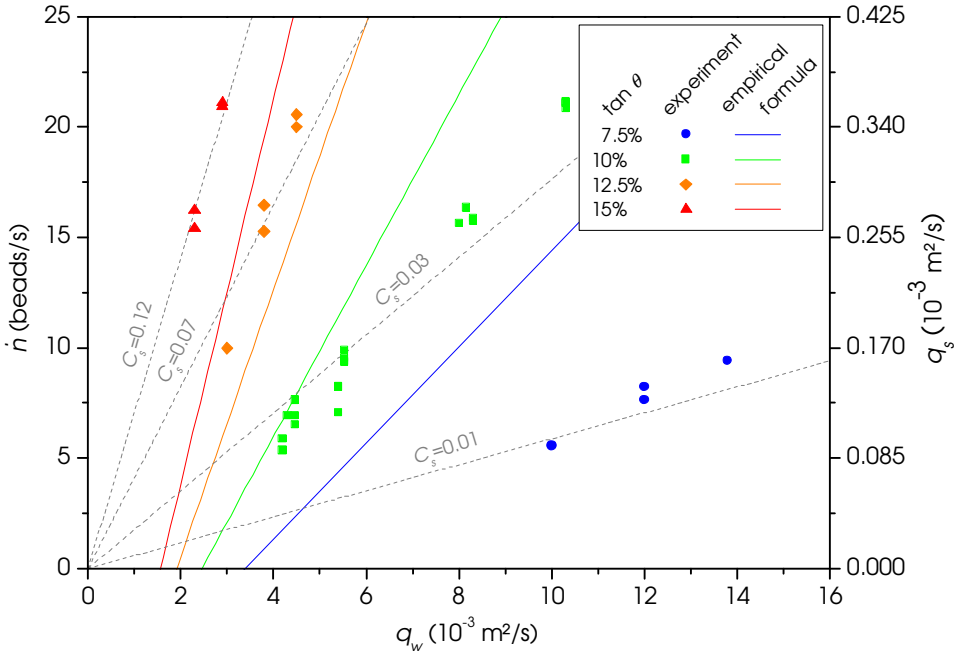

Fig. 5.10: Solid discharge $\dot{n}$ as a function of the water discharge q_w and the channel slope $\tan\theta$. Representation of an empirical bed load formula (see eq. (1.9)) and lines of constant concentration C_s. Experiment E7-11 has been omitted.

4 reveal that the characteristic particle velocities were sensitive to the fact whether or not the bed was mobile but fairly insensitive to flow variables as the solid discharge, the water discharge, or the slope. As the water depth decreased substantially with the slope, the Froude number increased in turn and reached mean values far above the critical value (for $\tan\theta = 15\%$, see Tab. 5.2).

The Shields number N_{Sh} was by definition proportional to the product $h\tan\theta$. In our case the variation of h outweighed the effect of $\tan\theta$ which explains that N_{Sh} was a decreasing function of $\tan\theta$. For experiments E12-9 and E15-16, N_{Sh} was below 0.1 and thus close to the threshold Shields number usually given for coarse particles on a slightly sloped bed ($N_{Sh,c} = 0.047$–0.06, see §1.2.2). Indeed, these experiments run at steep slopes (and thus at low water depths) showed a convergence to the threshold of motion. For a water depth lower than approximatively one particle diameter, it was actually impossible to obtain bed load equilibrium, which will be analyzed in §5.4. The standard deviation of the solid discharge $\sigma_{\dot{n}}$ (a measure for the

solid discharge fluctuations) showed no clear dependency on $\tan\theta$. For all but one slope ($\tan\theta = 15\%$), $\sigma_{\dot{n}}$ augmented slightly with $\dot{n}$.

As expected, Fig. 5.10 shows that the equilibrium water discharge diminished substantially with increasing channel slope. This involved a distinct increase of the solid concentration with slope (see the dashed lines of equal concentration). The new experiments (with exception of E7-11) confirm as well a slight increase of the concentration with the solid discharge. As above, we represent in Fig. 5.10 an empirical bed load transport formula for a rough comparison. It is remarkable that our experimental data points stayed below this transport prediction for moderate slopes, while they overshot it for steep slopes. In other words, the solid discharge was particulary sensitive to the slope for our experiments. This is probably due to the peculiarity of our channel. At moderate slopes, the effect of the channel base was dominant, particles tended to be trapped particles in the pronounced cavities. In this case the particle movement could barely be stimulated by the fluid, since an increase of q_w involved nearly no evolution of the fluid velocity. For steeper slopes the channel cavities were surmounted more easily. We assume that here the spherical nature of the particles was crucial, leading the particles to roll and slide on each other, provoking a high concentration C_s.

5.3.2 Effects on the transport features

It was once again interesting to break down the solid discharge into the contribution of the saltating and the rolling beads. In the preceding section, we found out that, for $\tan\theta = 10\%$, the relative contribution of the saltating beads κ_s was virtually constant. In general, however, this variable turned out to be coupled to channel slope and to water depth h. We plotted thus κ_s as a function of h/d for the different slopes (see Fig. 5.11). The whiskers reflect the standard deviation $(h \pm \sigma_h)/d$. For $\tan\theta = 7.5\%$, κ_s was higher, but still constant (between 62.2 and 64.1%). We can thus conclude that for moderate slopes (7.5 and 10%), κ_s was a function of $\tan\theta$ only. For steeper slopes though (12.5 and 15%), the diagram shows that κ_s was a linear function of h/d independent of $\tan\theta$.

A closer look at the flow images of Fig. 5.9 helps to understand this relation. For $\tan\theta = 12.5$ and 15%, beads in saltation touched the water free surface regularly, their vertical motion was limited by the low water depth. This is probably why saltation was impeded here, many particles had to be transported in the rolling or sliding motion which occupies less space in the vertical direction. The data show that saltation occurred even if the mean water depth fell below one particle diameter. This is due to

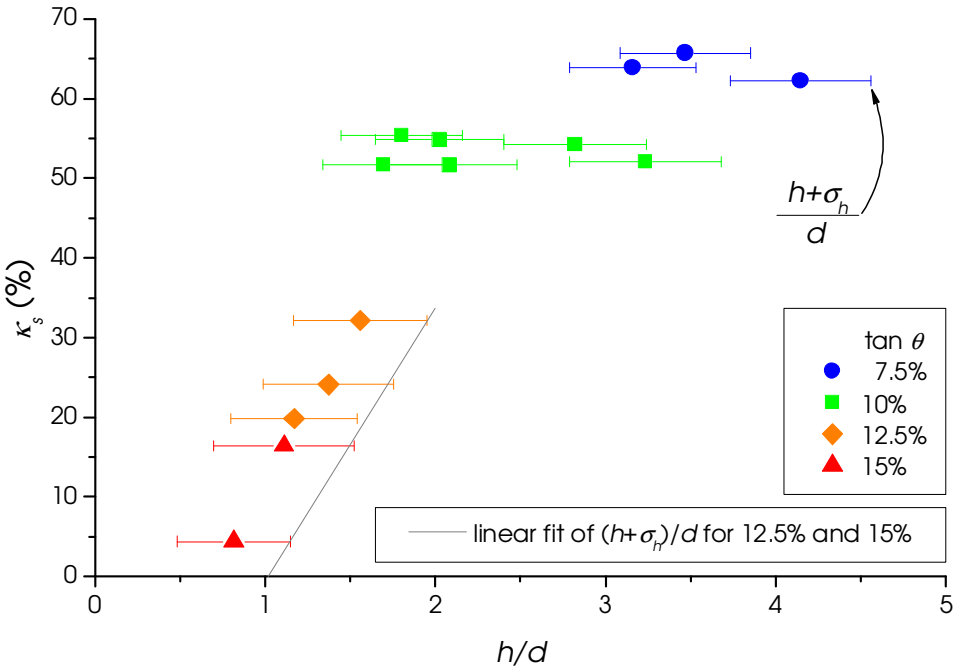

Fig. 5.11: Relative contribution of the saltating particles to the solid discharge κ_s as a function of the ratio h/d, where h and d are the water depth and the particle diameter, respectively. The whiskers reflect the standard deviation $(h \pm \sigma_h)/d$. Experiment E7-11 has been omitted.

the fluctuations of h, even in the case $h/d = 0.82$ the instantaneous water depth frequently exceeded one particle diameter and enabled saltation (see the whiskers in Fig. 5.11). This is why here we plotted a linear fit of the variable $(h + \sigma_h)/d$ for the data at $\tan\theta = 12.5$ and 15%. This line suggests a threshold of saltation at $(h + \sigma_h)/d = 1$. If the water depth raised by one particle diameter (for $(h + \sigma_h)/d = 2$), κ_s reached the value 33.7%. Note that the saltation threshold is only obtained by the extrapolation of the data presented in Fig. 5.9, experimentally we were not able to produce a flow where saltation was absent. For a water depth significantly lower than the particle diameter, no stable bed load equilibrium could be attained (see §5.4).

On the other hand, for the experiments at $\tan\theta = 7.5$ and 10%, the particle leap height was barely limited by the water depth (see again the flow images of Fig. 5.9). The contribution of saltating beads κ_s could thus freely adapt and appeared to depend only on the slope (see Fig. 5.11).

For moderate slopes the contribution of the saltating beads to the solid discharge, κ_s, depended on the slope. For steeper slopes κ_s was a linear function of h/d.

The features of the particle transport at different slopes are further illustrated in Fig. 5.12. To obtain these diagrams we counted for each pixel of the observation window the number of particles, N', that passed during the sequence. In other words the diagrams represent the superimposition of the particle trajectories by the color-coded number N'. It is striking that the rolling particles followed specific paths. At certain (x, y)-positions more than 100 particles passed. Note that at each x-position (for an arbitrary y) approximately 9 beads/s $\times$ 61 s $\approx$ 550 beads passed. The diagrams show once again the distinct layer structure of the particle transport.

While the cited features apply to each of the three diagrams shown in Fig. 5.12, several distinctions of the particle transport at different slopes were revealed. These concern mainly the particle's state of movement. At low slope (see E7-9 in Fig. 5.12) the saltation was dominant. Here, the cited paths of the rolling and sliding beads were relatively little frequented (maximal value $N' = 95$ beads). In the upper part of the diagram, there was a wide zone of transport where N' took values between 1 and 20. This was the zone of saltation. Because of the high water depth, it was rather broad. In the upper part of this zone one can notice several long leaps.

Different is the case for a steeper slope (see E12-9 in Fig. 5.12). The

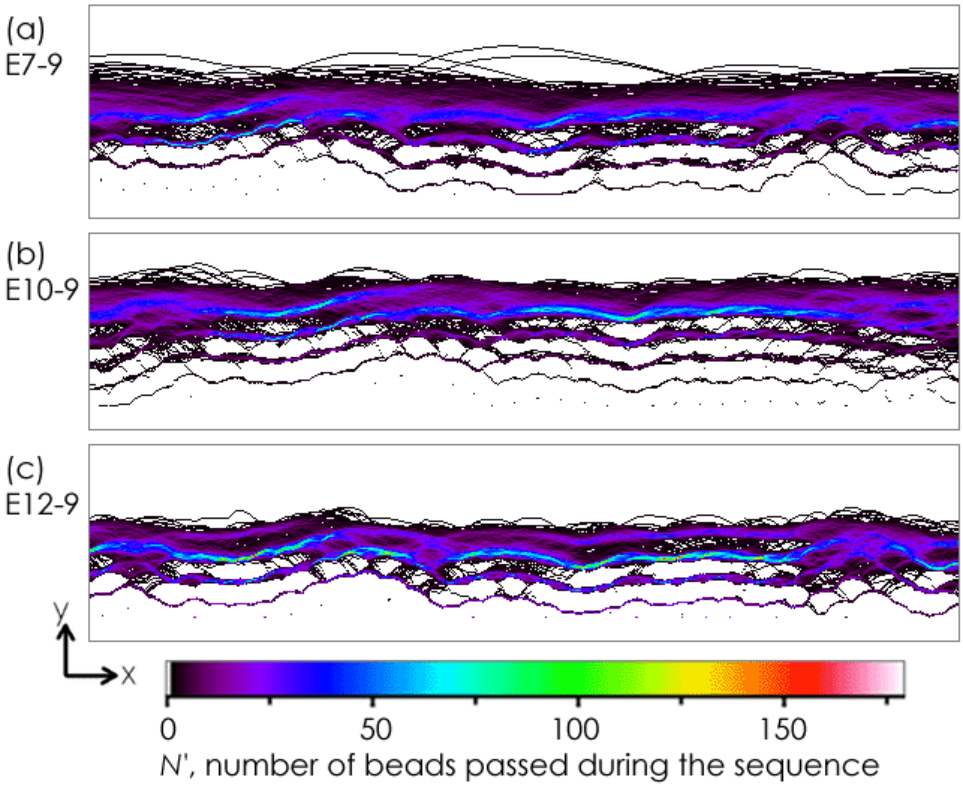

Fig. 5.12: Superimposition of the trajectories for experiments at different slopes: (a) 7.5%, (b) 10%, and (c) 12.5%. The solid discharge is fairly constant ($\dot{n} \approx$ 9 beads/s).

zone of saltation was narrower and the leaps were noticeably shorter. The data concerning the leaps given in Tab. 5.2 show that the number of leaps N_l, the leap length l_l as well as the leap height h_l were significantly smaller than for experiment E7-9. Here, the beads were predominantly rolling and followed frequently specific paths (see the green, yellow and red zones in the diagram, the maximum of N' was 175 beads).

A common way of comparing bed load transport rates for different flow conditions is to plot the dimensionless solid discharge ϕ_s as a function of the Shields number N_{Sh}. As already stated, our experimental setup was not designed to produce new experimental data to support empirical bed load equations. The plot in the (ϕ_s, N_{Sh})-diagram was nevertheless useful since it allowed us to compare our results with those of other authors and to uncover weaknesses of empirical formulas, which were established for slopes much lower than for our case. The solid discharge was made dimensionless by the definition $\phi_s = q_s/\sqrt{(\rho_p/\rho_f - 1)gd^3}$, where q_s is the bed load transport rate per unit width, $q_s = \pi d^3 \dot{n}/(6W)$. Figure 5.13 shows our experimental data points compared with two widely used empirical formulas. Both the Meyer-Peter (see eq. (1.7) and [MPM48]) and the Fernandez-Luque formula [FLvB76] make use of a transport threshold, they yield a non-zero ϕ_s if N_{Sh} exceeds a critical value, $N_{Sh,c}$. Our data was quite scattered in this diagram, the points seemed to be affected by slope. As shown above, the contribution of the saltating particles κ_s depended on the channel slope (at least via the water depth). This is why we retraced the diagram, multiplying each ϕ_s by the corresponding κ_s (see Fig 5.14). The quantity $\kappa_s\phi_s$ is thus the dimensionless transport rate of the particles in saltation. By this measurement, the scatter of the data was obviously reduced, allowing us to fit a curve. It represents an equation similar to the Meyer-Peter equation with modified coefficients and contains thus a critical Shields number. This result suggests that, for steep slopes, the transport by saltation can be reasonably described with a threshold law, while a different approach is needed for the rolling motion.

5.4 Experimental limits

The development of the experimental setup represented an important part of the practical work for the present PhD dissertation. It enabled us to run a number of experiments under various flow conditions as presented above. Carrying out preliminary experiments, we reached the limits of the experimental facility. Slope, solid discharge, and water discharge could not

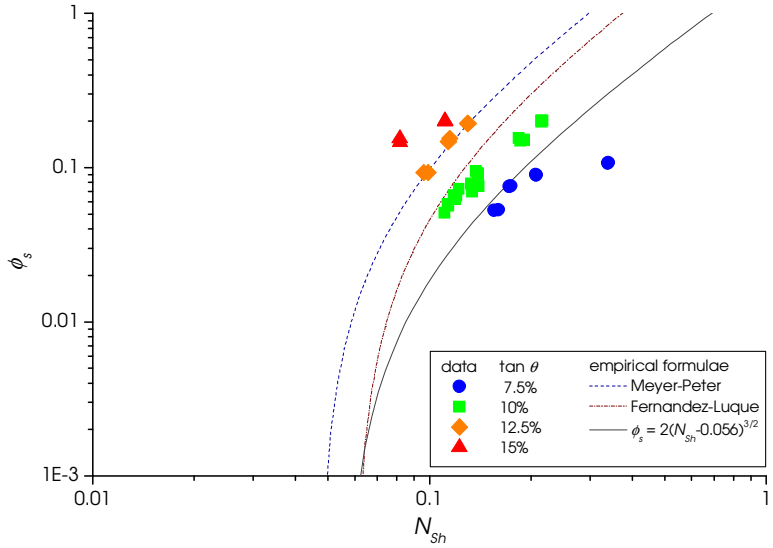

Fig. 5.13: Dimensionless solid discharge ϕ_s as a function of the Shields number N_{Sh}.

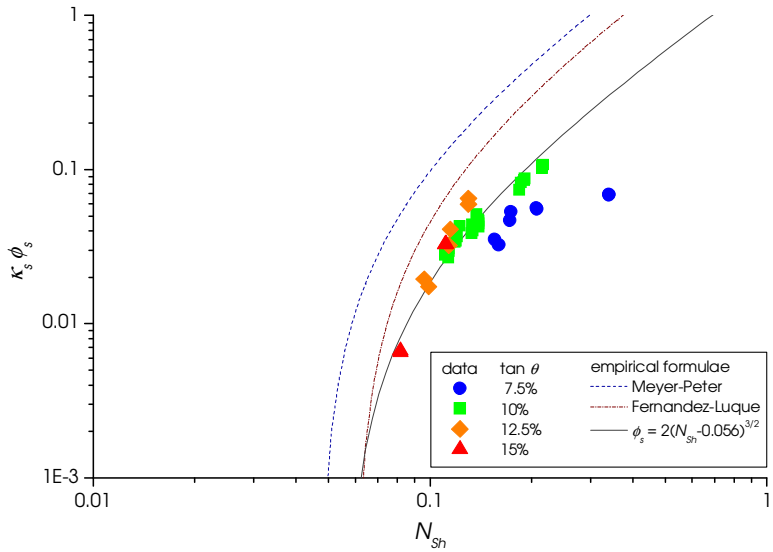

Fig. 5.14: Product of the contribution of the saltating particles and the dimensionless solid discharge, $\kappa_s \phi_s$, as a function of the Shields number N_{Sh}.

$\tan\theta$ \ $\dot{n}$	6	7	8	9	11	16	21
7.5	E7-6	-	E7-8	E7-9	E7-11	Q_w insufficient	
10	E10-6	E10-7	E10-8	E10-9	-	E10-16	E10-21
12.5	h supposed to be too low			E12-9	-	E12-16	E12-21
15	h supposed to be too low			†	-	E15-16	E15-21

Tab. 5.3: Summary of the experiments conducted an those that failed at various slopes $\tan\theta$ (in %) and solid discharges $\dot{n}$ (in beads/s). †: No stable bed load equilibrium was obtained.

be chosen arbitrarily in wide ranges. Table 5.3 indicates the limits related to the water discharge, furthermore we encountered constraints linked to the solid discharge.

5.4.1 Constraints of the solid discharge

The fact that there was an upper limit for the solid discharge (21 beads/s) can be attributed to our supply system, which injected the particles one by one. For considerable higher particle injection rates, we assume that it would be preferable to supply the particles by an adjustable hopper. However, the injection rate of our system was steady and easy to measure which was advantageous.

On the other hand, the nature of the physical system we studied prevented us from working with extremely low particle injection rates. As stated in §4.4, the fluctuations of the measured solid discharge were partly due to the small number of particles in motion observed using the camera. This issue was extreme for experiment E7-6, here, on average only $N_r = 4.53$ beads and $N_s = 2.21$ beads were observed in the rolling and the saltating motion, respectively. Each bead entering or leaving the observation zone thus modified the solid discharge on average by $1/(N_r + N_s) = 14.8\%$. For experiment E15-21, the same number yielded $1/(N_r + N_s) = 2.08\%$. As discussed in §5.2.2, a high injection rate was furthermore desirable to minimize $|\dot{n} - \dot{n}_0|/\dot{n}$, the relative difference between the injection rate and the measured flow rate.

5.4.2 Constraints of the water discharge

Firstly, the water supply was limited due to the nature of the circuit (see §2.3) which prompted us to remove the flow meter for one experimental run

(E7-11). In this case, the water depth h was substantially higher and we reached furthermore the limit of the chosen vertical image dimension (see §2.6). This forced us to reduce the bed elevation by decreasing the height of the obstacle (see the image for $\tan\theta = 7.5\%$ and $\dot{n} = 11$ beads/s in Fig. 5.9). In this way, the roughness of the channel base had more influence on the flow, which might explain that the solid concentration C_s was strikingly low for this run.

Generally, we had to prevent perturbations at the channel outlet from propagating upstream to the observation zone. The channel being short, this could only be achieved by ensuring a supercritical flow ($\mathrm{Fr} > 1$) and thus a small water depth. Indeed, the channel was designed to study supercritical flows. The cited problems that we encountered with higher water discharges let us conclude that our experimental setup was only adapted for a relatively low water depth.

Furthermore, for the slope $\tan\theta = 7.5\%$, we encountered the anomaly that for a given solid discharge there was no unique equilibrium water discharge but rather a range of values. For $\dot{n}_0 = 7.8$ beads/s we observed dynamic equilibria both for $q_w = 10.77$ and for 13.85×10^{-3} m^2/s, the corresponding experiment E7-8 was eventually conducted at an intermediate value of $q_w = 11.54 \times 10^{-3}$ m^2/s. For $\tan\theta = 7.5\%$ our experiments therefore suggested that there is no unique relationship between solid and liquid discharges as most of the empirical bed load formulas suggest.

For steeper slopes ($\tan\theta = 12.5$ and 15%) on the other hand, it was difficult to establish bed load equilibrium especially if $\dot{n}_0$ was small (see Tab. 5.3). In this case, the water depth was low ($h \to d$) and the ability of the fluid phase to set particles into motion was reduced. Particles thus accumulated either near the channel entrance or at the outlet, depending on the obstacle height (see † in Tab. 5.3). With a growing number of particle layers (up to 15) these accumulations were well ordered and formed hexagonal structures. Due to this order and since the water depth was low, these structures were eroded only occasionally, but the liftoff of one particle could entrain the erosion of dozens. The time intervals between erosion processes were irregular and covered several minutes. The available observation time was anyway utterly insufficient to embrace these phenomena correctly. Furthermore, heaps near the inlet tended to grow up to the channel entrance blocking the particle supply. We thus could not embark on the strategy to establish bed load equilibrium with a uniform bed thickness if the water depth was too low.

Due to these constraints, we were able to vary the water discharge q_w only in one order of magnitude as Tab. 5.2 shows. By the variation of

the solid supply rate, we succeeded to realize a certain number of different experiments. The main conclusions of their analysis are summarized in the concluding section of this chapter.

5.5 Conclusion

In this chapter we investigated the influence of the flow rate and the channel slope on the processes of bed load transport. A number of previous studies intend to establish empirical laws for the solid discharge as a function of water discharge and slope. Our approach focused on the physical processes of particle transport.

We ran a series of fifteen experiments with various particle injection rates and channel slopes each one under bed load equilibrium. Starting from the particle trajectories we were able to identify liftoff and settling zones, which were correlated with the local shape of the channel base. These zones expanded if the particle injection rate was raised, but they barely changed place. A higher solid discharge was furthermore characterized by an increase of the transport near the water free surface, while the particle transport in the lower part remained nearly constant.

Comparing experiments at different slopes was made difficult by the rapid variation in flow depth with slope. Furthermore, we noticed that flow variables could not be chosen arbitrarily in wide ranges, for some cases no bed load equilibrium could be obtained. Nevertheless, the data suggested a relation for the contribution of the saltating beads to the transport κ_s: For moderate slopes κ_s was above 50% depending only on the slope whereas for steep slopes it was a linear function of the water depth. Here, the rolling motion of the particles was dominant (representing ratios of up to 85%).

In previous studies on the motion of a single particle (see [Big01, ABFD03] and §1.3.3) the rolling motion was considered as a marginal mode of transport. It was suggested considering rolling simply as the intermediate state between the rest and the saltating motion of a particle. In contrast, this study on a set of particles emphasizes the importance of the rolling state of motion because: (i) for a low water depth, the space for saltation was limited, (ii) we frequently observed series of particles moving in the rolling regime keeping mutual contact. Even if the two-dimensional nature of our channel might privilege the rolling motion, we assume that this mode of transport may be neglected only in few cases. To our state of knowledge, the rolling regime is especially important for steep slopes as well as for transport near the threshold of motion, whenever the liftoff and the settling of

particles is relevant.

This result has important consequences for the development of bed load transport models. It claims the existence of two distinguished transport modes (rolling and saltation), which becomes predominant or marginal (but not negligible) depending on the flow conditions. Furthermore we found out that the regime transitions from rest via rolling to saltation (or the inverse) were of fundamental importance since they reflected the liftoff (or the settling) of particles. In consequence, we suggest that bed load transport models should incorporate a resting, a rolling, and a saltating state of motion for each sediment particle allowing regime transitions.

Chapter 6

Conclusion

In this PhD dissertation, the dynamics of particle transport in a flow was investigated experimentally. We used an inclined channel in which the particle and water supplies at the inlet were kept constant. The particles, either in motion or forming the bed, were filmed and their trajectories were calculated. The experimental setup was intended to idealize the sediment transport in steep gravel-bed rivers. Our study aimed at a better understanding of the mechanisms involved, which is needed to improve existing bed load transport models.

6.1 Summary of the main results

Solid discharge fluctuations

The first striking result of our investigation was that, over short time periods, bed load transport appeared as a very intermittent process: For our experimental conditions, the solid discharge fluctuations were as large as the mean value imposed at the upstream entrance. In a first study, we kept the channel slope and the particle injection rate constant. However, we modified the boundary conditions at the channel bottom by constraining particles to flow either over a fixed or an erodible bed (see §4), which attributed the solid discharge fluctuations to three main factors:

(a) The number of moving particles in the observation window was small, from 0 to 40 for some flow conditions. Each entering or leaving particle therefore modified the solid discharge significantly. This factor was identified by means of an experiment run with a nonerodible smooth bed (experiment A).

(b) The fluctuations of the particle velocities (x-component) entailed fluctuations of the solid discharge. This factor was identified by means of an experiment run with a nonerodible corrugated bed (experiment B).

(c) If the bed was mobile, i.e., erodible, the characteristics of transport changed remarkably: Particles were exposed to regime transitions (rest, rolling, saltation). Here, fluctuations of the solid discharge were mainly due to (i) the exchanges of particles between the moving solid phase and the bed and (ii) the collective entrainment of particles.

Factor (a) can be attributed to the experimental setup, whereas factors (b) and (c) reflect fluctuations intrinsic to the phenomena of bed load transport. Factor (c) depends on the structure of the bed: the collective entrainment of particles was most distinct if the bed was ordered (comparison of experiments C and D).

The study on different particle injection rates (see §5) showed that the absolute fluctuations increased with the solid discharge, while the relative fluctuations (ratio of fluctuations and mean solid discharge) decreased. For high solid discharges, factor (a) became less influential as the number of moving particles in the observation window increased. The channel slope had no clear effect on the solid discharge fluctuations.

Particle transport

Further noticeable results concern the water discharge needed to obtain bed load equilibrium. This variable turned out to depend on the particle arrangement in the bed: For the same solid discharge, the equilibrium water discharge needed was much higher if the bed was disordered. In other words, the solid concentration C_s (the ratio of solid and water discharge) increased with the order in the bed. As expected, C_s was also very sensitive to the channel slope: we measured values between $C_s = 1\%$ (for a slope of 7.5%) and $C_s = 12\%$ (for a slope of 15%).

It was insightful to break down the solid discharge into the contributions of rolling and saltating beads. This revealed that high solid concentrations could only be achieved when the rolling particles made up a large proportion of the particles. This result should not, however, be interpreted ignoring the effect of the water depth: For high solid concentrations, the water depth was on the order of one particle diameter and the particles were constrained to roll instead of going into saltation. In contrast to other studies [NGA94, Big01], our investigation showed that the rolling regime was relevant; for

steep slopes and ordered particle beds, it was even more substantial than saltation.

We also investigated the time correlation of the solid discharge between two vertical halves of the observation window. This yielded a propagation velocity characterizing bed load transport. This velocity corresponded to the mean velocity of the saltating beads (streamwise component). The latter in turn depended on the fluid velocity. These velocities varied only in tight ranges for the different conditions we investigated. However, the experiments run with a fixed bed (A and B) showed higher characteristic velocities.

We studied the particle liftoff and settling events in detail, as they represented the elementary processes of erosion or sedimentation. These events were reported in a space-time diagram to show that the liftoff of one particle was often spatially and temporally correlated with the liftoff of others. The same held for the settling events. We thus identified liftoff and settling zones that were linked to the local bed geometry. These zones extended if the particle injection rate was increased but they barely changed place.

Limitations of the results

In light of the results cited, it can be concluded that the goal of better understanding the mechanisms of bed load transport was entirely achieved in this PhD dissertation. It should be admitted, however, that the problem is far from being understood completely, among other things, because particle trajectories are barely predictable. This can be attributed to the influence of the disordered mobile bed. Often, particles seemed to switch randomly between the regimes of saltation, rolling, and rest without showing clear patterns.

The particle accelerations were part of the output of the flow images, a discrimination between the forces acting on the particles is, however, difficult. The liftoff of a particle, for example, could never be attributed to a single mechanism. There were always several factors involved, such as the positions of the surrounding particles or the intensity of the instantaneous water flow. To investigate the fluid-particle interaction more precisely, the measurement of the fluid velocity field would be necessary. Since the latter is three-dimensional, unsteady, and strongly affected by the moving particles, this would require a great deal of supplementary experimental effort.

6.2 Potential of the experimental facilities

The intention of our experimental facilities was to model bed load transport processes in an idealized way. We used monosized spherical particles; their motion was confined to a narrow channel and was therefore two-dimensional. As planned, the small length of the channel restricted our study to supercritical flows. Conducting the experiments, we also realized that the flow parameters we were imposing were restricted to certain ranges and could not be chosen arbitrarily.

Nevertheless, this approach was fruitful for research on sediment transport. The experimental setup made it possible to adjust solid and water discharges precisely imposing bed load equilibrium. With image-processing techniques, we were able to capture the individual motion of a set of particles with both a high temporal and spatial resolution. To meet this objective considerable work had to be devoted to the development of data-processing algorithms, but also to enhancing the experimental setup. The data obtained, the particle trajectories, were analyzed carefully to illuminate the mechanisms governing bed load transport. Notably, the characteristics of solid discharge were investigated more intensively than in any other study known to us.

Outlook

During the 5-year period since its construction, the experimental setup has evolved continuously. A first PhD dissertation was devoted to the motion of a single particle, the present one to a set of particles, seeking to meet the goal of progressively increasing the degrees of freedom of our experimental facilities.

The channel width was recently doubled to allow three-dimensional particle movement. The analysis of the images taken under these conditions will require the development of the existing detection and particle-tracking algorithms. In a further step, working with several particle sizes to study segregation processes is planned. Furthermore, a modification of the experimental protocol is foreseeable: it would be interesting to study particle transport under nonstationary conditions. This roughly outlines the possible experimental studies of a future PhD dissertation to be done at Cemagref.

It must also be emphasized that now our results are sufficiently mature to support and validate bed load transport models. The following section gives several starting points.

6.3 Impact of the results

The failure of the approach to describe bed load transport by means of a critical shear stress has reinforced the interest in a better comprehension of the mechanisms involved. Several recent models are based on alternative concepts; however, they are not free from empirical elements, because of the complexity of the problem. The bibliographic review (see §1.3) showed that some of these models are particle-based. Our experimental study especially suits complement models of this type, since we observed bed load transport at the particle scale. Two main directions can be adopted to associate our results with a numerical model:

Comparison between a numerical and an experimental simulation. It would be very instructive to carry out a bed load transport simulation with an existing model imposing conditions as close as possible to the conditions of our experiments. Whereas our study covers a range of flow conditions, several circumstances remained fixed: We used mono-sized coarse particles of a fixed diameter, the particle movement was two-dimensional, experiments were run at bed load equilibrium, the slopes were rather steep, and the water depths were low.

Any model that can be adapted to these (or most of these) conditions is suitable for a comparison with our data. It must be noted that it is presently improbable to find a model that can be fitted easily to all of the conditions cited, especially since the effect of the water free surface is considered in few approaches. The direct numerical simulation of Schmeeckle and Nelson (see §1.3.3 and [SN03]) would be suited for such a comparison. The solid discharge (profiles, time evolution) would be a particular variable of interest. Such a comparison is expected to be useful both for the transport model and for our experimental study. For the model, this could, above all validate the hypotheses. For our study, the comparison could suggest how to improve the experimental method.

Support of a new numerical model. The results also give preliminary ideas for the development of a new bed load transport model. Our study accentuated the importance of the rolling regime, regime transitions, and the arrangement in the particle bed. Starting from these results, it might be possible to develop a bed load transport model without having to calculate each particle's trajectory. The probabilistic approaches of Markov chains (see [ABFD03]) or the theory on cellular automata seem to be promising.

This points out that it would be enriching to orient our efforts toward the modeling of bed load transport without neglecting the experimental part. The experimental study of this PhD dissertation provided a base for these intentions.

Appendix A

Theoretical approach for experiment B[1]

Using simple assumptions makes it possible to obtain the probability density function $P_{\dot{n}}$ of the flow rate $\dot{n}$. These assumptions are the following:

(a) The number of particles is distributed according to a Poisson distribution, that is, we have:

$$P_N(N_i) = \frac{e^{-\mu}\mu^{N_i}}{N_i!},$$

where μ is the average number of particles contained in the observation window: $\mu = \mathbb{E}[N_i]$. The Poisson distribution is often used to describe processes characterized by a number of events occurring during a given time interval.

(b) The particle velocity is Maxwellian, that is, its variations around the mean velocity are normally distributed:

$$P_u(u_i) = \frac{1}{\sqrt{2\pi}\sigma_u} \exp\left[-\frac{(u_i - \bar{u})^2}{2\sigma_u^2}\right],$$

where $\bar{u}$ is the mean velocity and σ_u^2 the velocity variance. The choice of this distribution was motivated by the kinetic theory.

(c) The velocity probability is independent of (i) the particle number as well as (ii) the velocity of close particles because flow is dilute.

[1] See §4.4.2

We introduce $U = \sum_{i=1}^{N_i} u_i$ the sum of particle velocities (streamwise components) for the N_i particles included in the window. Since $\dot{n} = U/L$, the pdf P_U of U is related to that of $\dot{n}$ by: $P_{\dot{n}} = LP_v(L\dot{n})$. Thus computing P_U is tantamount to computing $P_{\dot{n}}$. The probability P_U is obtained by summing the elementary probabilities of observing k particles whose velocity sum equals U, that is,

$$P_U = \sum_{k=1}^{\infty} \frac{e^{-\mu}\mu^k}{k!} P_k(U),$$

where P_k denotes the probability of observing the velocity sum (for k particles) equal to U

$$P_k = \int_{-\infty}^{\infty} du_1 du_2 \cdots du_k P_u(u_1)P_u(u_2)\cdots P_u(u_k)\delta[U - (u_1 + u_2 + \cdots u_k)]$$

$$P_k = \int_{-\infty}^{\infty} du_1 du_2 \cdots du_{k-1} P_u(u_1)P_u(u_2)\cdots P_u(U - (u_1 + u_2 + \cdots u_{k-1}))$$

Taking the Fourier transform of P_k leads to:

$$\mathcal{F}[P_k](\omega) = \left(\mathcal{F}[P_u](\omega)\right)^k$$

where $\mathcal{F}[P_k](\omega) = \int e^{i\omega U} P_k(U)dU$. The Fourier transform can be expanded into an infinite series:

$$\mathcal{F}[P_k](\omega) = \sum_{j=0}^{\infty} \frac{c_j^{(P_k)}}{j!} (i\omega)^n,$$

where $c_j^{(P_k)} = (-1)^j (d^j \ln \mathcal{F}[P_k]/d\omega^j)_{\omega=0}$ are called the cumulants. For a normal distribution, the two first cumulants correspond to the mean and variance while the cumulants of order larger than 2 are zero. Here we find that:

$$c_j^{(P_k)} = 2c_j^{(P_u)} \text{ for } j = 1, 2;$$

$$c_j^{(P_k)} = 0 \text{ for } j \geq 3.$$

Finally we deduce that P_k is a normal distribution of mean $k\bar{u}$ and variance $k\sigma_u^2$: $P_k = \mathcal{N}\left[k\bar{u},\, \sqrt{k}\sigma_u\right]$. One finally obtains:

$$P_{\dot{n}} = \sum_{k=1}^{\infty} \frac{e^{-\mu}\mu^k}{k!\sqrt{2\pi k}} \frac{L}{\sigma_u} \exp\left[-\frac{(L\dot{n} - k\bar{u})^2}{2k\sigma_u^2}\right]$$

Expressing this result as

$$P_{\dot{n}} = \sum_{k=1}^{\infty} \frac{e^{-\mu}\mu^k}{k!} \mathcal{N}\left[\frac{k\bar{u}}{L},\ \frac{\sqrt{k}\sigma_u}{L}\right],$$

it is straightforward to deduce the mean and variance of $P_{\dot{n}}$:

$$\mathbb{E}[P_{\dot{n}}] = \frac{\mu\bar{u}}{L},$$

$$\mathrm{Var}[P_{\dot{n}}] = \frac{\mu\sigma_u^2}{L^2}.$$

Appendix B

Water and bed surfaces

The objective of this section is to analyze the features of the water free surface, the bed surface elevation and their interaction more comprehensively. For this purpose we first show once again the images of the water free surface w_f (see Fig. B.1) and the bed surface b_s (see Fig. B.2) taken over from §3. The experimental conditions of the experiment are described in chapter §4 (see experiment D).

We calculated the probability density functions (pdf) of w_f and b_s for the whole data sequence ($\Delta t = 61.9$ s, see Fig. B.3). In other words, these diagrams are the histograms of the images shown reduced in Fig. B.1 and B.2. The pdf of w_f was narrow and nearly Gaussian ($\bar{w}_f = 33.1$ mm, $\sigma_{wf} = 1.9$ mm) which indicates that small positive and negative perturbations of the elevation occurred with an even frequency. In contrast, the pdf of b_s ($\bar{b}_s = 21.4$ mm, $\sigma_{bs} = 2.2$ mm) had a higher maximum and wider tails. While most of the time the bed line was at a level of 20–23 mm, occasionally it raised or fell considerably (on the order of one particle diameter). The former process can be attributed to particles that reposed momentarily on the quasiimmobile bed, the latter to sporadic rearrangements in the bed. The background of Fig. B.3 was obtained by superimposing all the images of the filmed sequence.

Figure B.1 reveals furthermore a characteristic propagation velocity of the water surface waves. This can be made evident by the autocorrelation diagram (see Fig. B.4) obtained with the Wima software (see §3.1). We calculated the spatiotemporal autocorrelation on a squared detail of the image of w_f ($\Delta x = 200$ mm or 512 pixels, $\Delta t = 4$ s or 512 pixels) by means of the fast Fourier transformation. Each pixel of this image represents the correlation coefficient of the water line image with a copy of itself that was

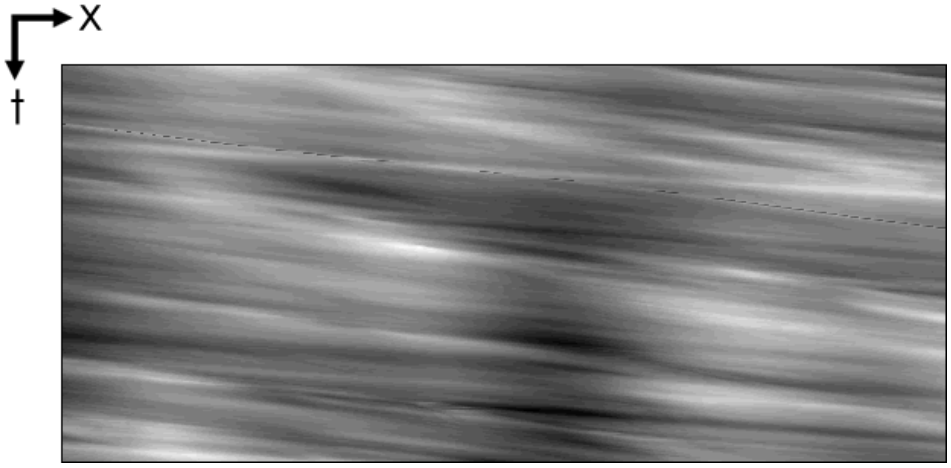

Fig. B.1: Elevation of the water free surface $w_f(x,t)$ as a gray scale image. Image dimensions: $\Delta x = 220$ mm, $\Delta t = 2$ s. White: $w_f(x,t) = +5.7$ mm, black: $w_f(x,t) = -5.5$ mm versus the mean value. For experimental conditions, see Tab. 4.2, experiment D.

Fig. B.2: Elevation of the bed surface $b_s(x,t)$ as a gray scale image. Image dimensions: $\Delta x = 220$ mm, $\Delta t = 2$ s. White: $w_f(x,t) = +15.5$ mm, black: $w_f(x,t) = -7.3$ mm versus the mean value. For experimental conditions, see Tab. 4.2, experiment D.

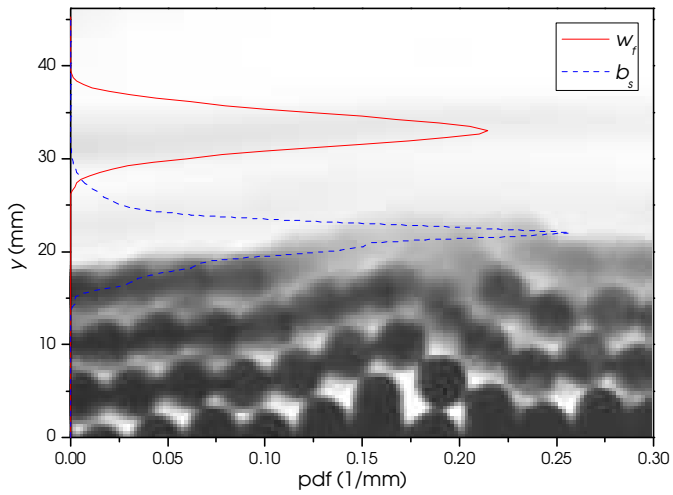

Fig. B.3: Probability density functions (pdf) of the water free surface w_f and the bed surface elevation b_s. Experiment D.

displaced in space and time. The highest correlation coefficient can be found in the image center for small Δx and Δt. The zones of equal correlation can be characterized by an elliptic shape. The inclination of the main axis of these ellipses reflect the characteristic propagation velocity of the surface waves yielding $c = \Delta x/\Delta t \approx 0.41$ m/s. For larger Δx and Δt the correlation coefficient decreases and the elliptic shape degenerates.

Similarly, we calculated the autocorrelation diagram of the bed elevation (see Fig. B.5). Since the elliptic shape of the zones of equal correlation is less pronounced, it is not possible to define a single characteristic velocity. The zones of equal correlation indicate characteristic velocities in the range 0.004 m/s $< c < 0.18$ m/s. An explication might be the following: Sections of the bed stayed stationary for long time intervals, whereas the occasional reorganization of the bed (via liftoff or settling of particles) implied much higher velocities.

Figure B.6 shows the intercorrelation function of $w_f(x,t)$ and $b_s(x,t)$. For small Δx and Δt, the correlation coefficient is approximately 0.5, which indicates that water and bed elevation were strongly coupled.

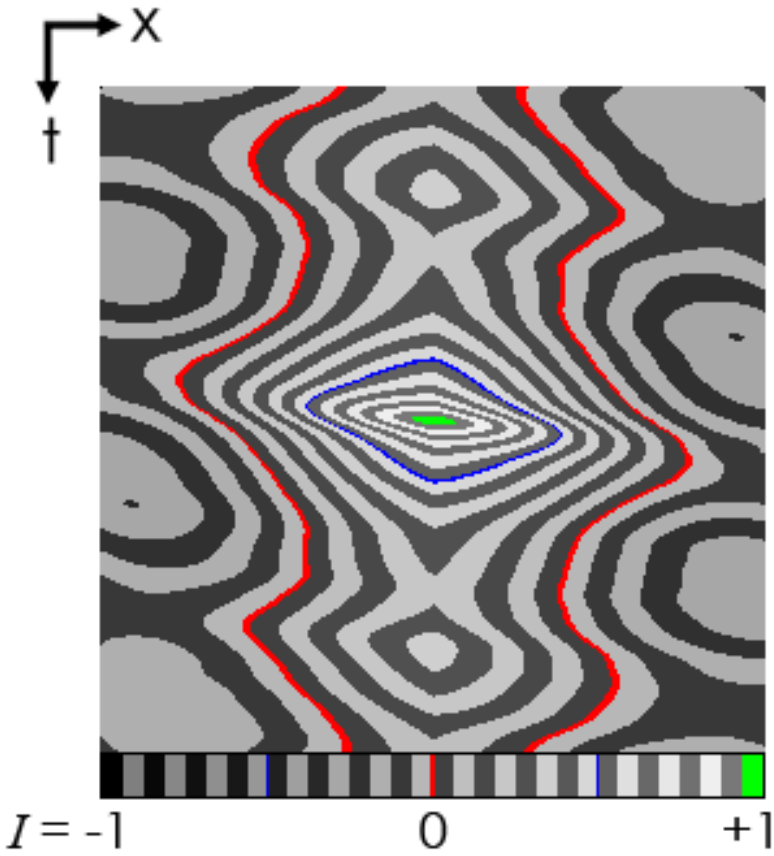

Fig. B.4: Spatiotemporal autocorrelation diagram for the water free surface w_f. Image dimensions: $\Delta x = 100$ mm, $\Delta t = 2$ s. Correlation coefficient: $-0.31 \leq I \leq +1$. Experiment D.

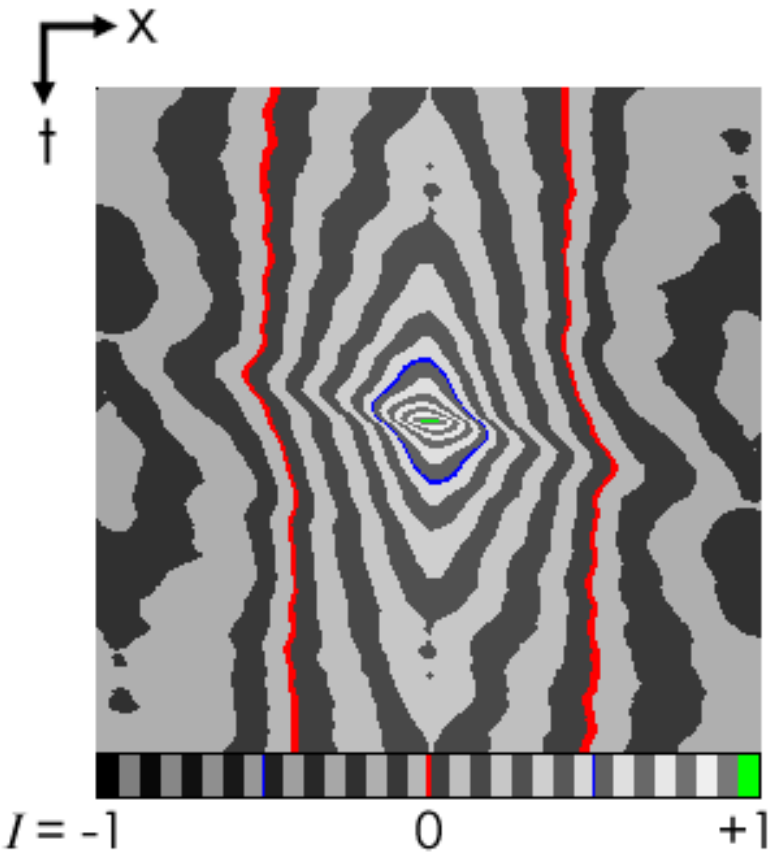

Fig. B.5: Spatiotemporal autocorrelation diagram for the bed surface elevation b_s. Image dimensions: $\Delta x = 100$ mm, $\Delta t = 2$ s. Correlation coefficient: $-0.27 \leq I \leq +1$. Experiment D.

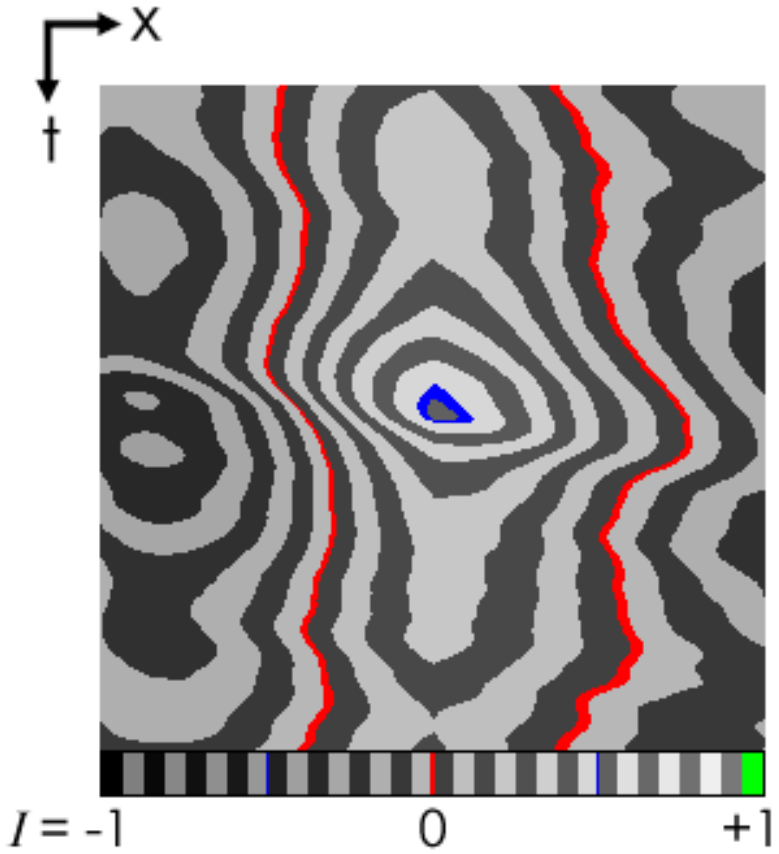

Fig. B.6: Spatiotemporal intercorrelation diagram between the water free surface w_f and the bed surface elevation b_s. Image dimensions: $\Delta x = 100$ mm, $\Delta t = 2$ s. Correlation coefficient: $-0.39 \leq I \leq +0.52$. Experiment D.

Appendix C

Solid discharge

C.1 Fourier transform

For a further analysis of the solid discharge $\dot{n}$ we calculated its Fourier transform (for experiment D, see Fig. C.1). The two most distinct peaks could both be identified as perturbing frequencies due to imperfections of the experimental facility: the frequency of the lamp ($f = 30.7$ Hz) and the vibration frequency of the vibrator used for the particle supply ($f = 46.4$ Hz).

The deficiency of the illumination (see §2.6), a periodic variation in the intensity, was clearly visible in the image sequences. The image luminosity affected slightly the particle detection, since it could happen that a poorly illuminated particle was not detected. This is why the frequency of the lamp was still perceivable in the spectrum of the solid discharge. However, we estimate the influence of this imperfection on our observation of bed load transport phenomena as weak. The simplest remedy would be the replacement of the present lamp by one of a constant light emission.

The second perturbing frequency had a higher amplitude and was thus more worrying. The vibration of the bead reservoir was necessary to keep the beads running towards the injection wheel (see §2.4). As the bead supply unit was fixed on the channel its vibrations were transmitted to the channel and the filmed beads. The x-component of these vibrations reflected in a periodic fluctuation of the solid discharge. To dispose of this deficiency completely it would be necessary to uncouple the supply system from the channel. The efforts in doing this seemed more important than the benefits, given that the solid supply system was the most delicate component of the experimental setup. However, we strived for a vibration amplitude as low

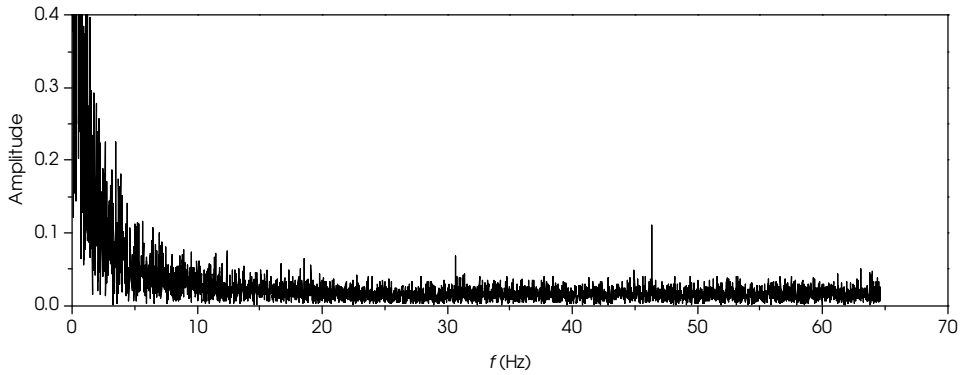

Fig. C.1: Amplitude of the Fourier transform of the solid discharge. Experiment D.

as possible, by reducing the eccentric mass of the vibrator.

The Fourier transform revealed thus two parasitic frequencies due to imperfections of the experimental setup which could not be suppressed completely. However, the cited peaks were less than four times higher than the background noise of the spectrum. Finally, the phenomena of bed load transport showed characteristic times of 0.1–1 s (see Fig. 4.6) and thus frequencies of 1–10 Hz. In this range, the Fourier spectrum showed no pronounced frequency. Notably the bead injection rate (here $f = 8$ Hz) and the rotation frequency of the bead transport wheel (for experiment D: 12 hollows, $f = 8$ Hz$/12 = 0.67$ Hz) were not visible.

In short, the Fourier transform did not give any insights into problems of bed load transport but it contributed to the better understanding of the experimental setup.

C.2 Alternative definitions

In §4.4 we mentioned the problems to define the solid discharge of a discrete particle flux. The volume averaged definition of $\dot{n}(t)$ in eq. (4.3) is only one possible definition. More generally the x- and y-motion of all the particles with time t can be considered. The trajectories form a set of functions: $\mathbf{x}_i(t) = (x_i(t), y_i(t))$, where i is the particle number. Figure C.2 shows that already the representation of two trajectories in the (x, y, t) space is complex. Indeed, we were studying on the order of 1000 trajectories in a resolution of 580, 120, and 8000 data points in x, y, and t respectively. For

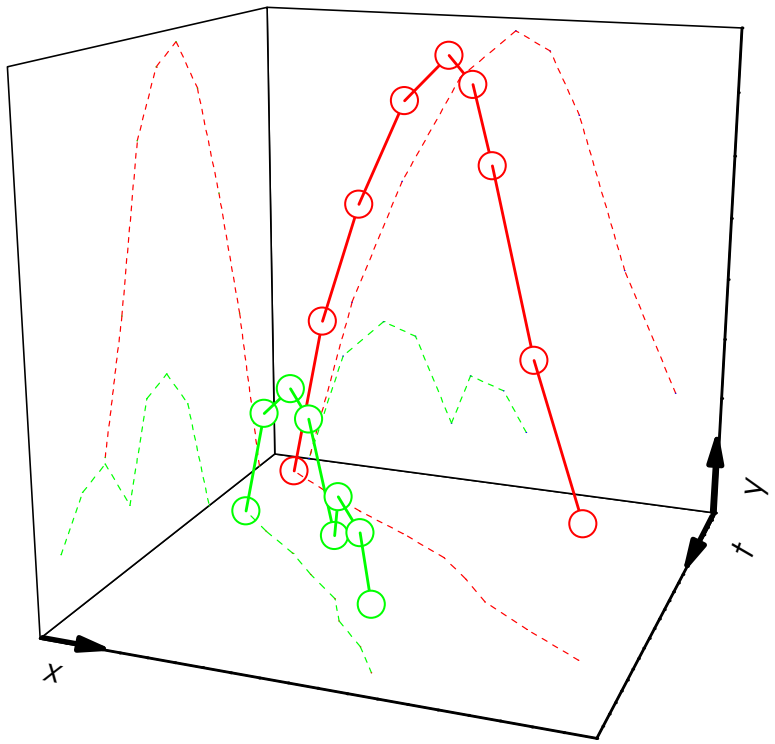

Fig. C.2: Sketch of the trajectories in the (x, y, t) space.

a more convenient representation, the number of independent variables had to be reduced. This can be done by taking the average over x, y, or t. In the sketch, the averaging corresponds to the projection of the trajectories on the (y, t), the (x, t), or the (x, y)-plane, respectively. Further simplicity can be obtained by a second averaging, leaving the intensity of the solid discharge as a function of a single variable. Several diagrams of the solid discharge have already been presented: Figure 5.12 shows the superimposition of the trajectories on the (x, y)-plane and Fig. 4.14 is the projection of the particle motion on the (x, t)-plane.

We worked with an x- and y-averaged definition of the solid discharge (see eq. (4.3)). It is furthermore possible to define the local solid discharge $\dot{n}_C(t)$, i.e. for a constant x. According to this definition the particles passing at a fixed x-position are "counted" and these events are plotted as a function of time. Figure C.3(a) shows that $\dot{n}_C(t)$ is a signal consisting of impulses of uniform duration and amplitude. Each impulse at the time t_i represents

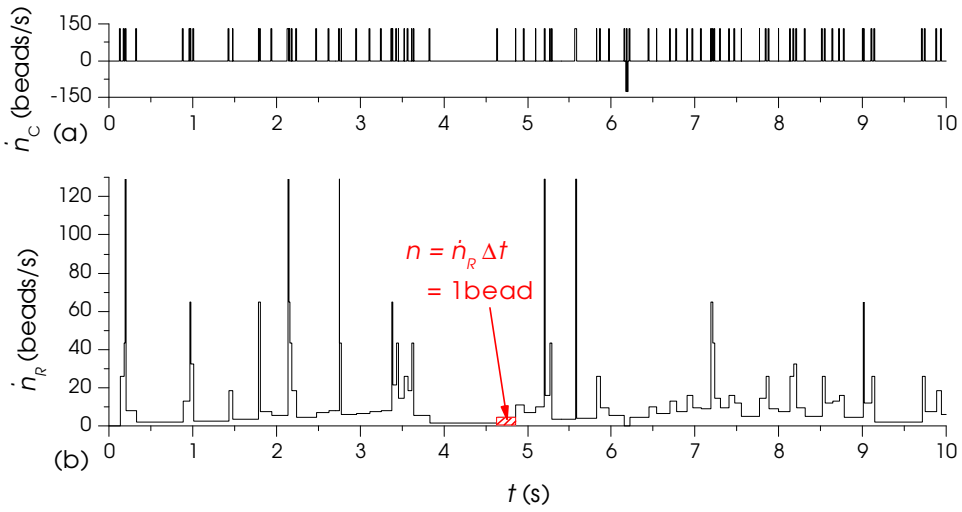

Fig. C.3: Two additional definitions of the solid discharge: $\dot{n}_C(t)$ and $\dot{n}_R(t)$ calculated for $x = 124$ mm.

a particle. However, it is difficult to treat such a signal with usual analysis methods, that is why we transformed it into the rectangular shaped function $\dot{n}_R(t)$. An example is shown in Fig. C.3(b), $\dot{n}_R(t)$ is defined by:

$$\dot{n}_R(t_i \leqq t < t_{i+1}) = 1 \text{ bead}/(t_{i+1} - t_i), \tag{C.1}$$

where t_i are the instants of the impulses of $\dot{n}_C(t)$. By this definition, for each time interval between the passing of two beads ($\Delta t = t_{i+1} - t_i$), a constant value (1 bead/Δt) was attributed to $\dot{n}_R(t)$. Thus, the area under the function corresponded to 1 bead for each section. $\dot{n}_R(t)$ was defined to be 0 on the intervals before and after $\dot{n}_C(t) < 0$, i.e. if a bead was going upstream. In the case of two beads passing at x at the same time step, one of them was considered to pass the following time step, introducing a slight error. By this, the instantaneous solid discharge was limited to 1 bead/frame or 129.2 beads/s, which is considerably higher than the injection rates we studied.

The solid discharge $\dot{n}_R(t)$ can be analyzed by means of correlation functions. We first calculated $\dot{n}_R(t)$ for $x_1 = 12$ mm, $x_2 = 124$ mm, and $x_3 = 236$ mm and normalized the signals by the equation: $\tilde{\dot{n}}_R(t) = (\dot{n}_R(t) - \overline{\dot{n}}_R)/\sigma_{\dot{n}R}$, as in §4.4.1. For each x-position we calculated the autocorrelation function (see Fig. C.4), which corresponds to curve D in Fig. 4.3. Because we were working here with a local, non-averaged definition, the functions

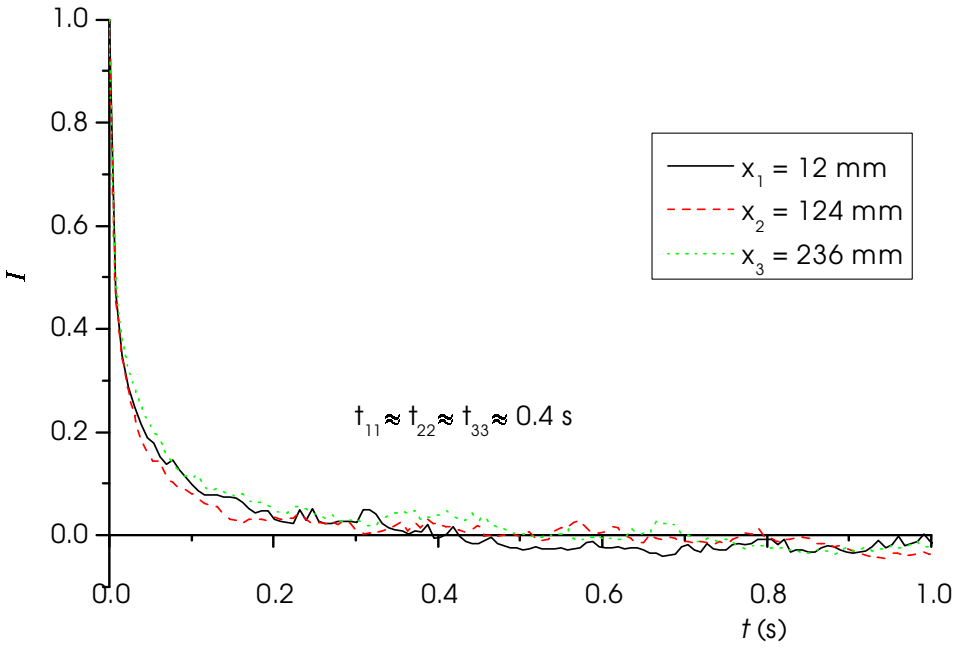

Fig. C.4: Normalized autocorrelation functions of the solid discharge $\dot{n}_R(t)$ computed for three x-positions.

were less smooth and fell off to 0 more rapidly than that in §4. The physical interpretation of the autocorrelation function for $\dot{n}_R(t)$ is more palpable here: It describes the mean temporal duration of high or low phases of the solid discharge at a fixed section x. The three curves of Fig. C.4 differed only slightly, which indicates that the time-evolution of the solid discharge exhibited the same patterns at any x-position. Each of them revealed a characteristic time of approximatively 0.4 s. The physical meaning of Fig. 4.3 is less clear as it reflects the time correlation of the complete particle movement in the observation window.

We calculated furthermore the intercorrelation functions between the positions x_2-x_1, x_3-x_2 (both of them corresponding to curve D in Fig. 4.6), and $x_3 - x_1$. The correlation amplitudes are considerably lower than in §4, which again can be attributed to the fact that the definition of $\dot{n}_R(t)$ is local which implies more fluctuations. More striking is the strong difference between the curves x_2-x_1 and x_3-x_2 which were calculated on two adjacent zones of the same length, especially the different positions of the maxima. Particles took an average time of $t_{12} = 0.379$ s to traverse the first window

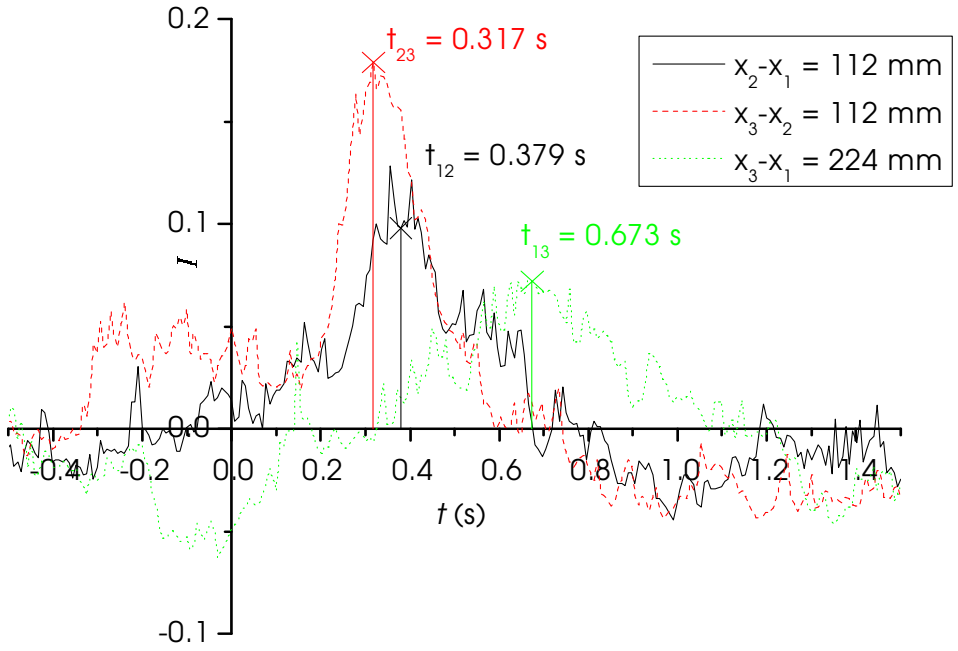

Fig. C.5: Normalized intercorrelation functions of the solid discharge $\dot{n}_R(t)$ computed for three x-intervals.

half but only $t_{23} = 0.317$ s for the second one, which was nearly 20% less. The characteristic times were nevertheless of the same order as $t_D = 0.33$ s, obtained in §4.4.4. The characteristic time for the complete window length was roughly the double ($t_{13} = 0.673$ s).

In short we found, that the autocorrelation functions at different x-positions differed very little, while the intercorrelation functions taken on adjacent zones of equal length were quite different.

Appendix D

Résumés des chapitres en français[1]

Introduction

Les crues des rivières de montagne se distinguent par leur formation soudaine et un transport solide important [Bes96]. Un exemple est la crue de la Saltine à Brigue (Suisse) en 1993. A la suite de l'obstruction par un dépôt solide d'un pont au centre ville, la Saltine quitta subitement son lit, inonda la vieille ville. L'écoulement laissa sur son passage un dépôt massif de sédiment et causa la mort de deux personnes [BAJ94]. C'est un exemple qui a amené des ingénieurs à se consacrer au transport solide, même si la prédiction de l'apparition de tels désastres est souvent impossible.

En outre, de nombreux cours d'eau doivent être gérés pour assurer la coexistence de l'écosystème et de l'infrastructure humaine. Dans ce contexte, le transport de sédiments est souvent important puisqu'il influence directement la morphologie des cours d'eau. En France par exemple, le lit de la Drôme s'est enfonçé considérablement, en partie à cause de l'extraction de granulats. Comme l'incision du lit met en danger l'effet protecteur des digues, il faut développer des stratégies pour recharger la rivière en sédiment.

Pour cette raison, les ingénieurs accordent beaucoup d'attention au calcul de transport solide en fonction du débit liquide, les résultat ne sont pas complètement satisfaisants. En particulier à forte pente (voir le torrent de Fig. 1) la concentration solide peut atteindre 20 % et la granulométrie du sédiment est très étendue (du sable aux blocs).

[1] Traduction complète de l'introduction et de la conclusion ; traduction des résumés des chapitres 1-5.

Ceci explique la nécessité d'une meilleure compréhension du transport solide par charriage (le transport de sédiment près du lit de la rivière). A cet égard, des chercheurs suivent des approches différentes. A priori, les mesures de terrain sont le plus proche de la réalité. Néanmoins, peu des nombreux paramètres impliqués peuvent être mesurés. Ces mesures sont en plus rarement reproductibles, car elles dépendent des conditions de terrain. Les mesures de terrain ne donnent alors qu'une vue limitée des mécanismes du transport par charriage. Des expériences en laboratoire peuvent combler ce manque : le phénomène est simulé sous des conditions maîtrisées. Le nombre de paramètres de contrôle peut être réduit et il est beaucoup plus facile de faire des mesures précises et complètes.

L'intérêt des données de terrain mais aussi de laboratoire est le support du développement et de l'amélioration de modèles. Ces modèles sont ensuite utilisés pour la prédiction des phénomènes d'écoulement pour des conditions données. La plupart des problèmes concernant les écoulement d'eau à surface libre ont été résolus depuis longtemps pour des régimes peu éloignés du régime permanent. Le transport solide est pourtant toujours difficile à modéliser puisqu'une phase liquide et une phase solide sont impliquées. L'approche des problèmes liés au seuil de mouvement et à la présence des formes du lit est particulièrement complexe. Jusqu'à présent, les modélisateurs doivent faire appel à des approches empiriques pour déterminer plusieurs paramètres. L'importance qu'il y a à valider et à vérifier des modèles de transport avec des données de laboratoire et de terrain a récemment été soulignée par le Task Committee on computational modeling of sediment transport processes de l'American Society of Civil Engineers [ASC04].

Notre contribution à ce sujet est la suivante : réduire le transport solide par charriage à ses éléments essentiels, ce qui nous a incité à utiliser un canal modèle à deux dimensions. Dans une première thèse de doctorat [Big01], le mouvement d'une particule individuelle dans un écoulement d'eau sur un fond rugueux a été étudié. Pour la présente étude, nous avons développé un système de distribution de billes de verre sphériques pour alimenter le canal en continu en sédiment. Le dispositif expérimental permet d'imposer les conditions expérimentales d'une manière précise, notamment l'alimentation en eau et en particules. En conséquence, nous sommes capable de faire des mesures sophistiquées par traitement d'images et d'analyser les résultats d'un point de vue physique. Une attention particulière a été accordée au lit de particules mobile résultant de l'échange incessant entre les particules en mouvement et le lit. Nous verrons par exemple que des particules sont mises en mouvement et se déposent fréquemment en des zones précises,

déterminées par la structure du lit. Cet approche microstructurelle a donc pour objectif l'étude fine des mécanismes de transport. L'objectif en filigrane est d'utiliser les résultats pour avancer le développement des modèles numériques de transport solide par charriage.

Plan du mémoire de thèse

Ce mémoire de thèse est structuré comme suit : dans le premier chapitre nous décrivons le problème étudié et nous discutons les travaux les plus importants faits dans le domaine jusqu'à présent. Le chapitre 2 introduit notre approche par une présentation du dispositif expérimental, le canal, les systèmes d'alimentation en eau et en particules, ainsi que l'acquisition d'images. Les procédures expérimentales du transport solide par charriage à l'équilibre sont détaillées. Les images de l'écoulement ont ensuite été traitées par deux algorithmes de détection pour obtenir la surface libre et les positions des particules. Les trajectoires ont été calculées à l'aide d'un algorithme de suivi de particules. Ces algorithmes développés pendent cette thèse sont décrits dans le chapitre 3.

Les résultats expérimentaux sont présentés dans les deux chapitres suivants : une première étude s'intéresse aux origines des fluctuations du débit solide (chapitre 4). A cet effet, nous avons effectué une série de quatre expériences avec un nombre croissant de processus impliqués. Dans le chapitre 5 nous examinons l'influence du débit et de la pente du canal sur le transport par charriage. Nous verrons que notamment la pente a une influence importante sur les caractéristiques du transport. L'apport de ces résultats est finalement discuté dans la perspective des travaux futurs.

D.1 Approches en transport solide par charriage

La présente étude se focalise sur le transport solide dans les torrents. Ces derniers sont caractérisés par de fortes pentes, des concentrations de sédiment parfois élevées avec entraînement de particules grossières. Nous étudions le transport par charriage, les particules roulent ou effectuent des sauts sur le lit lui-même composé de particules. Comme une phase solide ainsi qu'une phase liquide sont présentes à l'échelle macroscopique, l'approche physique de ce problème est difficile. Il est courant de considérer quatre variables (débit solide, débit liquide, cote du lit et hauteur d'eau) en fonction de la coordonnée longitudinale et du temps. Outre des équations de bilan de masse de chaque phase et de la quantité de mouvement pour le fluide, une

quatrième relation manque pour compléter le jeu d'équations. Le plus souvent, les ingénieurs font appel à des approches empiriques qui sont pour la plupart basées sur l'hypothèse de Bagnold. D'après cette hypothèse, le débit solide est relié à la contrainte de cisaillement exercée sur le lit par le fluide, si cette dernière excède une valeur seuil. L'échec de l'hypothèse de Bagnold pour certains problèmes a renouvelé l'intérêt pour des approches alternatives. Celles-ci incluent la description théorique du système fluide-particules à l'aide de la théorie cinétique et la simulation numérique des trajectoires de particules.

D.2 Dispositif et techniques expérimentaux

Le dispositif est composé d'un canal étroit aux parois en verre d'une longueur de 2 m. La pente a été réglée dans la gamme de 7,5 % à 15 %. Le canal est alimenté en continu en eau et en billes de verre sphériques de diamètre 6 mm. La largeur du canal n'est que légèrement supérieure à ce diamètre, si bien que le mouvement des particules est quasiment bidimensionnel. Un obstacle à la sortie du canal permet aux particules de se déposer sur le fond rugueux du canal. Nous avons étudié en priorité le cas de l'équilibre de transport, c.-à-d. sans érosion ni dépôt de particules sur des intervalles de temps suffisamment longs. Les écoulements ont été filmés par le côté avec une caméra rapide. Ceci nous a permis d'acquérir le mouvement d'un ensemble de particules (une centaine d'individus) pendant environ une minute.

D.3 Traitement d'images et de données[2]

Les images ont été analysées en utilisant des algorithmes qui combinent des opérations de traitement d'images du logiciel Wima. La surface libre d'eau a été détectée grâce à sa forme allongée ; les portions manquantes ont été interpolées et extrapolées. Les positions des centres de masse des billes ont été détectées en comparant des images filmées avec l'image d'une bille modèle. Les maxima de corrélation ont été calculés pour obtenir les positions des billes. L'incertitude du résultat pour la ligne d'eau et les positions des particules se limite à 1 pixel ou 0,4 mm. Nous avons développé un algorithme de suivi de particules pour calculer la trajectoire de chacune des billes filmées pas à pas. L'état de mouvement d'une particule a été défini en considérant que chaque bille était dans un régime d'arrêt, de roulement ou de saltation. Nous avons défini le profil de la surface du lit par la ligne

[2]Publication soumise à *Experiments in Fluids* [BFD$^+$].

brisée qui joint les points les plus hauts des billes en arrêt ou en roulement. Ceci a permis de calculer la hauteur d'eau.

D.4 Fluctuations du débit solide[3]

Nous avons analysé les origines des fluctuations du débit solide lorsqu'on fait varier les conditions d'écoulement. Deux expériences ont été réalisées avec un fond fixe (lisse ou ondulé) et deux autres avec un lit mobile (avec des couches de particules jointives susceptibles d'être mises en mouvement par l'écoulement). Dans ce dernier cas, deux arrangements de particules ont été testés. Nous avons trouvé que, dans une large mesure, les fluctuations reflétaient la taille finie de la fenêtre d'observation. Pour des lits fixes, l'échelle temporelle caractéristique des fluctuations et leur distribution de probabilité peuvent être prédéterminées si l'on évalue la vitesse moyenne d'une seule particule et sa fluctuation. Les fluctuations du débit solide augmentent si le lit est mobile car (i) la phase solide en mouvement et le lit stationnaire échangent des particules et (ii) entraînement collectif des particules se manifeste.

D.5 Influence du débit et de la pente[4]

L'influence du débit et de la pente sur les processus du transport solide par charriage a été étudié. En premier lieu, nous avons varié le débit solide, en adaptant le débit d'eau pour établir l'équilibre de transport. Une augmentation du débit solide accroît surtout le transport proche de la surface libre, tandis que le transport de particules dans la zone inférieure reste quasiment constant. En outre, nous avons identifié des zones de départ et de dépôt des particules, corrélées avec la forme locale du fond de canal. Ces zones s'élargissent pour une augmentation du taux d'injection de particules, mais elles ne changent pratiquement pas de position. Pour une augmentation de la pente du canal, le rapport des particules transportées dans le régime de saltation diminue. Pour des fortes pentes, la hauteur d'eau est réduite à environ un diamètre de particule, ce qui incite les particules à rester en contact mutuel et à se déplacer dans le régime de roulement. Pour des hauteurs d'eau encore plus faibles, il est impossible d'établir un équilibre de transport.

[3] Basé sur T. Böhm, C. Ancey, P. Frey, J.L. Reboud, and C. Ducottet, *Physical Review E* **69** 061307 (2004) ; voir [BAF+04].

[4] Une publication est en préparation.

D.6 Conclusion

Dans cette thèse la dynamique du transport de particules dans un écoulement a été étudiée expérimentalement. Nous avons utilisé un canal incliné avec une alimentation constante en particules et en eau. Les particules, en mouvement ou constituant le lit, ont été filmées et leurs trajectoires ont été calculées. L'objectif de ce dispositif expérimental était de modéliser d'une manière idéalisée le transport solide dans les rivières à lit de gravier à forte pente. Notre étude vise une meilleure compréhension des mécanismes impliqués, ce qui est nécessaire pour améliorer les modèles existants du transport solide par charriage.

D.6.1 Résumé des résultats principaux

Fluctuations du débit solide

Le premier résultat frappant de notre étude est que, sur des périodes de temps courtes, le transport par charriage apparaît comme un processus très intermittent : pour nos conditions expérimentales, les fluctuations du débit solide sont aussi importantes que la valeur moyenne imposée à l'entrée du canal. Lors d'une première étude nous avons gardé la pente du canal et le taux d'injection de particules constants. Nous avons cependant modifié les conditions aux limites du fond du canal en forçant les particules à couler sur un lit soit fixe, soit érodable (voir § D.4). Ceci nous a permis d'attribuer les fluctuations du débit solide à trois processus principaux :

(a) Le nombre de particules en mouvement dans la fenêtre d'observation est faible, de 0 à 40 pour certaines conditions d'écoulement. Ainsi, chaque bille qui entre ou sort modifie le débit solide d'une manière significative. Ce processus à été identifié grâce à une expérience réalisée avec un lit lisse et non-érodable (expérience A).

(b) Les fluctuations des vitesses des particules (composante x) engendrent des fluctuations du débit solide. Ce processus a été identifié grâce a une expérience effectuée avec un lit ondulé et non-érodable (expérience B).

(c) Pour un lit mobile, érodable, les changements des caractéristiques de transport sont remarquables : les particules sont soumises à des transitions de régime (arrêt, roulement, saltation). Dans ce cas, les fluctuations du débit solide sont principalement dues à (i) des échanges de par-

ticules entre la phase solide en mouvement et le lit et (ii) l'entraînement collectif de particules.

Le processus (a) est dû au dispositif expérimental, alors que les processus (b) et (c) représentent des fluctuations intrinsèques au phénomène du transport solide par charriage. Le processus (c) dépend de la structure du lit. L'entraînement collectif des particules est autant plus important que le lit est plus ordonné (comparaison des expériences C et D).

Lorsque le débit solide en entrée augmente, la valeur absolue des fluctuations augmente, tandis que les fluctuations relatives (rapport entre les fluctuations et le débit solide moyen) diminuent. Pour des débits solides élevés, le processus (a) perd de l'influence car le nombre de particules dans la fenêtre d'observation augmente. La pente du canal n'a pas d'effet clair sur les fluctuations du débit solide.

Transport des particules

D'autres résultats remarquables concerne le débit d'eau nécessaire à obtenir l'équilibre de transport. Cette variable s'est avérée dépendre de l'arrangement des particules dans le lit : pour le même débit solide, le débit liquide nécessaire à l'équilibre est beaucoup plus élevé, si le lit est désordonné. Autrement dit, la concentration solide C_s (le rapport entre le débit solide et liquide) augmente avec l'ordre dans le lit. Comme attendu, C_s est en outre très sensible à la pente du canal : nous avons mesuré des valeurs entre $C_s = 1$ % (pour une pente de 7,5 %) et $C_s = 12$ % (pour une pente de 15 %).

Il a été révélateur d'étudier les contributions des billes en roulement et en saltation. Les concentrations solides élevées ont seulement été atteintes lorsqu'il y avait une contribution importante des particules en roulement. Cependant, ce résultat ne doit pas être interprété en ignorant l'effet de la hauteur d'eau : pour des concentrations solides importantes, la hauteur d'eau était de l'ordre d'un diamètre de particule et les particules étaient forcées à rouler au lieu de passer en saltation. Par opposition à d'autres études [NGA94, Big01], nos recherches ont montré que le régime de roulement était crucial. Pour des fortes pentes et des lits ordonnées de particules, il était même plus important que la saltation.

Nous avons également examiné la corrélation temporelle du débit solide entre les deux moitiés verticales de la fenêtre d'observation. Il est mis en évidence une vitesse de propagation caractérisant le transport solide par charriage. Cette vitesse s'est révélée correspondre à la vitesse moyenne des particules en saltation (composante dans le sens de l'écoulement). Cette dernière dépend de la vitesse du fluide. La plage de variation de ces vitesses

était très étroite pour les différentes conditions étudiées. En revanche, les expériences réalisées avec un lit fixe (A et B) ont montré des vitesses caractéristiques plus élevées.

Nous avons étudié en détail les événements correspondant au départ et au dépôt des particules puisqu'ils représentent les processus élémentaires de l'érosion et de la sédimentation. Ces événements ont été reportés dans un diagramme spatio-temporel pour montrer que le départ d'une particule était souvent corrélé (en espace et en temps) au départ d'autres. La même observation a été faite pour les événements de dépôt. Ainsi, nous avons identifié des zones de départ et de dépôt qui se sont révélées être liées à la géométrie locale du lit. Ces zones se sont élargies pour un taux d'injection de particules plus élevé, mais elles n'ont pratiquement pas changé de position.

Limites des résultats

Devant les résultats cités on peut conclure que l'objectif d'obtenir une meilleure connaissance des mécanismes du transport solide par charriage a été atteint au cours de cette thèse de doctorat. Pourtant, il faut admettre que le problème est loin d'être compris complètement, entre autres parce que les trajectoires des particules ne sont guère prévisibles. Ceci peut être attribué à l'influence du lit mobile désordonné. Souvent, les particules semblent changer entre les régimes de saltation, de roulement et d'arrêt d'une manière aléatoire sans montrer un type de comportement clair.

Les accélérations des particules font partie des résultats des images de l'écoulement, mais une discrimination entre les forces exercées sur les particules est difficile. Par exemple, le départ d'une particule n'a jamais pu être attribué à un mécanisme en particulier. Il y avait toujours plusieurs facteurs impliqués, comme la position des particules au voisinage ou bien l'intensité instantanée de l'écoulement d'eau. Pour analyser l'interaction entre fluide et particules plus précisément, la mesure du champ de vitesse du fluide serait nécessaire. Puisque ce dernier est à trois dimensions, non-stationnaire, et fortement influencé par les particules en mouvement, ceci demanderait un gros effort expérimental supplémentaire.

D.6.2 Potentiel du dispositif expérimental

L'objectif de notre dispositif expérimental était de modéliser le transport solide par charriage d'une manière idéalisée. Nous avons utilisé des particules sphériques à taille unique. Leur mouvement, restreint à un canal étroit, était bidimensionnel. Comme désiré, la faible longueur du canal a limité

notre étude à des écoulements supercritiques. Bien entendu, notre canal particulier a imposé des plages restreintes de variation des paramètres de l'écoulement qu'on n'a pas pu choisir arbitrairement.

Malgré tout, cette approche s'est révélée féconde pour la recherche sur le transport solide. Le dispositif expérimental a permis d'ajuster les débits solide et liquide précisément pour imposer un équilibre de transport. Grâce aux techniques de traitement d'images, nous avons été en mesure de saisir le mouvement individuel d'un ensemble de particules avec une résolution élevée en temps et en espace. A cet égard, un travail considérable a dû être consacré au développement des algorithmes de traitement des données, mais aussi au raffinement du dispositif expérimental. Les données obtenues, les trajectoires de particules, ont été analysées soigneusement pour mieux comprendre les mécanismes du transport solide par charriage. Notamment, les caractéristiques du débit solide ont été étudiées de façon plus approfondie que dans toutes les autres études à notre connaissance.

Perspectives

Continûment depuis sa construction il y a cinq ans, le dispositif expérimental a évolué. Une première thèse de doctorat à été consacrée au mouvement d'une seule particule, la présente à un ensemble de particules. Ceci montre que nous poursuivons le but, d'augmenter progressivement les degrés de liberté de notre dispositif expérimental.

La largeur du canal a récemment été doublé pour permettre un mouvement des particules à trois dimensions. L'analyse des images prises sous ces conditions demandera un développement des algorithmes existants de détection et de suivi des particules. Dans une démarche suivante, il est prévu de travailler avec plusieurs tailles de particules pour étudier des processus de ségrégation. En outre, une modification du protocole expérimental est imaginable, il pourrait être intéressant d'étudier le transport des particules dans des conditions instationnaires. Ceci esquisse des études expérimentales possibles d'une future thèse de doctorat, qui devrait être élaborée au Cemagref.

Mais surtout, il faut souligner qu'à ce point de l'étude, nos résultats sont suffisamment mûrs pour nourrir et valider des modèles de transport solide. Le paragraphe suivant suggère plusieurs points de départ.

D.6.3 Apport des résultats

Les difficultés de la description du transport solide par charriage à l'aide d'une contrainte de cisaillement critique a renouvelé l'intérêt d'une meilleure compréhension des mécanismes impliqués. Plusieurs modèles récents sont basés sur des concepts alternatifs, ils ne sont pourtant pas exempt d'éléments empiriques dus à la complexité du problème. La revue bibliographique (voir §1.3) a montrée que certains de ces modèles s'intéressent à la particule. Notre étude expérimentale est notamment précieuse pour la modélisation de ce type, puisque nous avons observé le transport solide par charriage à l'échelle de la particule. Principalement, deux pistes peuvent être envisagées pour associer nos résultats à un modèle numérique :

Comparer une simulation numérique avec la simulation expérimentale. Il serait très instructif d'effectuer une simulation de transport solide avec un modèle existant en imposant des conditions les plus proches que possible des conditions de nos expériences. Bien que notre étude couvre une plage de conditions d'écoulement, plusieurs paramètres n'ont pas varié : nous avons utilisé des particules grossières à diamètre identique, le mouvement des particules est bidimensionnel, les expériences ont été réalisées à l'équilibre du transport, les pentes étaient plutôt élevées et les hauteurs d'eau faibles.

Tout modèle adaptable à ces (ou à la plupart de ces) conditions est approprié pour une comparaison avec nos données. Il faut noter qu'il est à présent improbable de trouver un modèle qui puisse être ajusté facilement à toutes les conditions citées, notamment l'effet de la surface libre de l'eau est prise en compte dans peu d'approches. Particulièrement le modèle de simulation directe de Schmeeckle et Nelson (voir §1.3.3 et [SN03]) serait adapté pour une telle comparaison. En particulier le débit solide (profils, évolution temporelle) serait une variable d'intérêt. Une telle comparaison serait fructueuse pour le modèle de transport ainsi que pour notre étude expérimentale. Pour le modèle cette confrontation pourrait avant tout permettre la validation des hypothèses faites. Pour notre étude en revanche, la comparaison pourrait suggérer comment améliorer la méthode expérimentale.

Nourrir un nouveau modèle numérique. Les résultats donnent également des idées préliminaires pour le développement d'un nouveau modèle de transport solide par charriage. Notre étude a mis en évidence l'importance : du régime de roulement, des transitions de régimes, et l'arrangement dans le lit des particules. A partir de ces résultats, il

serait peut-être possible de développer un modèle de transport solide sans être obligé de calculer la trajectoire de chaque particule. Les approches probabilistes de type “chaînes de Markov” (voir [ABFD03]) ou alors la théorie des automates cellulaires semblent prometteurs.

Il serait donc enrichissant d'orienter nos efforts vers la modélisation du transport solide par charriage, sans négliger la partie expérimentale. L'étude expérimentale de cette thèse de doctorat constitue à cet égard une base fructueuse pour la modélisation future.

References

[ABF+02] C. Ancey, F. Bigillon, P. Frey, R. Ducret, and J. Lanier. Saltating motion of a bead in a rapid water stream. *Physical Review E*, 66:036306, 2002.

[ABFD03] C. Ancey, F. Bigillon, P. Frey, and R. Ducret. Rolling motion of a bead in a rapid water stream. *Physical Review E*, 67:011303, 2003.

[ASC04] ASCE. Task committee of computational modeling of sediment transport processes. *Journal of Hydraulic Engineering*, 130:597–598, 2004.

[Aza98] E. Azanza. *Ecoulements granulaires bidimensionnels sur un plan incliné*. PhD thesis, Ecole nationale des ponts et chaussées, 1998.

[BAF+04] T. Böhm, C. Ancey, P. Frey, J.L. Reboud, and C. Ducottet. Fluctuations of the solid discharge of gravity-driven particle flows in a turbulent stream. *Physical Review E*, 69:061307, 2004.

[BAF+05] T. Böhm, C. Ancey, P. Frey, M. Jodeau, and J.L. Reboud. Experiments on gravity-driven particle flows in a turbulent stream. In *Powders and Grains*, 2005.

[Bag56] R.A. Bagnold. The flow of cohesionless grains in fluids. *Philosophical Transactions of the Royal Society of London, Series A: Mathematical an Physical Sciences*, 249:235297, 1956.

[BAJ94] G.R. Bezzola, J. Abegg, and M. Jaeggi. Saltinabrücke Brig-Glis, Rekonstruktion des Hochwassers vom 24. September 1993 in Brig-Glis. *Schweizer Ingenieur und Architekt*, 11:165–169, 1994.

[BDJ03] C. Barat, C. Ducottet, and M. Jourlin. Pattern matching using morphological probing. In *IEEE ICIP 2003*, Barcelona, Spain, 2003.

[Ber25] C.J.M. Bernard. *Cours de restauration des terrains en montagne*. ENGREF, 1925.

[Bes96] L. Besson. *Les risques naturels en montagne*. artès publialp, 1996.

[BFD+] T. Böhm, P. Frey, C. Ducottet, C. Ancey, and J.L. Reboud. Two-dimensional motion of a set of particles in a free surface flow with image processing. *Submitted to Experiments in Fluids*.

[BH93] D. Bideau and A. Hansen. *Disorder and granular media*. North Holland, 1993.

[Big01] F. Bigillon. *Etude du mouvement bidimensionnel d'une particule dans un courant d'eau sur forte pente*. PhD thesis, Université Joseph Fourier, 2001.

[BM97] J.M. Buffington and D.R. Montgomery. A systematic analysis of eight decades of incipient motion studies, with special reference to gravel-bedded rivers. *Water Resources Research*, 33:19932030, 1997.

[BP01] N.J. Balmforth and A. Provenzale. Patterns of dirt. In N.J. Balmforth and A. Provenzale, editors, *Geomorphological Fluid Mechanics*, pages 369–393. Springer Verlag, Berlin, 2001.

[Cou97] J.D. Courtney. Automatic video indexing via object motion analysis. *Pattern Recognition*, 30:607–625, 1997.

[Duc94] C. Ducottet. *Application of wavelet transforms to the processing of tomographic and holographic images of fluid flows*. PhD thesis, University of Saint Etienne France, 1994.

[Ein41] H.A. Einstein. Formulas for the transportation of bed load. *American Society of Civil Engineers Papers*, pages 351–367, 1941.

[Ein50] H.A. Einstein. The bed-load function for sediment transportation in open channel flows. *Technical Bulletin of the United States Department of Agriculture*, 1026, 1950.

[FDJ03] P. Frey, C. Ducottet, and J. Jay. Fluctuations of bed load solid discharge and grain size distribution on steep slopes with image analysis. *Experiments in Fluids*, 35:589–597, 2003.

[FLvB76] R. Fernandez-Luque and R. van Beek. Erosion and transport of bed-load sediment. *Journal of Hydraulic Research*, 14:127–144, 1976.

[FR01] P. Frey and J.L. Reboud. Experimental study of narrow free surface turbulent flows at steep slopes. In H. Ninokata, A. Wada, and N. Tanaka, editors, *Advances in Flow Modeling and Turbulence Measurements*, pages 217–224. World Scientific Publishing Co. Pte. Ltd., Singapore, 2001.

[GA93] W.H. Graf and M.S. Altinakar. *Hydraulique fluviale, Ecoulement permanent uniforme et non uniforme*. Presses polytechniques et universitaire romandes, 1993.

[Gra97] G.E. Grant. Critical flow constrains flow hydraulics in mobile-bed streams: A new hypothesis. *Water Resources Research*, 33:349–358, 1997.

[GW92] R.C. Gonzalez and R.E. Woods. *Digital Image Processing*. Addison Wesley, 2nd edition, 1992.

[Hes72] H. Hesse. *Das Glasperlenspiel*. Suhrkamp, 1972.

[HH96a] C. Hu and Y. Hui. Bed-load transport. i: mechanical characteristics. *Journal of Hydraulic Engineering*, 122:245–254, 1996.

[HH96b] C. Hu and Y. Hui. Bed-load transport. ii: stochastic characteristics. *Journal of Hydraulic Engineering*, 122:255–261, 1996.

[Hwa89] V. Hwang. Tracking feature points in time-varying images using an opportunistic selection approach. *Pattern Recognition*, 22:247–256, 1989.

[JH98] J.T. Jenkins and H.M. Hanes. Collisional sheet flows of sediment driven by a turbulent fluid. *Journal of Fluid Mechanics*, 370:29–52, 1998.

[Jod04] M. Jodeau. Etude expérimentale des mécanismes de transport solide par charriage torrentiel. Master's thesis, Université Pierre et Marie Curie, 2004.

[Jul94] P.Y. Julien. *Erosion and sedimentation*. Press Syndicate of the University of Cambridge, 1994.

[Kou93] V. Koulinski. *Etude de la formation d'un lit torrentiel*. PhD thesis, Université Joseph Fourier, 1993.

[LCYL00] H.Y. Lee, Y.H. Chen, J.Y. You, and Y.T. Lin. Investigations of continuous bed load saltating process. *Journal of Hydraulic Engineering*, 126:691–700, 2000.

[MPM48] E. Meyer-Peter and R. Müller. Formulas for bed-load transport. In *Int. Assoc. Hydraul. Res., 2nd meeting, Stockholm*, pages 39–64, 1948.

[NG94] Y. Niño and M. García. Gravel saltation, 2. modeling. *Water Resources Research*, 30:1915–1924, 1994.

[NGA94] Y. Niño, M. García, and L. Ayala. Gravel saltation, 1. experiments. *Water Resources Research*, 30:1907, 1994.

[NKH89] K. Nishino, N. Kosagi, and M. Hirata. Three-dimensional particle tracking velocimetry based on automated digital image processing. *Journal of Fluid Engineering*, (11):384–391, 1989.

[PDEF02] A.N. Papanicolaou, P. Diplas, N. Evaggelopoulos, and S. Fotopoulos. Stochastic incipient motion criterion for spheres under various bed packing conditions. *Journal of Hydraulic Engineering*, 128:369, 2002.

[PSS03] G. Parker, G. Seminara, and L. Solari. Bed load on arbitrarily sloping beds: Alternative entrainment formulation. *Water Resources Research*, 39:1183, 2003.

[Ric91] D. Rickenmann. Hyperconcentrated flow and sediment transport at steep slopes. *Journal of Hydraulic Engineering*, 117:1419, 1991.

[Ric97] D. Richard. Transport solide par charriage torrentiel. In B. Ildefonse, C. Allain, and P. Coussot, editors, *Des grands écoulements naturels à la dynamique du tas de sable ; introduction aux suspensions en géologie et en physique*, pages 105–121. Cemagref Editions, 1997.

[Shi36] A. Shields. Anwendung der Ähnlichkeitsmechanik und Turbulenzforschung auf die Geschiebebewegung. *Mitteil., PVWES, Berlin*, 26, 1936.

[SJ83] G.M. Smart and M. Jaeggi. Sediment transport on steep slopes. *Mitteilungen der Versuchsanstalt für Wasserbau, Hydrologie und Glaziologie, Zürich*, 64, 1983.

[SJ87] I.K. Sethi and R. Jain. Finding trajectories of feature points in a monocular image sequence. *IEEE Transactions on pattern analysis and machine intelligence*, 9(1):56–73, 1987.

[SKFD96] B.M. Sumer, A. Kozakiewicz, J. Fredsøe, and R. Deigaard. Velocity and concentration profiles in sheet-flow layer of movable bed. *Journal of Hydraulic Engineering*, 122:549–558, 1996.

[SN03] M.W. Schmeeckle and J.M. Nelson. Direct numerical simulation of bedload transport using a local, dynamic boundary condition. *Sedimentology*, 50:279–301, 2003.

[Soi99] P. Soille. *Morphological image analysis, principles and applications*. Springer-Verlag, 1999.

[SS90] V. Salari and I.K. Sethi. Feature point correspondence in the presence of occlusion. *IEEE Transactions Pattern Analysis Machine Intelligence*, 12:87–91, 1990.

[SSP02] G. Seminara, L. Solari, and G. Parker. Bed load on arbitrarily sloping beds: Failure of the Bagnold hypothesis. *Water Resources Research*, 38:1249, 2002.

[vR84] L.C. van Rijn. Sediment transport, part i: bed load transport. *Journal of Hydraulic Engineering*, 110:1431–1456, 1984.

[WC03] F.C. Wu and Y.J. Chou. Rolling and lifting probabilities for sediment entrainment. *Journal of Hydraulic Engineering*, 129:110, 2003.

[WG91] C.E. Willert and M. Gharib. Digital particle image velocimetry. *Experiments in Fluids*, 10:181–193, 1991.

[Woh00] E. Wohl. *Mountain rivers*. American Geophysical Union, 2000.

[WS85] P.L. Wiberg and J.D. Smith. A theoretical model for saltating grains in water. *Journal of Geophysical Research*, 90:7341–7354, 1985.

[WS89] P.L. Wiberg and J.D. Smith. Model for calculating bed load transport of sediment. *Journal of Hydraulic Engineering*, 115:101–123, 1989.